INTRACELLULAR SUBSURFACE IMAGING USING A HYBRID SHEAR-FORCE FEEDBACK/ SCANNING QUANTITATIVE PHASE MICROSCOPY TECHNIQUE.

by

Kert Edward

A dissertation submitted to the faculty of
The University of North Carolina at Charlotte
in partial fulfillment of the requirements
for the degree of Doctor of Philosophy in
Optical Science and Engineering

Charlotte

2009

Approved by:

____
Dr. Terrill W. Mayes

____
Dr. Faramarz Farahi

____
Dr. Greg Gbur

____
Dr. Robert Hocken

____
Dr. Todd Steck

ABSTRACT

KERT EDWARD. Intracellular subsurface imaging using a hybrid shear-force feedback/ scanning quantitative phase microscopy technique. (Under the direction of Dr. TERRILL W. MAYES)

Quantitative phase microscopy (QPM) allows for the imaging of translucent or transparent biological specimens without the need for exogenous contrast agents. This technique is usually applied towards the investigation of simple cells such as red blood cells which are typically enucleated and can be considered to be homogenous. However, most biological cells are nucleated and contain other interesting intracellular organelles. It has been established that the physical characteristics of certain subsurface structures such as the shape and roughness of the nucleus is well correlated with onset and progress of pathological conditions such as cancer. Although the acquired quantitative phase information of biological cells contains surface information as well as coupled subsurface information, the latter has been ignored up until now.

A novel scanning quantitative phase imaging system unencumbered by 2π ambiguities is hereby presented. This system is incorporated into a shear-force feedback scheme which allows for simultaneous phase and topography determination. It will be shown how subsequent image processing of these two data sets allows for the extraction of the subsurface component in the phase data and in vivo cell refractometry studies. Both fabricated samples and biological cells ranging from rat fibroblast cells to malaria infected human erythrocytes were investigated as part of this research. The results correlate quite well with that obtained via other microscopy techniques.

DEDICATION

This work is dedicated to my daughter; Alysa Haley Edward, wife; Shirlette Hall-Edward, mom; Fredrica Edward, and sisters Zenith and Natalie Edward. These five individuals have had the most notable and positive impact on my life over the years. Alysa, who was born on May 11th 2007, is the most recent and formidable addition to the quintet. She demanded most of our attention from day one but I especially looked forward to being home with my wife and her after long difficult days in the lab. I wish to take this moment to thank my special quintet for the love, support and encouragement I have received throughout the course of my graduate career. It really did make a difference.

ACKNOWLEDGEMENT

I am extremely grateful to Dr. Terrill W. Mayes for agreeing to act as my supervisor even after retiring from academia. I’ve learnt a great deal under his tutelage about being meticulous, diligent and persistent in my scientific endeavors. He has gone out of his way to assist me on numerous occasions regarding my research and otherwise. I respect him greatly as a talented Physicist and benevolent human being, and I am indeed privileged to have known him. Thank you.

I am indebted to John Hudack for his assistance with the coating of my NSOM probes, Dr. Mark Clemens for his assistance and advice with respect to biological imaging, Dr. Meshnick of Chapel Hill for providing me with the malaria samples, and Dr Farahi for his overall support and encouragement throughout the duration of my research. Daryl Purcell served as a very helpful sounding board whenever I needed to articulate inchoate ideas and I wish to thank him for his time and patience.

Finally, I wish to thank my wife and mom for their support. It was very difficult for my wife to deal with mundane responsibilities of running a household, while coping with a newborn without the full support of her graduate student husband. Along the way, she discovered innovative ways of getting things done and for that I will remain eternally indebted. To her and to the countless individual who helped me along the way, I extend a heartfelt thank you. The initial part of this research was funded by a grant from the National Science Foundation, award number 9988761 and subsequently by the Physics department. I wish to thank both organizations for their financial support.

TABLE OF CONTENTS

LIST OF FIGURES

LIST OF ABBREVIATIONS

PCM	Phase contrast microscope
SFF	Shear-force feedback
DIC	Differential interference contrast
NSOM	Near-field optical scanning microscope
RBCs	Red blood cells
RBC	Red blood cell
PI	Proportional integrating
SEM	Scanning electron microscope
AFM	Atomic force microscope
OPL	Optical path length
PZT	Piezoelectric transducer
RIE	Reactive ion etching
DAQ	Data acquisition
AOM	Acousto-optic modulator
PBS	Phosphate buffered saline

CHAPTER1: INTRODUCTION

1.1 Research Objective

In conventional optical microscopy, specimens often exhibit poor contrast due to the negligible effect of the field/sample interaction on the transmitted or scattered field intensity. Such objects, e.g., biological cells, require an exogenous contrast agent which often renders these cells unsuitable for in-vivo imaging. This shortcoming was circumvented in part by the development of the phase contrast microscope (PCM) in the 1930s. The PCM is, however, diffraction limited and yields qualitative results. A more complete understanding of the fundamental underlying mechanisms behind biological processes associated with physiological processes of living cells requires an imaging tool capable of quantitative non-invasive high resolution in-vivo imaging. Technical challenges notwithstanding, phase contrast microscopy appears uniquely positioned to fill this void.

Traditional phase imaging techniques such as phase contrast and differential interference contrast microscopy are qualitative in nature. Over the last decade however, there has been a proliferation of novel quantitative phase imaging techniques and instruments based on interference microscopy and phase shifting interferometry [1-8]. In all of these procedures, the phase data is strongly wrapped especially for samples with dimensions much greater than the incident wavelength. Although phase unwrapping is an option, most unwrapping algorithms require subjective participatory involvement of the user when the feature height is greater than the wavelength of the illuminating source [9], except when multiple wavelength illumination is employed [10-12].

In quantitative phase imaging, optical path length (OPL) and refractive index contributions are coupled. Two recent yet innovative approaches to decoupling these components in biological cells involved physical confinement of the specimen in a micro-fluidic cell of known dimensions [13] and an analysis of the phase data for the specimen in two solutions of slightly different refractive indices [14]. In the former instance, confinement is not always practical and in the later, the experimental setup can be complicated and tedious. The refractive index variation throughout the intracellular region of a cell is a fundamental quantity which is related to other biophysical properties (e.g. size and mass), cell permeability and hematology [15]. For example, since hemoglobin is the main constituent of red blood cells (RBCs), an abnormal hemoglobin to cell ratio such as is the case with anemia will cause a change in the refractive index. In addition, it is well known that cancerous cells have a higher refractive index compared to their normal counterparts due to higher protein content [16]. It is therefore clear that refractive index information provides valuable insight into the physiological state of a cell and the progress of pathological conditions.

In addition to thickness and refractive index information, quantitative phase data often contains coupled surface and subsurface components. The subsurface contribution however, until now has remained largely unexplored. Over the last few years, many of the recently developed quantitative phase imaging systems have been utilized in morphological studies of biological specimens. The analysis is typically simplified by assuming an average refractive index for the cell in concern. This is acceptable if the cell is homogenous such as human red blood cells but most cells contain a nucleus and other interesting organelles. As such, any acquired phase data contains surface information related to the morphology and subsurface information due to the intracellular organelles. Until now, the separation of the two components has been either very difficult or impossible. It is nevertheless known that subsurface information such as nuclear morphology and size is strongly correlated with physiological and pathological processes within the cell [18].

These unanswered questions and technical challenges related to quantitative phase imaging served as the impetus for my research. In prior investigations, I was involved in the development of a high resolution quantitative phase imaging procedure for the near-field scanning optical microscope (NSOM) [17]. This was accomplished by incorporating an environmentally stabilized Mach Zehnder interferometer into a home-built NSOM. The resultant phase although unencumbered by 2π ambiguities, was determined to be intensity dependent. As part of my most recent research, I have perfected a procedure for intensity independent quantitative phase imaging without phase ambiguities. My current research would not be possible without this milestone. The author is unaware of any other interferometric quantitative phase imaging procedure capable of unambiguous quantitative phase determination with sub-wavelength resolution using single wavelength illumination. An analysis of the phase and simultaneously obtained independent shear-force feedback topography information allows subsurface information in the phase data to be exploited for the first time. This new data has tremendous possibilities for intracellular investigations as will be shown later. By adapting the experimental setup for in vivo liquid imaging, cell refractometry analysis was also possible. Acquired experimental refractive index values for rat fibroblast in phosphate buffer solution were in good agreement with previously published results.

Throughout this research, I chose to primarily investigate structurally simple biological cells such as RBCs. As a non-biologist, this choice made the interpretation of the results fairly straightforward. Malaria infected RBCs were of particular interest because after many decades of research, this condition still leads to millions of death annually, yet the host RBCs are elementary cells without a nucleus or other organelles. Some organisms such as fishes have nucleated RBCs which proved to be ideal for examination of nuclear morphology which is strongly correlated with the progress of certain cancers [18]. The line of enquiry pursued in my research was influenced in part by these considerations.

1.2 Conventional Phase Contrast Microscopy

There are several qualitative phase microscopy techniques for imaging transparent specimens with the most notable being Zernike's phase contrast microscope [19]. The distinct advantage of this instrument over conventional bright field microscopy is that an exogenous dye is not required for contrast. Instead, these instruments convert phase shift introduced by thickness and refractive index variations across the sample into phase information. Unfortunately, there is not a linear relationship between the detected phase change and the sample thickness or refractive index and as such a quantitative analysis is typically precluded. Nevertheless, these novel microscopes have significantly impacted the field of biological imaging and a brief outline of the most notable of these instruments is presented in the next few subsections.

1.2.1 Phase Contrast Microscopy

The phase contrast microscope (PCM) was invented by the Dutch physicist Fritz Zernike in 1934 [19]. This instrument works on the principle that zeroth order planar wavefronts transmitted by the specimen are phase shifted by a phase plate and combine with spherical diffracted transmitted wavefronts. The result is a significant improvement in contrast since subtle intensity changes due to absorption, which are otherwise difficult to observe visually, are converted into intensity variations due to thickness and refractive index changes. One of the distinct advantages of the PCM over other qualitative phase contrast microscopes is that this instrument is insensitive to polarization and birefringence effects, which means that living cells can be examined in plastic tissue culture vessels. The PCM is however hampered by the appearance of light halos at the edges of the specimen. This situation is not evident in the differential interference contrast microscope.

1.2.2 Differential Interference Contrast: Normarski Interference Contrast

In the differential interference contrast microscope, the sample is illuminated by a plane-polarized wavefront [20]. A beam splitting modified Wollaston prism is used to first create orthogonal polarized, phase shifted wavefronts which impinge on the sample, and a second to combine the transmitted wavefronts. The specimen causes a relative or differential phase shift between the two wavefronts which are combined to produce a final image after passing through an analyzer. The DIC exhibits better resolution and axial specificity when compared to the PCM. The halo effect is also effectively eliminated using this procedure. However, the DIC is not conducive to imaging in plastic culture vessels due to the birefringence introduced by these containers. They are also expensive to set up and require significant increases in incident light levels compared to the PCM. This instrument adds a spurious three dimensional effect to the sample and it is often necessary to validate specimen structure with a PCM.

1.2.3 Hoffman Modulation Contrast

The Hoffman Modulation Contrast microscope (HCM) utilizes an optical amplitude spatial filter called a modulator, positioned on the back focal plane of an acromat or planchromat objective [21]. The intensity of the light transmitted through the system is modulated by the filter. The modulator consists of a small dark zone near the periphery of the back focal plane with about 1% transmission, a narrow gray zone which transmits about 15% and a third zone which constitutes most of the filter and transmits 100%. Unlike the PCM, the HCM does not measure phase changes but instead provides a three dimensional relief appearance to a sample dictated by the sample's phase gradient. The HCM makes full use of the objective's numerical aperture and allows for excellent resolution compared to the PCM. This instrument shares the axial specificity of the DIC but unlike this instrument, the HCM can be used to image cultures in plastic containers.

1.2.4 Summary of techniques

Qualitative phase imaging has had a tremendous impact on the field of biological imaging but detailed morphological cell analysis requires a quantitative phase imaging technique. In addition, setup should be relatively straightforward and in vivo image should be realized. An overview of a few of the most promising quantitative procedures is hereby presented.

1.3 Overview of Contemporary Quantitative Phase Imaging Procedures

Over the last decade, the scientific community has witnessed a sudden surge in publications and research activity related to quantitative phase imaging. A research group at the George R. Harrison Laboratory at MIT has been responsible for at least five novel techniques [22-26], two of which are highlighted in this chapter. Another group from Switzerland has successfully commercialized a quantitative phase procedure using digital holography [27], forming the company Lynceetec in the process. The appeal of quantitative phase imaging is heavily skewed towards biological imaging since it allows for detailed non-invasive morphology studies with nanometric axial resolution [28-30]. This is not possible with any other optical imaging technique and the procedure holds the potential of helping to elucidate some of the fundamental processes associated with physiological cellular activity. The technique has also been employed in numerous non-biological applications such as waveguide index profiling [31]. Quantitative phase imaging is also useful to the biologist because the phase data consists of thickness, refractive index and subsurface components which can be decoupled under certain circumstances. Changes in the refractive indices of a biological cell have been well correlated with pathological processes [32], thus the possibility of using quantitative phase imaging procedures for the detection of the early onset of diseases is a real possibility. Presented is a cross-section of a few of these techniques and their potential applications.

1.3.1 Point by point and full field illumination techniques

Quantitative phase imaging can be broadly separated into point measurement and full field illumination technique. The subsequent subsections are almost entirely devoted to full field illumination techniques since they have assumed greater prominence in recent years. However, several noteworthy point measurement techniques have been developed in only the last few years [33, 34]. Some of these procedures are based on Optical Coherence Tomography (OCT) imaging motifs such as the work of Rylander et al [35] on the differential phase contrast optical coherence microscope. In other low coherence techniques, a back-reflected signal from a single channel is analyzed to determine sample phase. In such an instance, some sort of compensation is required to deal with optical path length fluctuations. A dual channel approach such as that applied by Rylander is able to achieve very high sensitivity by cancelling common-mode phase noise. Phase sensitive OCT has the distinct advantage of allowing for three-dimensional refractive index distributions instead of integrated refractive index values which is typical with most full field techniques.

Other scanning techniques have been developed base on confocal microscopy [36] and digital holography [37]. The main drawback of these procedures is the long data acquisition time compared to full field technique, however better measurement specificity is possible.

1.3.2 Phase Shifting Interferometry

Full field techniques have the advantage of a rapid data acquisition rate which is limited primarily by the refresh rate of the capture device such as a CCD camera. In phase shifting interferometry for example, a CCD camera is used to record the interferogram formed by a test and reference signal such that the resultant intensity signal is given by;

$$I(x,y) = I_1(x,y) + I_2(x,y) + 2\sqrt{I_1(x,y)I_2(x,y)}\cos\big(\cos(\delta_s(x,y)+\alpha(t))\big) \qquad (1)$$

where $I_1(x,y)$ and $I_2(x,y)$ are the intensities of the test and reference wavefronts respectively and $\alpha(t)$ represents a controlled shifted phase introduced by a PZT actuator [38]. The objective is to solve for the sample phase $\delta_s(x,y)$ and to subsequently determine the optical path difference. In general, at least three interferograms with a PZT induced phase shift $\alpha(t)$ between them are needed to solve for the phase at each point on the investigated sample. Since these instruments operate primarily in a reflection mode, they are seldom used to investigate biological samples.

1.3.3 Fourier Phase Microscopy

Fourier phase microscopy is based on the principles of phase contrast microscopy and phase shifting interferometry [23]. The procedure involves using scattered and unscattered light from a specimen as the object and reference fields, respectively, of an interferometer. The experimental setup for this procedure is shown in figure 1.

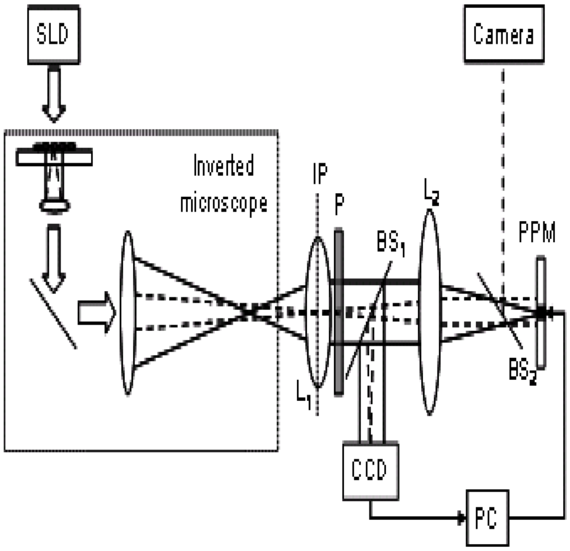

Figure 1.1: Experimental setup for Fourier phase microscope. Light from a superluminescent diode (SLD) is projected onto a programmable phase modulator (PPM) which phase shifts the light which falls onto a 2D array of individually addressed liquid crystals. The reflected signal from the PPM interfere which a reference beam and the resultant signal detected by a CCD camera (G. Popescu et al [23]).

A collimated low coherent field such as that from a superluminescent diode (SLD) is use as a source. A magnified image is formed at the image plane IP which coincides with the lens L_1. The focal length of this lens is such that it collimates the zero spatial frequency or unscattered field. The Fourier transform of the resultant image is projected by the lens L_2 onto the surface of a programmable phase modulator (PPM). The PPM consists of an optically addressed, two dimensional liquid crystal array with 768 times 768 active pixels. The polarizer P allows the polarization of the field to be adjusted in a direction parallel to the axis of the liquid crystal. This allows for precise control of the light reflected from the surface of the PPM. The beam splitter BS2 is used for alignment purposes. The PPM is used to shift the phase of the scattered field component (shown as dotted lines) in four successive increments of $\pi/2$ and the phase is calculated from the four successive interferograms. As with the other techniques which will be reviewed, phase unwrapping of the final data is required. However, this phase shifting procedure operates in a transmission mode and has found a wide range of applications in biological imaging [39, 40]

1.3.4 Hilbert Phase Microscopy

Hilbert phase microscopy makes use of a single spatial interferogram recording for quantitative phase determination [22]. This procedure is well suited to the investigation of dynamic biological processes since the acquisition time is limited only by the refresh rate of the recording device. In a typical experimental setup, light from a HeNe laser at 632.8 nm is coupled into a 1 times 2 single mode coupler with the outputs collimated. One of the outputs is used as an illumination field for an inverted microscope and the other as a reference. The two fields are combined at a beam splitter with the resulting interferogram detected using a CCD device. The reference field, which can be approximated as a plane wave, is tilted with respect to the sample field such that uniform fringes are formed at an angle of 45° with respect to the x and y axes. In the x direction, the spatial irradiance is given by;

$$I(x) = I_R + I_S(x) + 2\sqrt{I_R I_S(x)}\cos\left(qx + \delta(x)\right) \tag{2}$$

where I_R and I_S are the reference and samples irradiances, q is the spatial frequency of the fringe and δ is the spatially varying object phase of interest. Utilizing high-pass filtering and Hilbert transformation, the phase at each point in the sample can be determined.

1.3.5 Digital Holographic Phase Imaging

Digital holography was developed as a technique which combines digital recording with traditional holography [41]. The procedure is based on phase retrieval by numerically solving the Fresnel propagation equation [42]. An alternate approach involves use of angular spectrum method for diffraction calculations [43]. In a typical setup, a Mach Zehnder interferometer is employed with a coherent light source divided into an object and reference wave by a beam splitter. This allows for transmission mode imaging, although reflection mode imaging is possible with a Michelson setup [44]. In either case, the two waves interfere in an off-axis geometry and the hologram intensity at the output is given by;

$$I_H(x,y) = |R|^2 + |O|^2 + R^*O + RO^* \tag{3}$$

where R represents the reference wave intensity and O the object wave intensity. This information is digitized and recorded using a CCD camera. The digital hologram is the direct result of the two dimensional spatial sampling of $I_H(x,y)$. In classical holography, reconstruction is achieved by illuminating the hologram with a replica of the reference wave. In digital holography, reconstruction is accomplished by multiplication of the digital hologram with a digitally computed reference wave. This technique has become increasingly popular for biological imaging culminating in a commercially available instrument. However, this instrument allows diffraction limited imaging and phase unwrapping is still an area of concern.

1.3.6 Non-interferometric approaches

It is possible to obtain quantitative phase information from a specimen sample without using an interferometric approach [45, 46]. The underlying principle involves an analysis of how the propagation of light is affected by the sample. In this approach, three images are captured from a standard bright field microscope. A computational algorithm is then applied to the analysis of an in focus image, and two equidistant positive and negative out of focus images. The algorithm entails calculations of the rate of change of the light intensity between the images to determine the sample induced phase. Unlike interferometric techniques, the resulting phase data is without 2π ambiguities and does not have to be unwrapped. The positions of the equidistant out of focus images depend on the thickness of the sample under investigation. Thus it appears that the most salient issue with this procedure is the determination of the precise defocus positions which will yield optimum results. Nevertheless, this procedure appears promising as a general approach to phase microscopy with electron and x rays, as well as visible electromagnetic radiation.

1.3.7 Phase Contrast NSOM

Iravani and Crow were among the first to demonstrate phase imaging capability in a conventional near-field scanning optical microscope [47]. Using a pseudo heterodyne detection scheme with a slow feedback loop i.e. loop bandwidth much less than image bandwidth. A signal at the fundamental frequency f_m was detected which was given by;

$$ABJ_1(\theta)\cos(\delta_s) \tag{4}$$

where A and B are the light intensities of sample and reference arm of the interferometer, J_1 is the first order Bessel function of the first kind and δ_s is the sample phase. Thus the extracted phase information is intensity modulated. As such, the technique suffered from a "loss of lock" with sharp changes in the intensity of the signal transmitted through the sample.

A few years later, Saeed et al demonstrated the same concept in a reflection mode but the aforementioned problems persisted [48]. Subsequently, a procedure in a collection mode without active feedback stabilization was presented for optical phase measurement in the near field [49]. Although these techniques are ideally suited to the examination of biological samples, they have remained largely ignored as tools for biological imaging. Part of the goal of my research is to help elucidate some of the potential applications for the phase imaging enabled NSOM.

1.3.8 Summary of techniques

Quantitative phase microscopy allows for the investigation of transparent specimen with negligible light scattering characteristics. Since most of these techniques are interferometric in nature, nanometric axial resolution is routine. Point measurement imaging techniques are slow and unsuitable for dynamic studies but allow excellent sample measurement specificity. Full field measurements are typical limited only by the acquisition time of the data capture device and are ideal for dynamic studies. Without exception, interferometric quantitative phase techniques have to contend with 2π ambiguities in the final data. Possible solutions include using multiple wavelengths for imaging and phase unwrapping algorithms although both approaches have certain inherent limitations. Also, although the investigation of several techniques for decoupling sample thickness and refractive index information in quantitative phase data has been pursued, the exploitation of subsurface information has been ignored. Some of these blind spots in the body of scientific knowledge were actively addressed during my research.

1.4 Subsurface imaging: Decoupling phase components

Several traditional optical techniques are available for subsurface imaging including OCT and confocal microscopy. In recent years, several novel procedures have been developed such as the scanning near-field ultrasound microscope [50] and tomographic phase microscopy [51]. Interestingly, it was recently determined that features buried a few nanometers deep can be detected using a shear-force feedback detection scheme [52], and this will undoubtedly continue the debate concerning the nature of the shear-force interaction in the NSOM. All these disparate approaches have their pros and cons but the use of quantitative phase data for subsurface imaging has not yet been explored. Optical phase data contains coupled integrated refractive index and sample thickness information. Much research has been pursued towards decoupling these two components but not subsurface contributions. Presented is a new technique for accomplishing this task.

1.5 Multi-modal Phase Imaging

The Phase-Contrast NSOM allows for simultaneous quantitative phase, topography and intensity imaging by incorporating an environmental stabilized Mach Zehnder interferometer into a conventional home-built near-field scanning optical microscope. The stabilized interferometer exhibits a change in the optical path length of approximately 2 nm over a period of several hours. The phase information can be converted into a height value using the equation $h_p(x,y) = \theta(x,y)\lambda / 2\pi n(x,y) - 1$ where $h_p(x,y)$ is the height at position (x,y), $n(x,y)$ is the integrated refractive index at this position, $\theta(x,y)$ is the measured sample phase and λ is the illumination wavelength of 632.8 nm. For homogenous biological specimens such as human erythrocytes, the refractive index can be considered to be a constant [53] and hence the cell morphology can be determined from the aforementioned equation. Such is the idea employed in the other quantitative phase imaging techniques previously mentioned.

There are three salient features which differentiate my work from previously published results. The first is the circumvention of phase unwrapping. Subsequent subsurface information extraction would be severely limited without this accomplishment. The second is the potential for high spatial resolution due to the subwavelength NSOM probe and third being the independent shear-force feedback topography data. Since the topography data is simultaneously obtained in addition to the quantitative phase data, the refractive index $n(x,y)$ can be independently determined from the previous equation. However, the fiber probe is almost always tilted from the vertical position which results in a displacement between the sample region with which the emitted field from the tip interacts and the region which experience the tip/sample interaction. This displacement means that the phase and topography datasets need to be registered such that the phase datum h_p at the point (x,y) coincides with the topography datum h_t at some point (x',y'), such that h_p and h_t represent the same feature information in both datasets. Registration is the process of mapping the two images such that common features exactly coincide and this is performed using algorithms written in Matlab. Subsequent to this registration, subtraction and further processing of the two data sets allows for the decoupling of subsurface information in the phase data if the refractive index is known, or the determination of the integrated refractive index for homogenous samples as previously mentioned. This represents a novel solution to long standing problems in biological imaging.

1.6 In-vivo Imaging: Imaging in a liquid

Most of the biological cells investigated throughout my research were fixed dried cells. This is accepted preparation practice for cellular surface morphology studies [54] but in-vivo imaging is particularly desirable. In-vivo imaging is critical to the understanding of fundamental dynamic processes associated with cellular physiology and pathology. However, liquid imaging means that the fiber probe and perhaps the tuning fork of the shear-force feedback system need to be immersed in the culture medium. Shear-force feedback in a liquid is far from trivial [55] and several techniques have been proposed to deal with the numerous technical challenges [56-58]. A neoteric procedure for imaging in a liquid is presented. This technique was used to investigate fabricated samples image in distilled water and rat fibroblast cells image in a buffer solution. Both surface morphology and cell refractometry studies are possible using this procedure. Cell refractometry has the potential for the non invasive tracking of the progression of physiological and pathological processes and the determination of information which serves as a starting point for scattering analysis.

1.7 Fabricated Samples and Biological Imaging

Various samples with surface and subsurface features were fabricated for testing and characterization of the imaging instrument. The surface topography samples consisted primarily of photolithography fabricated micro-structures. The subsurface featured samples were fabricated by etching miscellaneous patterns into quartz glass using reactive ion etching following by photo-resist planarization. The etched structures varied in depth from 100 nm to several microns and in width from 1 micron to 7.5 microns. Samples with both surface and subsurface features were fabricated by depositing a resist pattern onto the planarization layer of the etched glass substrate. In an alternate design, red blood cells were deposited on top of the planarized subsurface features resulting in a surface/subsurface sample. These samples were used to test the subsurface imaging capability and the capacity for the extraction of subsurface information from raw phase data. These test proved the principle of operation before biological sample imaging. A selection of biological samples was investigated to illustrate some of the applications of the imaging device. These samples included human red blood cells, nucleated red blood cells, malaria infected cells, white blood cells and rat fibroblast cells. The results of these investigations and an analysis of the results are presented in the later chapters.

1.8 Summary of Results.

Throughout the course of this research, both fabricated samples and non-biological specimens were investigated. The following subsections briefly describe the types of samples investigate and comments on the rationale behind each choice.

1.81 Fabricated Samples

The fabricated samples were designed with subsurface and surface features as briefly described in section 1.7. A more detailed account of the fabrication process is found in chapter 3. The results indicate that subsurface features in the range 1 micron to 7.5 microns can be readily resolved with planarization thickness up to 12 microns. It was noted that lateral dimensions appear slightly larger than expected for samples with planarization thicknesses greater than 4 microns due to beam spreading. This effect is further highlighted in the later chapters. Using the independently acquired topography data, it was possible to suppress the sample's surface information in the phase data and successfully recover the subsurface information. The recovered height and lateral dimensions were in strong agreement with AFM and SEM results obtained prior to planarization.

1.82 Red blood cells and White blood cell

Enucleated, nucleated and malaria infected erythrocytes were imaged using the instrument. In the first instance, the size, thickness, morphology and homogenous nature of human erythrocytes were verified from the phase and extracted subsurface information. The subsurface image of the fish red blood cells clearly indicates the presence of a nucleus. The size, shape and lateral extent of this organelle was determined from the subsurface information. This has direct application to the study of the nuclear morphology of malignant cancer cells. Three different white blood cells were investigated and in each case the nucleus was clearly highlighted in the subsurface image. The overall shape and approximate sizes were readily discernable. This has direct application to the non invasive classification of these cells. Leukocytes are typically identified by the shape of their nuclei but only after staining.

1.83 In vivo imaging (Fibroblast cells)

Rat fibroblast cells were successfully imaged in a liquid. This represents a significant accomplishment since liquid evaporation is a major problem with a partially submerged tip without liquid compensation [58]. Reproducibility scans in a liquid confirmed that there were no apparent artifacts due to liquid evaporation. This allowed for cell refractometry studies of biological specimens without ad hoc modifications.

1.9 Dissertation Overview.

Chapter 1 is a general introduction to my research which included motivation and a review of the results presented herein. In Chapter 2, I will introduce the theoretical framework for unambiguous quantitative phase and subsurface information determination. The general concept of imaging in a liquid will also be highlighted in addition to the theory underlying a novel liquid replenishment system for evaporation compensation. Chapter 3 will focus on the detail of sample fabrication and the preparation procedures for the biological samples. The experimental setup and imaging procedures are elaborated upon in Chapter 4. In Chapter 5, the imaging processing procedures employed in subsurface information extraction, cell refractometry and pseudo color 3D rendering are presented. Chapters 6 and 7 include all experimental results and Chapter 8 is an outline of potential future research.

CHAPTER 2: THEORY

2.1 Introduction

The relevant theoretical framework for this research will be reviewed in this chapter. This includes the theory for phase determination and stabilization, subsurface imaging and in-vivo imaging. In the latter, the behavior of the tuning fork in air and water will be investigated. Proportional integrating circuits played a key role in this research and a general overview of these circuits will also be presented. A more detailed account of the actual circuits employed is described in my master's thesis [17].

2.2 Stabilization and Phase Determination

In my setup, light from a linearly polarized 20mW HeNe laser at 632.8nm travels along the input arm of the coupler (figure 2.1), is split into two components, and is back-reflected from both ends.

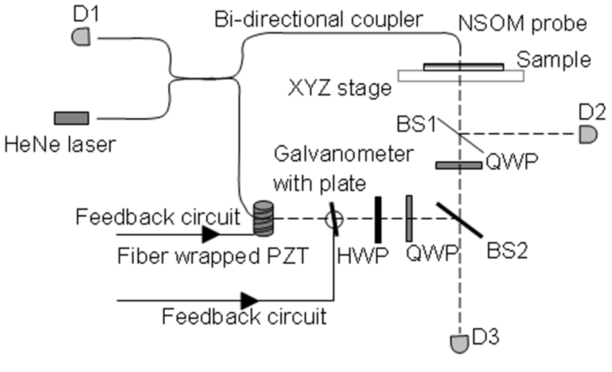

Figure 2.1: Stabilized interferometer setup: D1, D2, D3, photodiode detectors; BS1, BS2, beam splitters; QWP, quarter wave plate; HWP, half wave plate. The XYZ precision stage has a feedback controlled z-axis and computer controlled x and y axes. Dotted line shows the path of light from the output ends of coupler to detectors D2 and D3.

A section of the input arm is tightly wrapped around a piezoelectric (PZT) tube to allow for signal modulation at Ω (1 kHz). The back-reflected light from the ends of the coupler is detected with a photo-detector at D1. Thus, the light intensity impinging on this detector is given by;

$$I = I_1 + I_2 + 2\sqrt{I_1 I_2}\cos\left(\phi_o \cos(\Omega t - \delta_e)\right) \tag{5}$$

where, ϕ_o is the modulation amplitude of the signal, δ_e is the environmentally induced relative phase difference between the light traversing the two arms of the fiber coupler, and I_1 and I_2 represent the back-reflected intensities from the two ends. The cosine term in equation (5) can be expanded as an infinite Bessel function [47] series to give;

$$I = I_1 + I_2 + 2\sqrt{I_1 I_2}\begin{pmatrix} J_o(\phi_o)\cos(\delta_e) - J_1(\phi_o)\sin(\delta_e)\cos\Omega t - \\ J_2(\phi_o)\cos(\delta_e)\cos 2\Omega t - \ldots \end{pmatrix} \tag{6}$$

where $J_n(\phi_o)$ represents the nth order Bessel function.

Sample phase determination is possible only if the fiber portion of the interferometer is stabilized against environmentally induced phase noise. This was achieved using a technique similar to that pioneered by Iravani and Crow, whereby environmental stabilization was achieved by detecting the second harmonic signal of equation (6) at the output detector (D3 in figure 2.1), and maintaining the 2Ω signal at zero[47]. This procedure involves monitoring the first harmonic term, $2\sqrt{I_1 I_2}\, J_1(\phi_o) \sin\delta_e \cos\Omega t$ in equation (6), of the back-reflected signal at detector D1. Although this could just as easily been achieved using the 2Ω signal, it is preferable to use the back-reflected instead of the output signal since the former does not contain any sample phase information. The Ω signal was monitored with a "stability" lock-in amplifier which outputs a proportional signal to a PI (proportional integrating) circuit. The PI circuit sends an error signal to the fiber wrapped PZT to maintain the first harmonic term at zero. This signal induces an "error phase term" γ_{pzt} in the reference arm such that $\delta_e + \gamma_{pzt} = n\pi$. The resultant stability is equivalent to a change in the optical path length of less than 2nm over a period of several hours. The entire interferometric setup is enclosed in an isolation chamber to provide an additional measure of protection against random external thermal fluctuations.

Sample phase was determined by monitoring the output signal from detector D3. As before, it can be shown that the detected intensity signal is given by:

$$I = I_s + I_r + 2\sqrt{I_s I_r}\begin{pmatrix} J_o(\phi_o)\cos(n\pi+\delta_s) - J_1(\phi_o)\sin(n\pi+\delta_s)\cos\Omega t - \\ J_2(\phi_o)\cos(n\pi+\delta_s)\cos 2\Omega t - \ldots \end{pmatrix} \tag{7}$$

where I_s and I_r are the detected intensities of the light traversing the sample and reference arm respectively of the Mach Zehnder interferometer, and δ_s is the induced sample phase. Two additional "phase" lock-in amplifiers referenced at Ω and 2Ω are used to monitor the first and second harmonic voltages, V_Ω and $V_{2\Omega}$ respectively. At this point, there are several approaches available for sample phase determination. Three approaches were investigated as part of this research and they will be presented in the next few subsections.

2.2.1 Harmonics ratio method without phase plate

In this simple approach, the ratio of the first and second harmonic signals is used for phase determination. Before this can be accomplished, the amplitude ϕ_o of the modulation signal to the PZT is adjusted such that the first and second harmonic Bessel Functions are equalized, i.e. $J_1(\phi_o) = J_2(\phi_o)$. For an environmentally stabilized interferometer, the ratio of the first and second harmonic voltages yields:

$$\frac{V_{\Omega}}{V_{2\Omega}} = \left(\frac{\sin(n\pi + \delta_s)}{\cos(n\pi + \delta_s)} \right) = \tan(\delta_s) \tag{8}$$

It should be noted that δ_s obtained using the first harmonic term is intensity independent. The system was operated in a transmission mode, although it is possible to implement this idea in a reflection regime [48]. The harmonic ratio of equation (8) was calculated in real-time using LabView and the resultant phase data stored as a 2-dimensional array. The phase is bounded within the limits $0 \leq \delta_s \leq 2\pi$ and as such, post imaging unwrapping is required for thick samples outside this limit. Using a 632.8 nm light source, it is theoretically possible to image samples up to approximately 1.3 microns thick, given an average sample refractive index of 1.5. This assumes that the scan is initiated at the lowest point and that the initial phase is 0 degrees. Since these two conditions are almost never achieved in practice, the maximum sample thickness which can be scanned without the need for unwrapping is typically half the theoretical maximum.

2.2.2 First harmonic controlled plate

A novel approach for phase imaging was explored which circumvented the need for post imaging phase unwrapping. A related idea was employed by R. Hocken in his investigation of the refractive index of the gas Xenon [59]. In this approach, the first harmonic signal, $2\sqrt{I_1 I_2}\, J_1(\phi_o) \sin(n\pi + \delta_s) \cos\Omega t$ was kept at zero by actively adjusting the position of an angular displacement plate in the reference arm. This plate was attached to a feedback control precision galvanometer (General Scanning Inc, model 6124). During operation, the plate introduces a phase γ_{plate} such that the term $\delta_s + \gamma_{plate}$ was kept at an integral multiple of π, where δ_s is the sample phase. Thus the phase change introduced by the plate is equal to the phase change introduced by the sample.

The change in phase introduced by the plate is directly related to its angular displacement, which is in turn related to the voltage applied to the galvanometer. To determine the relationship between induced phase and applied voltage, the system was calibrated with the calibration plot represented in figure 2.2. The equation of the best fit line was given by $-41.33x^3 + 362.29x^2 -27.30x + 96.74$.

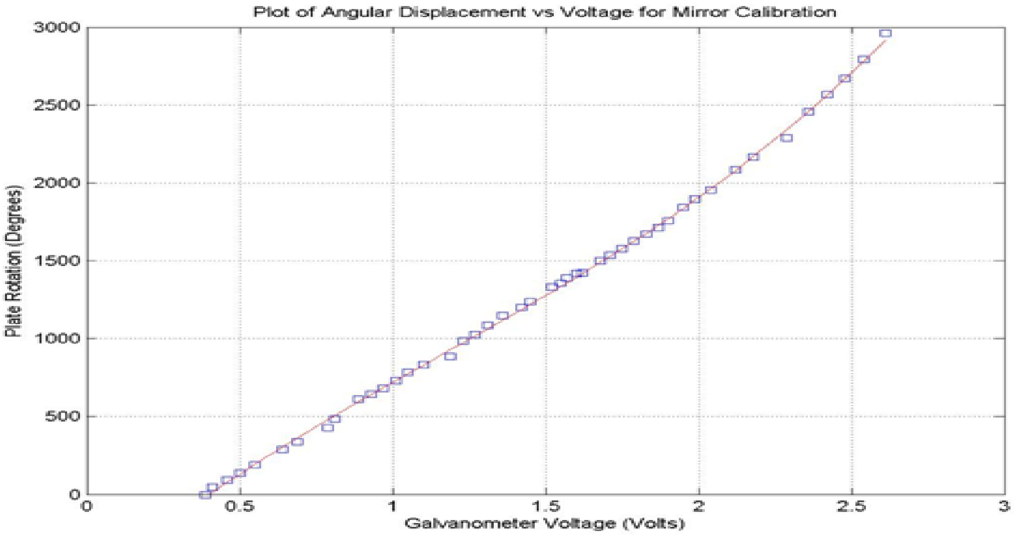

Figure 2.2: Calibration curve for galvanometer and angular displacement plate setup without a sample. As the applied voltage to the galvanometer was varied, the induced phase change was measured using the harmonic ratio method described in section 2.2.1. This curve was used to determine the induced sample phase by keeping the first harmonic voltage at zero.

This curve was obtained by applying a known voltage to the galvanometer, and measuring the induced phase of the displacement plate without a sample in place. The plate induced phase was determined using the harmonic ratio method described in section 2.2.1 and equation 8. Although the sample phase change can be determined by utilizing the first harmonic signal to control the displacement plate, the intensity term $2\sqrt{I_1 I_2}$ in the expression renders the resultant phase intensity dependent. The extraneous intensity modulation causes the system to become unstable which can result in a “loss of lock” of the lock-in amplifiers. This situation is further exacerbated when imaging thick samples with low throughout. To resolve this problem, the ratio of the harmonic terms was used to control the angular displacement plate.

2.2.3 Harmonic ratio controlled plate

In this approach, the ratio signal of equation (8) was used to actively adjust the position of a galvanometer controlled angular displacement plate in the reference arm of the interferometer. Thus the setup was identical to that described in section 2.2.1 except that the ratio signal was calculated using the ratio function of the 2nd harmonic lock-in instead of the LabView application. This is a faster process than using a Windows based PC and data acquisition card to access the galvanometer. Alternatively, a ratio circuit can be built using log and antilog operational amplifiers as shown in figure 2.3.

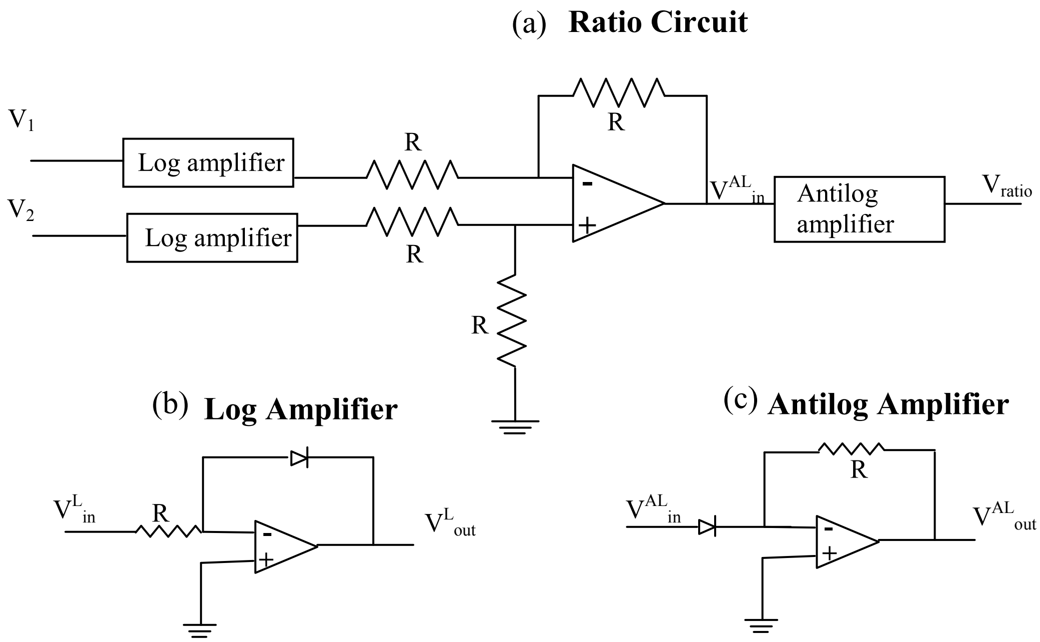
(a) **Ratio Circuit**

(b) **Log Amplifier**

(c) **Antilog Amplifier**

Figure 2.3: Figure (a) is a schematic of a simple ratio circuit using logarithmic and antilogarithmic components. Figures (b) and (c) are schematics of the individual component amplifiers which constitute (a). This circuit works well if the denominator voltage is sufficient large (i.e. several millivolts).

The output of a logarithmic amplifier V^{L}_{out} is given by;

$$V_{out}^{L} = k \ln \frac{V_{in}}{RI_s} \tag{9}$$

where k is a constant and I_s is the saturation current. It can be shown that the input to the antilog circuit V^{AL}_{in} in figure 2.3(a) is related to the original inputs as shown below.

$$V_{in}^{AL} \propto k \ln \frac{V_1}{V_2} \tag{10}$$

The output of the antilog circuit is an exponential function and as such the output signal is proportional to the ratio V_1/V_2. These circuits proved to be very unstable for values of V_2 much less than 1 millivolt and very sensitive to environmental temperature fluctuations. I also experimented with a few commercially available ratio amplifiers, such as the AD734 four-quadrant analog divider with limited success. Using the ratio function on the lock-in appears to be the most efficacious approach to dividing the 1st and 2nd harmonic signals. The phase determination procedure is identical to that described in section 2.2.2, except that the PI circuit outputs a ratio signal instead of a signal proportional to the first harmonic voltage. With the feedback circuit engaged, the ratio signal is maintained at zero. Thus the first harmonic signal is kept at zero and the second harmonic at a maximum. As described before, the sample phase is determined from the calibration curve shown in figure 2.2.

Detector D2 in figure 2.1 detects a portion of the light transmitted by the sample and reflected at the beam splitter BS1, resulting in an intensity signal. A topography image is obtained from the shear-force feedback error signal used for sample-probe distance regulation [60]. The images from the three imaging modalities are built up pixel by pixel as the sample is raster scanned. The phase data can be converted to topography information using the relationship,

$$t = \frac{\Delta\delta_s \lambda}{2\pi(n_s - 1)} \tag{11}$$

where t is the sample thickness or height, $\Delta\delta_s$ is the measured sample phase, λ is the wavelength of the illumination source and n_s is the average refractive index of the sample.

2.4 Subsurface imaging

During a scan, intensity, phase and surface topography data points are simultaneously obtained at predetermined time intervals. The latter image is used to extract the subsurface details in the phase data. Intensity line scans are useful in locating subsurface features for the purpose of probe positioning prior to scanning.

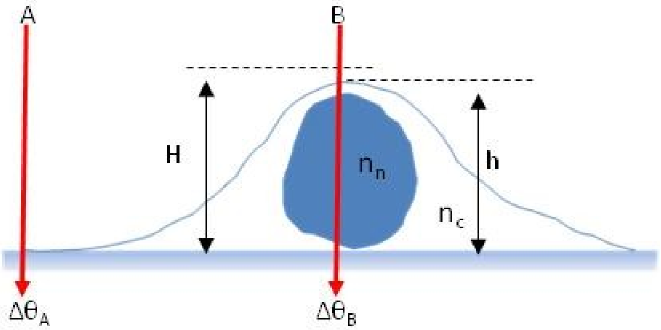

Figure 2.4: The schematic shown represents a simple biological cell with a single prominent subsurface feature. The nucleus has a height h and protrudes through the cell membrane as is typical. The cell has an external height H.

Although a near-field setup is employed, the optical images are not near-field images due to the thickness of the samples imaged which range from 1 to 3 microns. Consider a simple biological cell with a nucleus of thickness h and refractive index n_n shown in figure 2.4. The height of the cell is given by H, the refractive index of the cytoplasm is given by n_c and the induced phase values at points A and B are given by $\Delta\theta_A$ and $\Delta\theta_B$ respectively. The phase change $\Delta\theta_{BA}$ between points B and A is given by $\Delta\theta_{BA} = \Delta\theta_B - \Delta\theta_A$. It can be shown that the subsurface feature height is given by,

$$h = \frac{\lambda}{2\pi(n_n - n_c)}\left(\Delta\theta_{BA} - \frac{2\pi}{\lambda}H\left(n_c - 1\right)\right) \tag{12}$$

where λ is the illumination wavelength of 632.8 nm. The cell thickness H is determined directly from the shear-force topography feedback data. This data contains information about the surface morphology and can be expressed as a phase change using the expression,

$$\Delta\theta^t{}_{BA} = \frac{2\pi}{\lambda}H\left(n_c - 1\right) \tag{13}$$

Thus we can represent the subsurface feature height at any point (x,y) as,

$$h(x,y) = \frac{\lambda}{2\pi\Delta n(x,y)}\left(\Delta\theta_{BA}(x,y) - \Delta\theta^t{}_{BA}(x,y)\right) \tag{14}$$

where $\Delta n(x,y)$ is given by $n_n(x,y) - n_c(x,y)$. Thus the subsurface height at any point is proportional to the difference between the acquired phase and the phase equivalence of the height at that point.

During the experimental setup, it is extremely difficult to position the probe exactly orthogonal to the plane of the substrate beneath. As such, there is a displacement between the shear-force and phase data because slightly different regions are accessed as shown in figure 2.5. The emitted field from the tip interacts with a sample region which depends on the tilt of the probe but the shear-force interaction occurs between the tip and the region directly below. Thus when the probe is above region A, T(x,y) and the phase $P(x', y')$ at B are recorded, instead of P(x, y) at A. The displacement in the acquired datasets ranges from 200- 500nm in both directions. This is corrected using image registration algorithms.

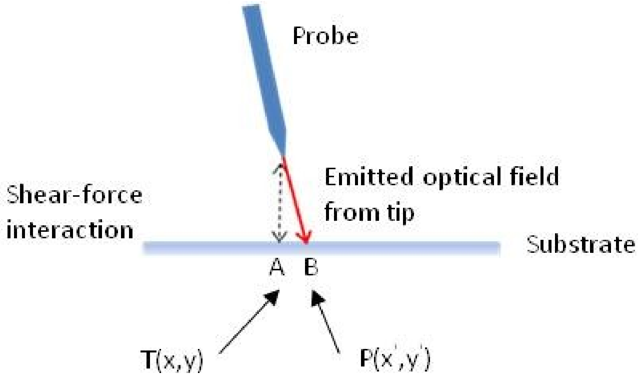

Figure 2.5: The diagram depicts a typical orientation of the tip relative to the sample. The tilt of the probe is exaggerated to emphasize the displacement between the acquired phase and topography images.

Thus for each point in the scan, the subsurface feature height is given by;

$$h(x,y) = \frac{\lambda}{2\pi \Delta n(x,y)} \left(P(x,y) - T_{\theta}(x,y) \right) \tag{15}$$

where P(x,y) is the registered phase value and $T_\theta(x,y)$ is the corresponding topography value converted to a phase value using Eq.13 at point (x,y). The data subtraction procedure is analogous to the case of digital subtraction angiography in which a mask (topography data) is subtracted from a reference dataset (phase) [61]. Unless registration is perfect, a residue difference error results after image subtraction. This error was minimized by suppressing sharp peaks in the final data.

2.5 Shear force feedback imaging

The basic idea associated with the near-field scanning optical microscope (NSOM) is to position a sub-wavelength aperture probe in such close proximity to the investigated sample that the emitted field interacts with a highly localized sample region. Under this condition, the field interacts with a region approximately equal to the size of the illuminating aperture (40-100nm). Hence it is possible to achieve very high sub-wavelength optical resolution. Most NSOM probes are typically fabricated by etching [75] although other approaches are available [17]. Since the intensity image is generated in a point by point manner as the sample is raster scanned, it is necessary to maintain a constant tip/sample separation to avoid catastrophic collisions. This is typically accomplished using a shear-force feedback system in which a dithered tuning fork attached to a fiber probe acts as a mechanical "pick-up". When the probe/sample separation is within the near field, the vibrations of the dithered probe are linearly damped within separation distance due to shear-forces. By monitoring the phase difference between the signal sent to a mini-PZT which dithers the tuning fork and the separation distance dependent signal generated by the tuning fork, it is possible to maintain a constant tip/sample separation during a scan. An error signal generated by a PI circuit is used to adjust the z-axis of a precision three axis controlled X,Y,Z stage on which the sample sits. It is possible to generate a simultaneous topography image using this error signal. In the next section, I will briefly review some of the relevant theory associated with operating a shear-force feedback system in air and in a liquid environment.

2.51 Tuning fork/ probe assembly in air and water

The main component of the mechanical "pick-up" system is a quartz tuning fork. These devices have a resonant frequency which can range from 32 kHz-100 kHz. The tuning fork consists of a piezoelectric substrate which allows for the interchangeable conversion of electrical signals into mechanical motion [62]. Throughout this investigation, tuning forks with a resonant frequency of 32.768 kHz were employed. The dithering of the tip occurs in a plane parallel to the surface of the sample.

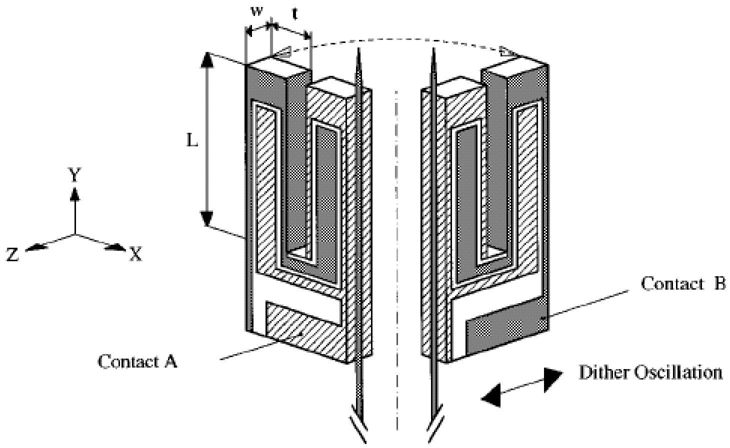

Figure 2.6: The diagram depicts the front and back of a crystal tuning fork with a 125 μm tapered fiber probe glued to one of the prongs. X, Y and Z are the quartz crystal axis. The shaded and dark regions serve as contacts pads which allow for coupling between the two prongs and also act as pickups for the piezoelectric signal [73].

In an experimental setup, approximately 1 mm of fiber hangs over the prong. To determine the dynamics of the prong, the parameters required are the cantilever length L, rectangular cross-section wt and its Young's modulus E and density ρ [73]. Using this model, the time dependence of the position of the tip is described by a harmonic oscillator equation driven at frequency ω as shown in the equation 16.

$$m_e \frac{\partial^2 x}{\partial t^2} + F_D + kx = Fe^{i\omega t} \tag{16}$$

where m_e is an effective mass corresponding to about ¼ of the mass of one of the prongs, F is the amplitude of the driving force, k is the static compliance of one of the prongs and $F_D = m_e\gamma\partial x/\partial t$ is a viscous force which is the sum of all drag forces acting on the cantilever. For small drag (i.e. $\gamma << \omega$), the solution of equation 16 is given by,

$$x = \frac{F/m_e}{\left(\omega_0^2 - \omega^2 + i\gamma\omega\right)} e^{i\omega t} \qquad (17)$$

where F_D is now given by $F_D = i m_e \gamma \omega x$ and both the viscous force and x are characterized by a resonant frequency $\omega_o = \sqrt{(k/m_e)}$. The amplitude of x depicts a Lorenzian dependence which can be characterized by a Q or quality factor given by $Q = f_o/\Delta f$ where Δf is the full width at half the maximum amplitude at resonance. A tuning fork without a probe attached can have a Q factor as large as 7000 in air. With a probe attached, this value falls to between 400-1000. If a portion of the protruding fiber from the fork is immersed in a liquid of a given viscosity, at a constant drive force, as the immersion depth increases, so does the drag force. Therefore, we would expect the Q factor and the amplitude of displacement to decrease. Thus my strategy for imaging in a liquid was to minimize the drag and maximize Q by keeping the immersion depth to a minimum. The setup employed to accomplish this is briefly reviewed in the next section. A much more detailed account of the behavior of quartz tuning forks in air and in a liquid as applied to shear-force feedback can be found in the following references [63-68].

2.52 Evaporation compensation.

The Q factor of a tuning fork is a measure of its sensitivity. This quantity is paramount when imaging soft samples in a liquid environment using a shear-force feedback setup. If the immersion depth of the probe is too great, the Q factor is significantly decreased to the point where it impossible to scan the sample of interest without crashing. If the immersion depth is too shallow, then artifacts due to liquid evaporation and the resulting change in the immersion depth can occur. To achieve high Q liquid imaging, an evaporation compensation system was developed based on a setup similar to that of Gheber et al [73]. In this approach however, the sample was completely immersed in a liquid chamber with a hole at the top for probe access, and as such large damping forces resulted in a 40% reduction in the Q factors. A similar idea was employed by a research group at Berkley except that an electronic pump was used to control the liquid level [87]. My setup is simpler and yields comparable results in terms of a minimal % drop in the Q factor for liquid imaging.

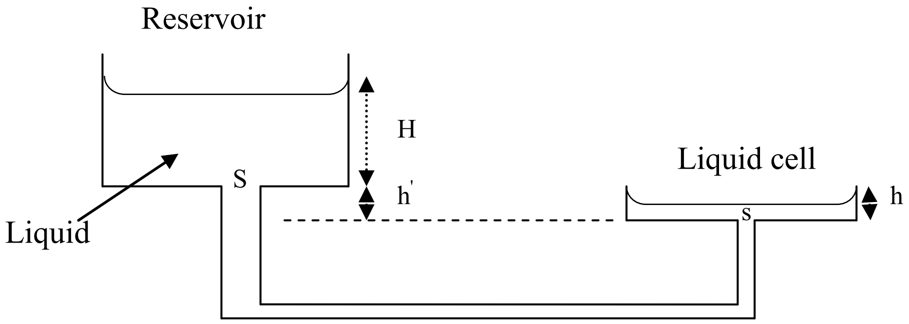

Figure 2.7: Schematic of liquid evaporation compensation system. The system operates by the siphoning action of liquid movement between a reservoir and liquid cell of which the liquid heights are given by H and h respectively. The vertical position of the reservoir $h^{'}$ can be adjusted so that the liquid flow from the reservoir to the cell is equal to the evaporation rate. The effective cross-sectional area of the tube connecting the cell and reservoir is larger for the reservoir S, than for the liquid cell.

A schematic of my experimental setup is shown in figure 2.7. The sample sits in the liquid cell and an o-ring is used to create a negative meniscus above the sample, which helps to maintain a very thin film. The objective is to adjust the height $h^{'}$ such that the liquid level in the cell remains constant even as evaporation occurs. This is easier to achieve when the tube leaving the reservoir has a larger effective cross-sectional area than that entering the cell. If the liquid level in the cell is constant, then the force through opening S is equal to the force through opening s. Once the volume of liquid V in the reservoir, is sufficient large, then $\partial V/\partial t \sim 0$ over the period of a few hours. A lid with tiny holes was placed on top the reservoir to minimize evaporation. Since the volume of liquid v in the cell is small compared to the evaporation volume, the liquid loss results in a force imbalance due to the reduced pressure exerted by the remaining liquid. This is compensated for by liquid slowly moving from the reservoir to the liquid cell.

2.6 Proportional integrating circuits

Three proportional integrating circuits were used as part of this investigation. Environmental stabilization, shear-force feedback and control of the galvanometer mounted angular displacement plate were all achieved using PI circuits. Schematics of the circuits and an overview of the operation of each circuit can be found elsewhere [17]. In this section, I will provide a general introduction to PI circuits and their applications.

Proportional-integral/integrating control is a ubiquitous control approach used in industry which has found universal acceptance in industrial control. PI circuits are particularly popular because their robust performance over a wide range of operating conditions and functional simplicity allow for straight forward operation. As the name suggest, a PI controller consist of two main components; a proportional component and a integrating component. A control system consists of a PI circuit/controller, a sensor and an output actuator. In a control system, the system parameter which needs to be controlled (process variable) is monitored by a sensor. The difference between the desired value for the process variable (set point) and the process variable is kept at near zero via feedback control of the actuator, which in turn influences the state of the process variable. Figure 2.8 represent the two main components of a PI circuit. In my specific situation, the input signal V_{in} for both circuits components comes from the lock-in amplifier. The set point is defined using the lock-in and the output is proportional to the difference between this value and the process variable e.g. z position of the precision stage.

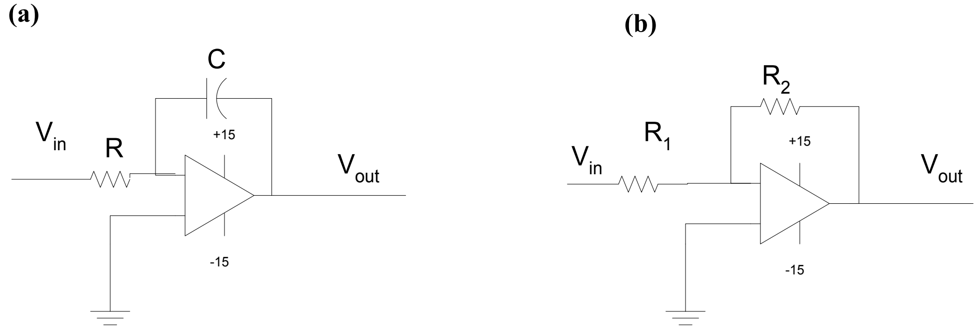

Figure 2.8: Schematics of an opamp integrator and inverting amplifier are shown in (a) and (b). These two circuits constitute the basic components of a PI circuit. The capacitance and resistance values must be judiciously chosen to allow for stable operation.

In that case, the PI output is given by,

$$V_{z-axis} = \left(k_1 \left(\frac{R_2}{R_1} V_{lock-in} + \frac{1}{RC} \int V_{lock-in} dt \right) \right) \tag{18}$$

where k_1 is a proportional gain factor. If $V_{lock\text{-}in}$ (the difference between the set point and process variable) is zero, the error signal is a constant. If the set point and process variable are not equal, an output signal from the circuit given by equation 17 attempts to main $V_{lock\text{-}in}$ at zero.

This general idea is the principle of operation associated with all three proportional integrating circuits employed as part of this research. In each case, time constants were chosen so as to allow for stable long-term operation. In the case of the precision galvanometer, this meant that the rate of angular displacement had to be significantly reduced. This will be examined in chapter 8 together with new ideas for improving the temporal resolution of the system. In the next chapter, the details of the sample fabrication process will be reviewed.

CHAPTER 3: SAMPLE PREPARATION, FABRICATION AND CHARACTERIZATION

3.1 Overview of Investigated Samples

Selected fabricated structures and biological samples were investigated as test objects to analyze the quantitative phase, shear-force feedback topography and intensity imaging performance of the phase contrast NSOM. The non-biological samples were fabricated using the clean room facilities of the Optics department at UNCC. These samples were all subsequently characterized using an atomic force microscope and a scanning electron microscope (SEM). Specific regions of the samples were also characterized using a profilometer. The fabricated samples consisted of samples with (1) surface features only, (2) samples with subsurface features only and (3) samples with both surface and subsurface features. In this chapter, the fabrication process for each of these samples will be reviewed in detail.

Several biological samples were imaged throughout the investigation. These samples were selected based on their structural simplicity and physiological characteristics such as the presence of absence of a nucleus. For example, human red blood cells were selected because they are simple cells without any intracellular components. These cells served as a control for the subsurface investigation of the biological samples. Fish red blood cells and human white blood cells however, are nucleated with large easily identifiable nuclei which proved ideal for subsurface analysis. Plasmodium Falciparum (malaria) infected RBCs were chosen to illustrate a powerful potential application of the instrument. The malaria samples were obtained from the School of Public Health and the Department of Cell and Developmental Biological of the University of North Carolina Chapel Hill. My in vivo studies involved working with rat fibroblast cells obtained from UNCC's Biology department. All preparation techniques will be reviewed in further detail.

3.2 Fabricates Samples

Three different types of fabricated structures were investigated throughout my research. The simplest of these were the samples with surface features only. These samples consisted of phototresist microstructures. To detect subsurface features in the absence of surface features, a sample with RIE etched features was planarized. Planarization entailed coating several layers of a resist material over etched structures, such that top surface was nearly planar. The third type of samples with surface and subsurface features were designed to represent primitive biological cells. They were essentially "subsurface-feature" samples with surface features deposited on the planar surfaces. The fabrication details of all three types of samples will be reviewed in this section.

3.2.1 Surface Features: Photoresist Samples

The samples with surface features were fabricated via a photolithographic process. First a quartz glass substrate was cleaned by immersing in piranha solution (sulfuric acid/hydrogen peroxide solution mixture) to remove any organic impurities. The substrate was then spin coated with a thin layer of photoresist followed by a low temperature soft baking. A mask with a pattern of 2 micron circles on 4 micron centers was used to selectively expose the resist layer with a UV light source via contact printing. In contact printing, the mask and resist coated substrate are in direct contact during the exposure process which allows for high resolution pattern transfer. If the photoresist is positive, the exposed region undergoes a chemical change and becomes soluble in a developer solution. In the case of negative resist, the unexposed region becomes soluble in developer solution.

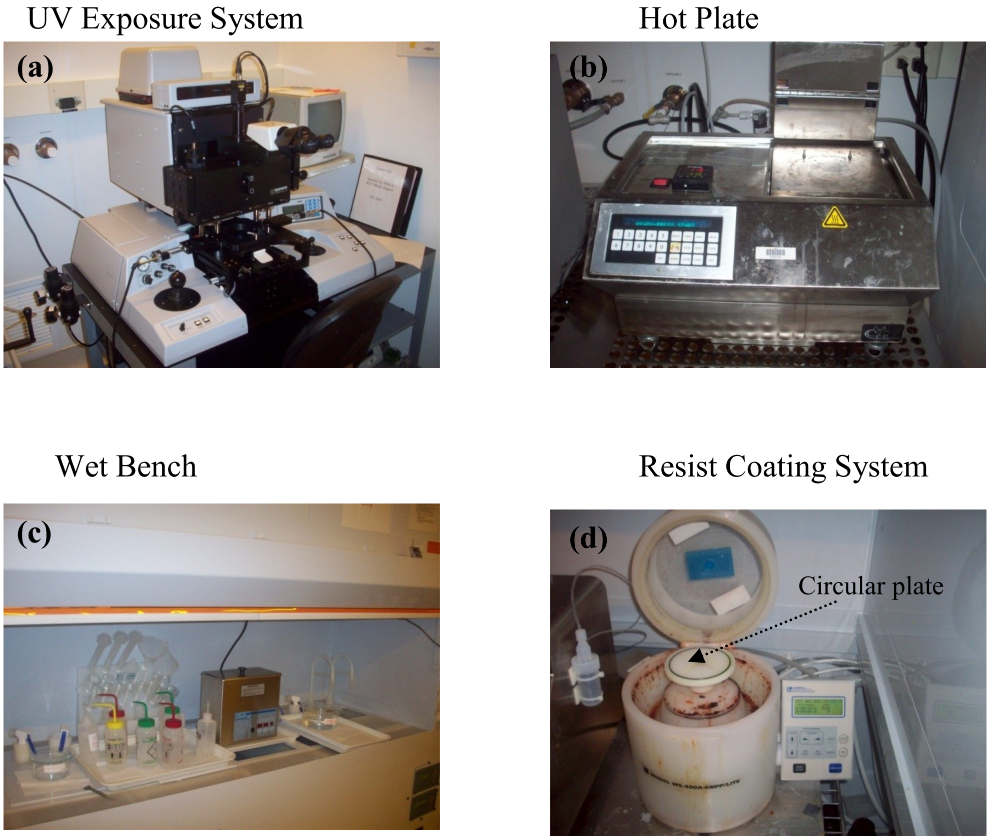

Figure 3.1: Image (a) is a photograph of the contact alignment photolithography system. The UV source and alignment components sit on top with a viewing monitor on the right. Images (b) and (c) are photographs of the hot plate used for baking and wet bench area used for development respectively. Image (d) depicts the spin coating system. The substrate is held in place on the circular plate in the image via vacuum adhesion.

In either case, the sample is "developed" by rinsing in a developer solution which removes the soluble photoresist and leaves behind a pattern of insoluble resist. After this step, the sample typically undergoes a post exposure bake to allow for complete curing. Any defective transferred patterns can be removed from the substrate by etching in piranha solution and the process repeated.

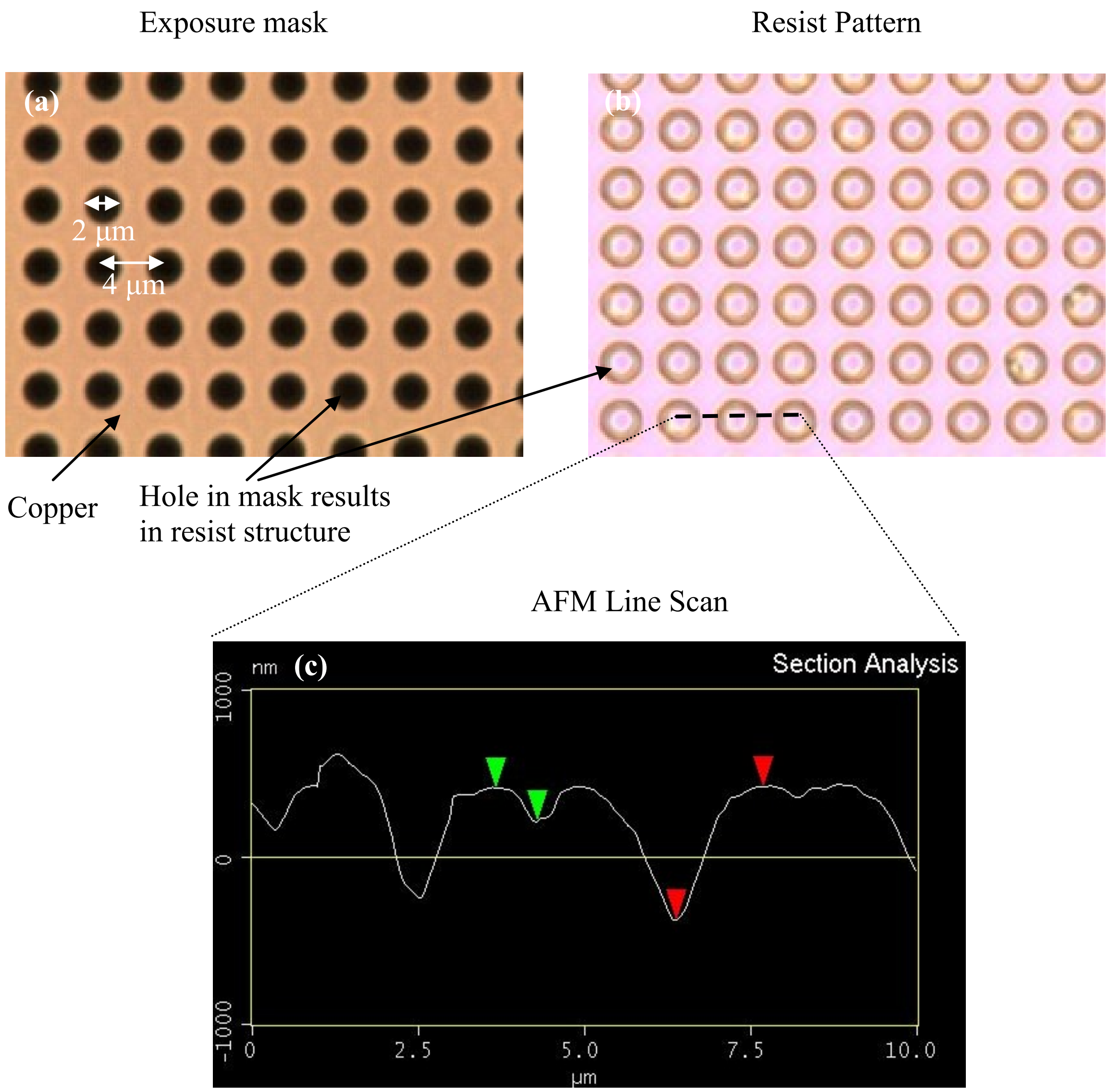

Figure 3.2: Image (a) is an optical image of the mask used for the sample fabrication process. The mask consists of 2 micron holes in a copper plate. The circular holes are 2 microns in diameter on 4 micron centers. Image (b) is an optical image of the transferred resist pattern. An AFM line scan of the region identified by the dark line is shown in (c).

The mask used for sample fabrication consisted of 2 micron circles on 4 micron centers as shown in figure 3.2(a). The photolithographic process previously described allows for the effective transfer of this pattern to a layer of photoresist. An image of the resist pattern as seen under an optical microscope is shown in 3.2 (b). Figure 3.2(c) is an AFM line scan of the over the region indicated by the black line in 3.2(b).

3.2.2 Subsurface Features: Planarized etched quartz glass

Fabrication of the samples with subsurface features involved dry etching micro-structures onto a quartz glass substrate via reactive ion etching (RIE) [69], followed by planarization of the features with photoresist.

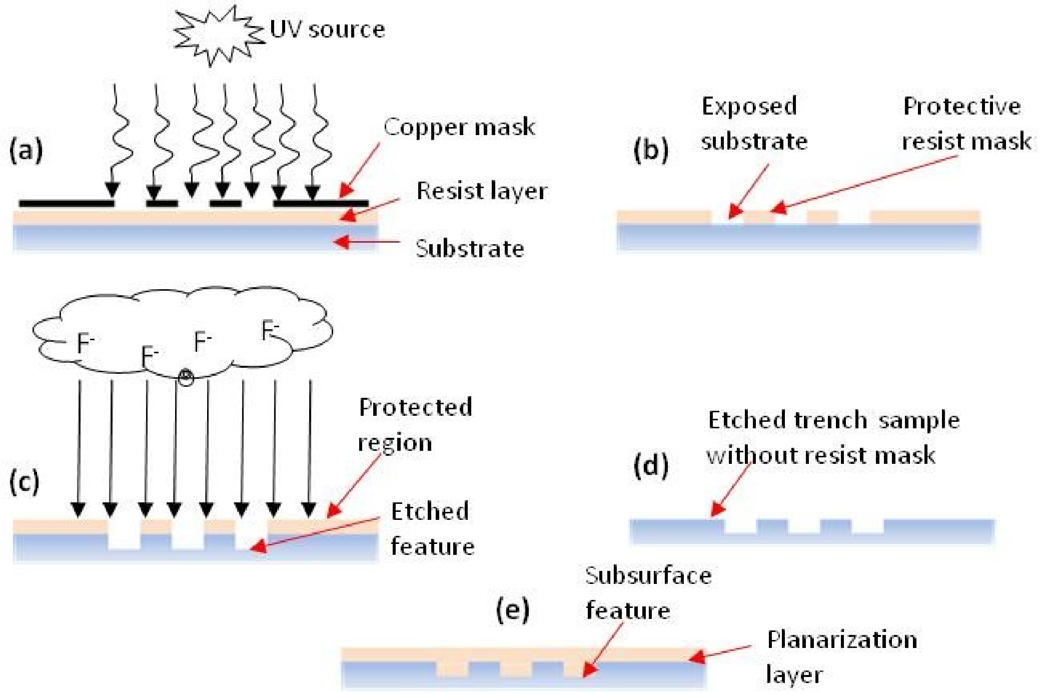

Figure 3.3: The stages in the fabrication of the samples with subsurface features are depicted in images a-e. In (a), the sample is exposed to UV light and subsequently developed to yield (b). The sample is then etched using RIE (c), followed by a striping of the resist mask (d). The result is a glass substrate with an etched pattern determined by the resist mask. This sample is then planarized with resist to produce a sample with subsurface features (e).

Prior to etching, a photoresist mask was created as describe in section 3.2.1. This mask is simply the transferred pattern of a copper mask onto a resist layer as shown in figures 3.3 (a) and (b). The pattern protects all resist covered regions of the substrate from the etching effect of a gas plasma during RIE. All unprotected regions are anisotrophically etched as shown in figure 3.3(c). The resulting micro-structures in (d) are subsequently planarized as described earlier.

Reactive ion etching is a dry etching procedure which results in anisotropic etching (highly directional) compared to the isotropic nature of wet etching. This is very important for high fidelity pattern transfer such as in micro-fabrication. In this process, plasma is generated from a gas pumped into an evacuated chamber using a strong radio frequency electromagnetic field. An electric field is used to accelerate the ions towards the substrate where they bombard and chemical react with the atoms at the surface. The etching is typical produced by the action of fluoride ions generated from gases such as sulfur hexafluoride SF6 and carbon tetrafluoride (CF_4). The resist mask selectively protects covered regions on the substrate while the exposed regions are etched to produce the desired pattern.

The copper mask used to create the resist mask consisted of an array of groups of rectangular structures. Each group contained up to seven of those structures with each structure separated from adjacent members by a fixed distance. Thus there exists a trench of fixed width between each rectangular structure. In this investigation, I was interested in the trenches and not the rectangular features. The resulting resist pattern created by the mask is shown in figure 3.4(a). A group of rectangular structures is highlighted in this figure although several other groups may be observed. The feature separation distance is fixed within a group, but it varies from one group to another, ranging from 2-10 microns. An SEM image of the highlighted group is shown in figure 3.4(b). The dark line in (b) represents a region of the sample which was scanned with an AFM. The line scan is shown in 3.4(c) and indicates that the separation distance for features in that group is approximately 5 microns.

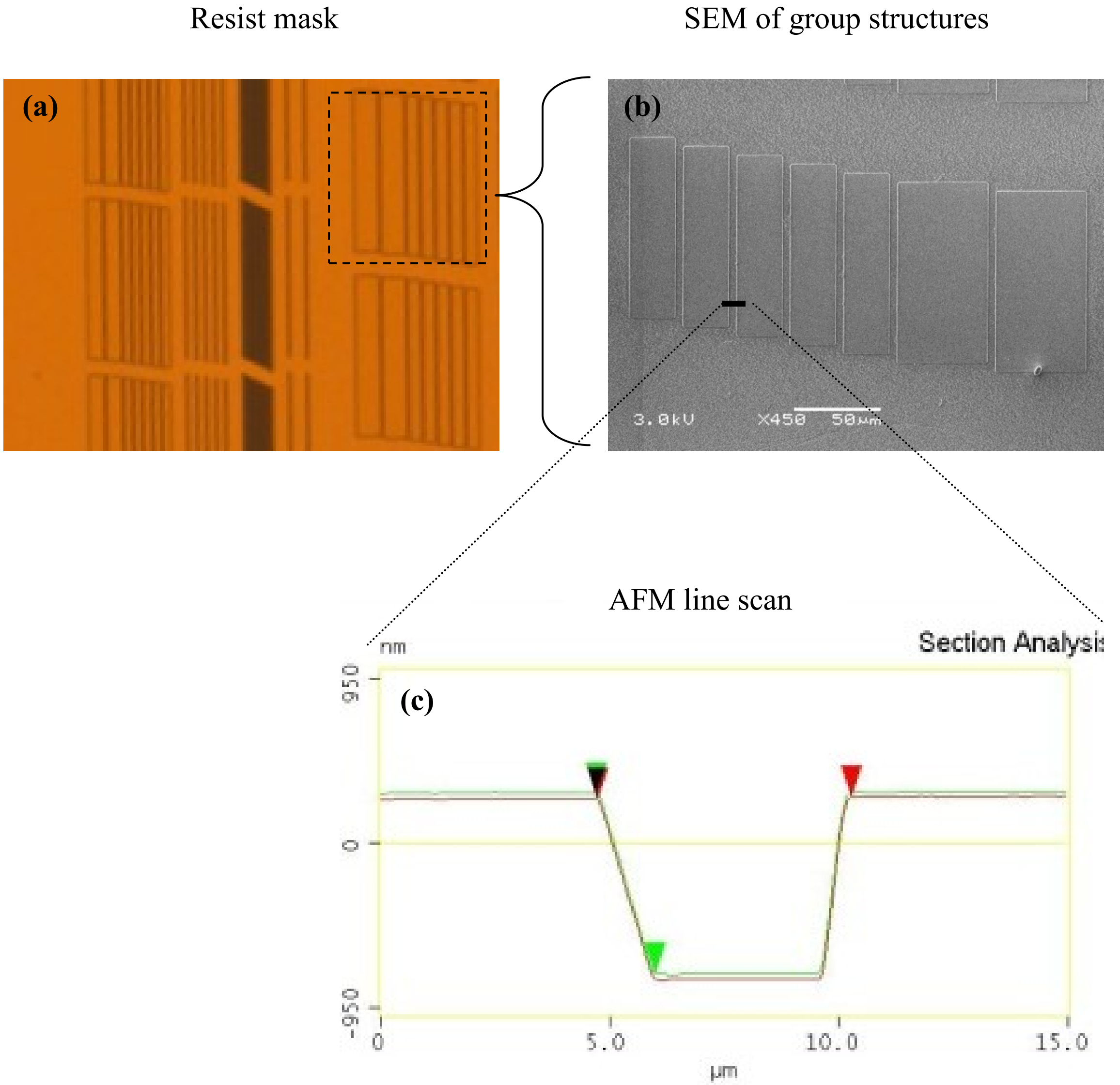

Figure 3.4: Image (a) is an optical image of the mask used for etching. It consisted of several groups of rectangular structures with one of the groups highlighted by a black square. A SEM image of the highlighted region in (a) is shown in (b). The dark line in (b) represents a region of the sample that was scanned using an AFM. A line scan of the scanned region is shown in (c). The etched trench was subsequently planarized in the final step in the fabrication process.

The scan indicates that although the side walls of the trench are sloped, they are nevertheless quite straight. It was possible to fabricated trenches of various depths by controlling the etch time for the etching process. The etch recipe used during sample fabrication allowed for etching at a rate of 62 Angstroms per second using quartz glass, so depth control was relatively straight forward. Features ranging in depth from 200nm to 1 μm were fabricated.

The final and most difficult step of the fabrication process is planarization. This was performed using SU8 photoresist which is essential transparent at optical frequencies. Thus it was possible to readily locate the underlying features by inspection with a light microscope. Planarization was achieved by overlaying several layers onto the etched substrate. Each layer was heated to ensure reflow and cross-polymerization of the resist. After each layer, the degree of planarization was determined using a profilometer. It was possible to planarize a 1 micron tall feature to within 100nm using this procedure.

3.2.3 Surface/ Subsurface features

Two different types of samples with surface/ subsurface features were fabricated. The first type of sample consisted the resist pattern of 3.21 deposited onto the planarized layer of the subsurface sample describe in 3.2.2. A schematic of the fabricated sample is shown in figure 3.5(a) with an optical image displaced in (b).

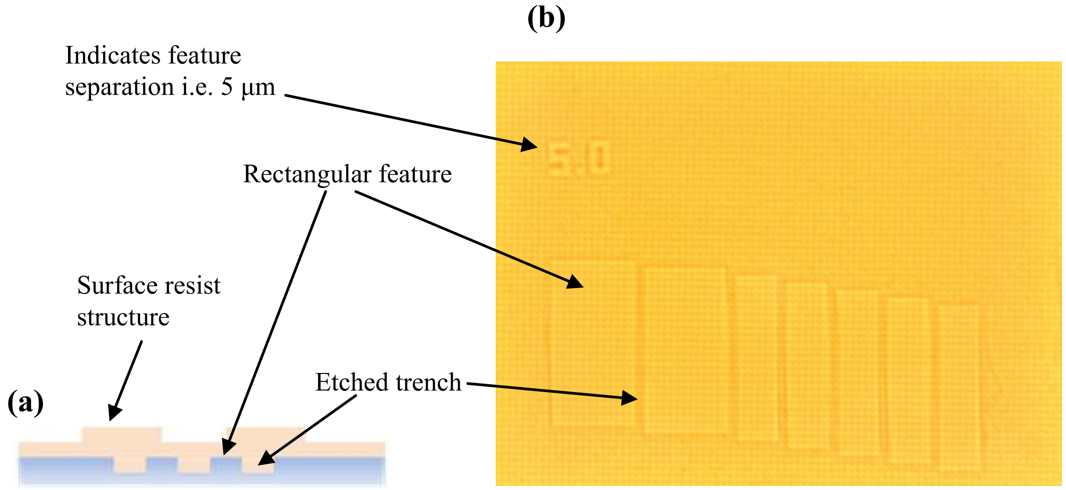

Figure 3.5: Image (a) is a schematic of the sample with both subsurface trenches and surface 2 micron resist circles. Image (b) is an optical image of one of the 5 micron array regions. The 5 microns features can be seen superimposed on the planarized subsurface trench features.

From image (a), it can be seen that the sample consists of surface resist features and planarized RIE etched subsurface micro-structures. Due to the transparent nature of the planarization resist, the underlying features are readily indentified as observed in image (b). It is however difficult to identify the surface resist structures since they are out of focus in the image and the magnification is low. The number at the top left indicates the separation distance of the rectangular features for the group shown. It must be emphasized that the schematic in 3.5 (a) is not drawn to scale and that six trenches are indicated in (b) whereas only three are shown in (a).

The second sample consisted of the same subsurface-feature sample but with human red blood cells deposited on the planarized layer instead of a resist pattern. Due to the group array nature of the features, it was possible to occasionally deposit red blood cells either partially or completely over an underlying trench by depositing a large number of cells in the general vicinity of the subsurface structures.

3.3 Biological Samples

The main focus of the research was the investigation of subsurface features in biological specimen. It was therefore necessary to have simple biological cells with and without salient subsurface features. Another requirement was that the cells needed to be easy to maintain (i.e. specific temperature or culture bath not required) and viable over a period of at least several hours. To avoid lengthy data acquisition times, samples less than 20 microns were investigated. Due to the z axis translation restriction dictated by the shear-force feedback PI circuit, it was necessary to image samples less than 8 microns in thickness. It was also important that selected samples were easier optically identifiable since the probe has to be placed as close to the bottom right of the sample as possible prior to each scan (scanning of the probe relative to the sample occurs from right to left and from the bottom to top). Taking all these factors into consideration, red blood cells were used as the primary biological cell for imaging. There are several recent publications [22-24] regarding quantitative phase imaging of these cells so it was possible to compared results when appropriate. An outline of the preparation procedures for the biological cells investigated is provided below.

3.3.1 Dried Red Blood Cells (RBCs)

Red blood cells or erythrocytes are interesting biological samples because of the contradiction of their physiological simplicity and functional complexity. They play a critical role in the transport of oxygen in living organism. In addition, these cells are readily obtainable and easily imaged in air. Human red blood cells lack a nucleus and can be considered to homogenous [5] with a refractive index of 1.41. A typical erythrocyte has a discoid (donut) morphology, is 7 microns in diameter and approximately 1 micron thick. The mechanism by which these relatively large cells are able to squeeze through blood capillaries half their size is not well understood. The physical characteristics of human red blood were desirable for my research in that these cells are easy to image and the results straightforward to interpret. The imaging of red blood cells throughout this investigation was performed in air and without staining. Samples were prepared by spreading a drop of blood over the surface of a quartz glass slide as shown in fig 3.6 (a). This resulted in a mono layer of well distributed cells as shown in figure 3.6 (b). It is clear from the image that these cells have a well-defined shape and size and are without any major intracellular components.

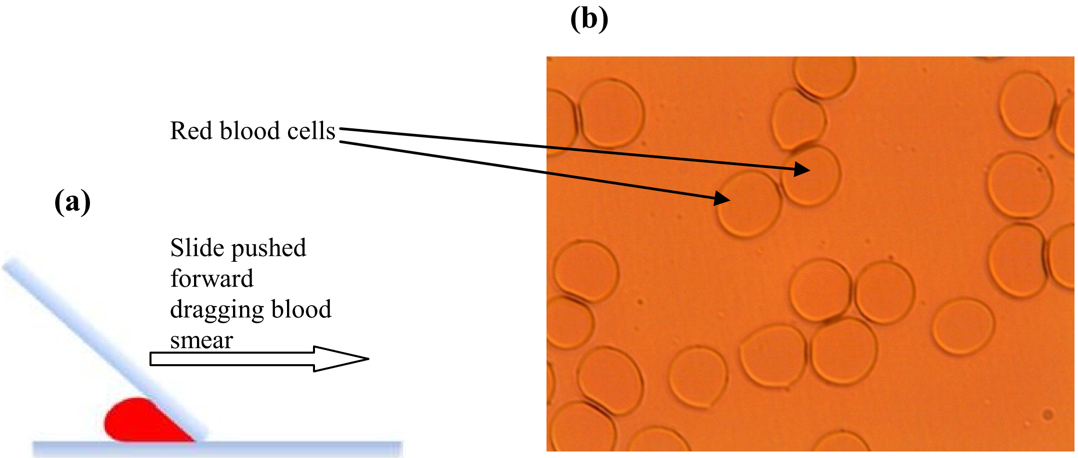

Figure 3.6: The schematic (a) illustrates the preparation procedure for the red blood cells sample. A drop of blood between two slides at an angle was spread thinly by moving the top slide forward. This results in mono layered cells. An optical image of a region of these cells on the sample is shown in (b).

3.3.2 Malaria Infected RBCs

Malaria is a disease which still affects numerous parts of sub-Saharan Africa and other third world countries. It is caused by one of several different malaria parasites and results in millions of deaths annually [70]. In my investigation, the parasite Plasmodium

Falciparum was investigated. This parasite is responsible for the most virulent form of malaria. In a laboratory setting, it is necessary to stain these cells before the parasite is visible but this step was unnecessary in my research. The stage of development of the disease can be determined from the morphology of the parasite and this was one of the objectives of this investigation. The sample was prepared by the method of Trager and Jensen [71]. The sample was rendered relatively safe to handle by rinsing the cells with methanol which effectively kills the parasite.

3.3.3 Fish's Red Blood Cells

Although mammals have enucleated RBCs; birds, amphibians and fishes all have nucleated RBCs. The RBCs in humans start off as nucleated cells in the bone marrow but these cells eventually lose their nuclei. The reason for this is still not known. However, I thought it would be interesting to compare and contract both nucleated and enucleated erythrocytes albeit from different species. The morphology and size of the nucleus is well correlated with the progress of pathological conditions such as cancer hence subsurface nuclear analysis is of great important. For this investigating, the red blood cells of the silver dollar fish (Metynnis Argenteus) were investigated. The sample was obtained from a "pet" fish and prepared in a similar manner to the human red blood cells.

3.3.4 White Blood Cells

White blood cells or leucocytes play an important role in helping the body ward off infections. Their relative abundance is a strong indicator of physiological diseases such as leukemia. There are several types of white blood cells, each with its specific role in fighting infections. These cells are differentiated by their size and the shape of their nuclei as seen under an optical microscope after staining. In this investigation, I sought to identify several leucocytes using quantitative phase imaging and subsequent analysis of their nuclear structures. These cells were identified in blood smear samples by meticulously sorting through the red blood cells. White blood cells appear translucent under a light microscope relative to red blood cells. They are generally larger and have an irregular shape so it easy to tell red and white blood cells apart. After imaging, the results were compared with standard optical images and previously published results.

3.3.5. Rat Fibroblast Cells

Rat fibroblast cells were obtained from the biology department at UNCC. These cells are much better suited for in-vivo analysis than red blood cells. It is difficult to fix RBCs in solution and as such motion artifacts are common. Fibroblast cells however, are easily fixed both in air and in a buffer solution. In addition, RBCs are surrounded by blood plasma in the body. This condition is difficult to reproduce in the lab. Fibroblast cells are normally surrounded by fluids which are similar in nature to buffered solutions such as phosphate buffer solution. These cells were image both in air and in PBS solution.

3.4 Summary

A series of fabricated structures and biological specimens were chosen to demonstrate and analyze the imaging capabilities of the multimode imaging instrument. The non-biological samples consisted of etched subsurface features with selected features deposited on top. The biological samples consisted of simple cells ranging in size from 7 microns to about 20 microns. After scanning each sample, a series of imaging processing procedures were performed to obtain the final images. These steps are highlighted in the next chapter.

CHAPTER 4: EXPERIMENTAL SETUP

4.1 General Setup

There are three primary requirements in an experimental setup for the simultaneous determination of quantitative phase, intensity and topography. The first is that the sample under investigation needs to be positioned and scanned to generate feature induced electronic signals. Secondly, optical and phase imaging requires at the very least, a light source, suitable optics and an interferometer such that physical characteristics of the investigated sample can be optically encoded. The final requirement is the detection and conversion of all optical signals into electronic signals, followed by the processing of all three signals to produce the final images.

As such, my experimental setup consists of three major components. At the core is an inverted optical microscope, modified to accept a NSOM head assembly. The assembly houses a turning fork/probe unit and a three axis controlled positioning stage. The second major component includes a fiber interferometer, optics and a light source. The third component consists of instrumentation for signal detection, feedback control and image processing. Image processing was performed post scanning using code written in Matlab. In this chapter, I will discuss each of the three components in detail and explain how they are integrated together to make the phase contrast NSOM possible. I will also discuss the modifications made to allow for imaging in a liquid environment at the end of the chapter.

4.2 Component 1: Inverted Microscope, NSOM Head Assembly and Precision Stage

In this section, I will review the details of the system's optics including the precision positioning stage and NSOM head assembly. These components constitute the core of the image acquisition system.

4.2.1 Inverted Optical Microscope

The Olympus IX50 inverted microscope was employed for visual positioning and inspection of the sample prior to scanning. In an inverted microscope, the sample is illuminated from above and the objective sits below the sample. This arrangement is absolutely necessary since the stage and head assembly must be positioned on top of the microscope. The head assembly houses the positioning stage, sample holder and PZT/tuning fork unit. Mounting the assembly unit onto an inverted microscope required a few modifications from the original design.

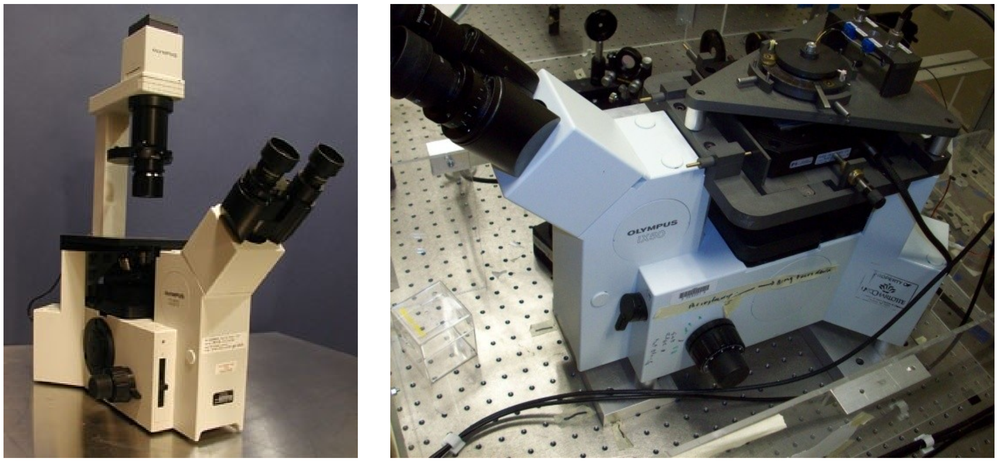

Figure 4.1: The left image if of the unmodified Olympus IX50 with an overhead light attachment. The right image is a modified version of the microscope used in this research. The NSOM assembly unit sits on top the microscope over the objective and sample.

The original and modified versions are shown in figure 4.1. A standard objective with a 10X magnification and 0.4 numerical aperture was used for all scans.

4.2.2 NSOM Head Assembly

The NSOM head assemble allows for fine positioning of the sample relative to the NSOM probe and coarse approach of the probe relative to the sample. The assembly consists of a base unit and a NSOM head unit and was designed and built by Ronnie Fesperman, then a graduate student in the department of mechanical engineering at UNCC. Schematics and optical images of this component are shown in figure 4.2.

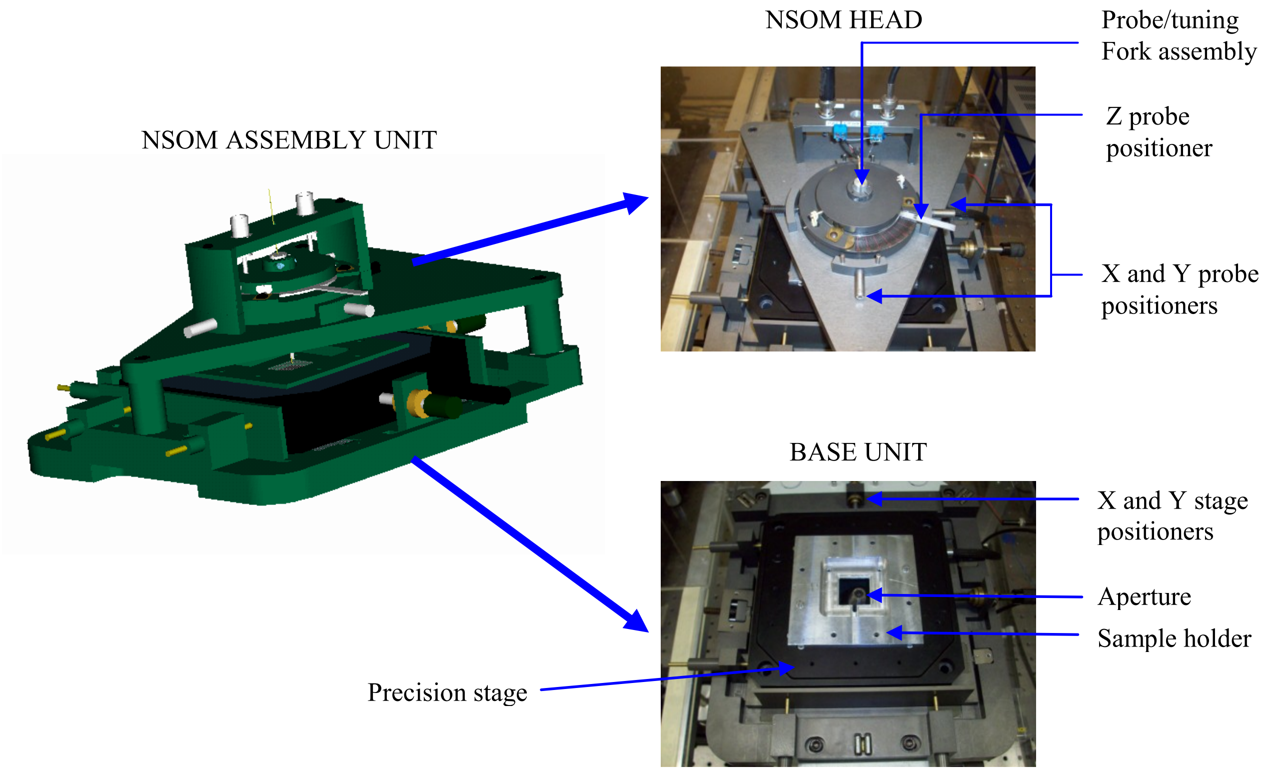

Figure 4.2: The image on the left is a 3-D rendering of the NSOM assembly. The top image on the right is an image of the NSOM head. The bottom right image is of the base unit. The objective lens of the microscope can be seen at the center of the sample holder.

The NSOM head houses the pzt/ tuning-fork assembly shown in figure 4.3. A quartz tuning fork is glued onto a mini-PZT and a fiber probe glued onto the fork. The PZT is electronically driven, causing the fork and probe to dither and a signal to be generated by the pieo-electric quartz tuning fork. This signal is utilized in fiber probe/sample distance regulation [72, 73]. The probe assembly can be moved in the x and y direction using the probe positioners of the NSOM head shown in top right image of figure 4.2. These degrees of freedom are important during optical alignment of the system. The probe can also be lowered or raised in the z direction with a maximum range of 1mm via the z positioned of the NSOM head. During near-field engagement, the stage is raised electronically by applying an increasing voltage to the z axis of the stage controller, to a maximum displacement of approximately 16 microns. If there is no near-field engagement, the voltage to the stage is then reduced to zero, and the z position moved 1/70 of 1mm or about 14 microns using a calibrated scale on the NSOM head. The stage is then raised electronically and the process repeated until near-field engagement.

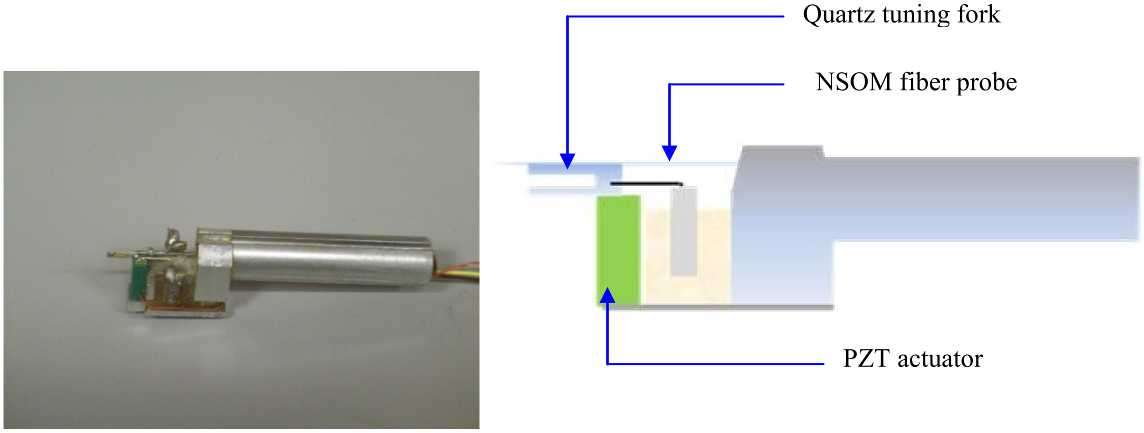

Figure 4.3: The left image is of the pzt/tuning fork assembly unit. The diagram on the right is a schematic of the assembly. The unit fits into a circular hole in the center of the NSOM head and is held securely in place. This represents the sensing unit of the shear-force feedback system.

The base unit allows the sample to be moved relative to the probe. The sample holder is attached to the precision stage which sits securely in the base unit. The x and y stage controllers shown in figure 4.2 allow movement of the stage and sample in these two directions. The base also has three magnetic receptacles which keep the NSOM head in place.

4.2.3 Precision Stage

In my setup, a PZT nano-positioner model P 527.2CL from Physik Instrumente (PI) with linear travel ranges in the X, Y, and Z directions of 200 microns was utilized.

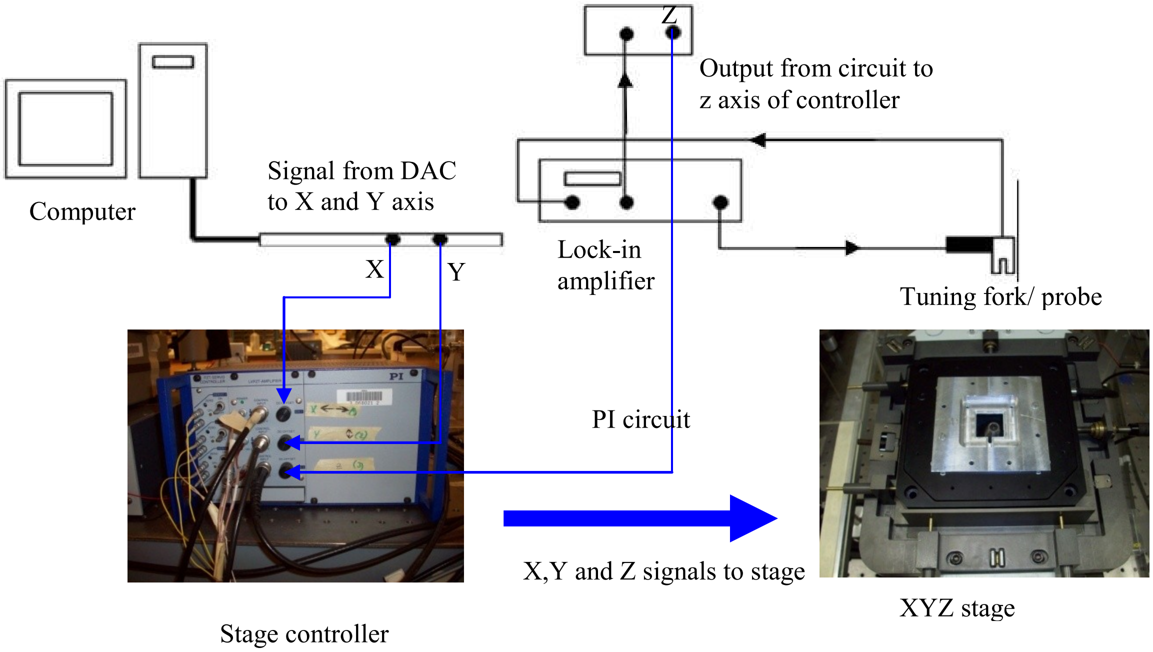

Figure 4.4: Controller for PZT precision stage. The x and y axis are controlled via a raster scanning program written in LabView. The z axis control voltage is generated as the output of a PI circuit which takes into account the dampening effect of the tuning fork with tip/sample separation.

The unit was controlled using a three-channel output position controller model E 509 from the same company. Z direction displacement is initiated by an error output voltage from a PI circuit which attempts to maintain tip/sample separation at a constant. The stage moves 2nm/mV in the z direction and 10nm/mV in the x and y directions. The scanning voltage was provided by a LabView program via a data acquisition (DAQ) board. The overall setup is shown in figure 4.4.

4.3 Component 2: Light Source, Fiber Interferometer and Optics.

4.31 Light Source

A helium-neon laser operating at 632.8 nm was used as the light source throughout the course of the investigation. The laser operated at 20 milliwatts with the plane of polarization parallel to the direction of the output. The relatively low power ensured that there was not excessive heating of the probe tip during the scans. It is well known that scanning a heated NSOM tip very close to biological samples can result in damage to the sample [74]. The single mode fiber utilized in our system required an operating wavelength near 630 nm for confinement hence our choice of the He-Ne laser.

4.3.2 Fiber Interferometer and NSOM Probe

Sample phase was determined using a part air, part fiber hybrid interferometer. The fiber interferometer consisted of a bi-directional coupler with a portion of one of the output arms tightly wrapped around a cylindrical PZT transducer as shown in figure 4.5. The PZT is phase modulated at1 kHz via a signal from a signal generator. A secondary signal from a PI circuit is also sent to the PZT to maintain the environmentally induced optical path length difference between the reference and sample arms at a constant. As shown in figure 4.5, light from a He-Ne laser is launched into one of the two input arms. A fiber NSOM probe is spliced into the sample arm using a fusion splicer. This probe is fabricated by etching in hydrofluoric acid followed by coating with aluminum. The details can be found elsewhere [17, 75]. Prior to splicing, the length of the probe is adjusted so that the sample arm length is exactly equal to the reference arm length of 52.5 cm. The second input arm is used to detect the back-reflected light from the output ends. This signal is used to help maintain environmental stabilization. Three pressure plates in the reference arm help to control the polarization state of the back-reflected light and improve the fringe contrast or visibility.

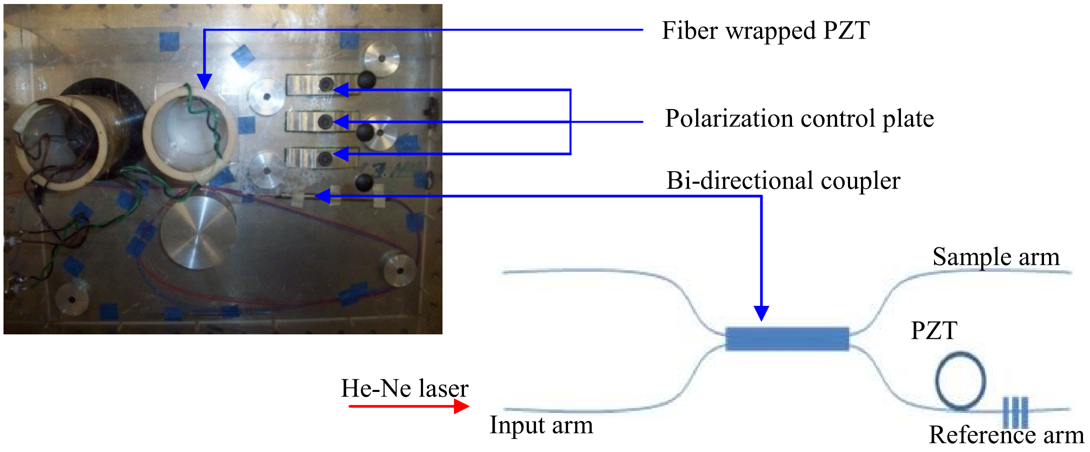

Figure 4.5: The left image is a top view of the bidirectional coupler enclosed in a plexiglass housing. Although two PZTs are present, only one is actively used. The three black circles on the left are cap covered accesses to polarization adjustment plates inside the housing. A schematic of the setup is shown on the right.

The plates which sit on top of a section of the fiber, can be tightened or loosen thus changing the birefringence and polarization state of the light in that arm. With the exception of small sections of each arm, the coupler is enclosed in a small plexiglass housing to help provide some additional environmental stability. This housing, the inverted microscope and optics, are all enclosed in a larger plexiglass housing shown in figure 4.7.

4.3.3 Optics

The output arms of the fiber interferometer forms the input arms of an air Mach-Zehnder interferometer as shown in figure 4.6. The sample under investigation sits on a precision stage positioned beneath the probe. Sample phase is determined via signal processing of the Fourier components of the output signal. The resulting phase is calculated as the inverse of the tangent function and consequently, the maximum phase which can be measured without unwrapping is 360 degrees. For samples with features greater than about 1.3 microns, phase unwrapping is required. To circumvent this inconvenience, a novel approach was prescribed which makes use of a 1mm square thin glass plate attached to a galvanometer for phase determination. The galvanometer and angular displacement plate are inserted into the reference arm and are shown in figure 4.6.

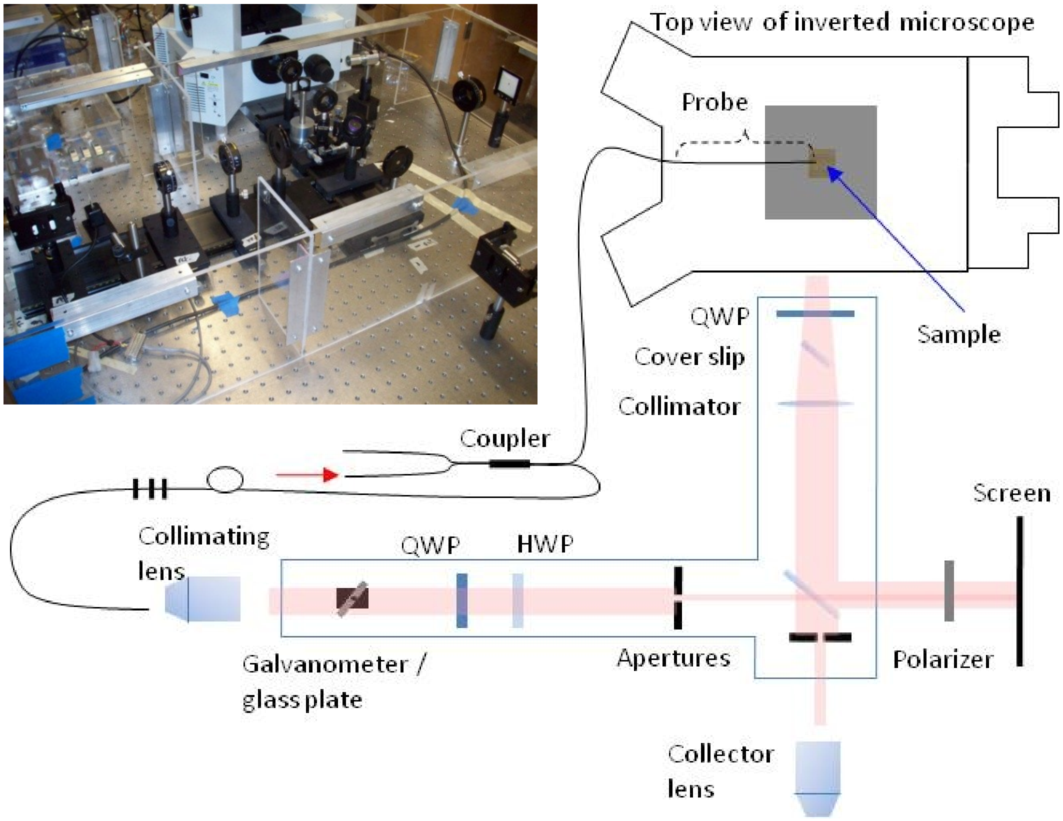

Figure 4.6: On the left is an image of the Mach-Zehnder interferometer used for phase determination. The right image is a schematic of the setup. QWP and HWP represent quarter wave plate and half wave plates respectively.

The effective determination of sample phase requires that the fringe contrast on the output be as high as practically possible. This is achieved using a quarter and half wave plates in the arms of the Mach-Zehnder interferometer as shown in figure 4.6. Both arms of the interferometer contains quarter wave plates which convert the elliptically polarized light which results from the natural birefringence of the fiber coupler and induced birefringence of the polarization adjustment plates, into linearly polarized light. The half wave plates rotate the plane of polarization. In the case of the sample arm, the linearly polarized light is nearly extinguished by adjusting the polarization state of the polarizer to the right of the beam splitter, with the reference beam blocked. Then with the sample beam blocked off and the polarization state of the polarizer unchanged, the quarter wave and half wave plates in the reference arm are adjusted until the light is extinguished by the polarizer. At this point, the light from both arms are linearly polarized and have the same polarizations states, thus maximum fringe contrast is achieved.

4.3.4 Enclosure

As mentioned before, a simple enclosure was built around the entire system to provide some degree of isolation from external thermal sources. A photograph of the plexiglass enclosure box is shown in figure 4.7. There are several removable lids and a flap opening which allow access to the components inside.

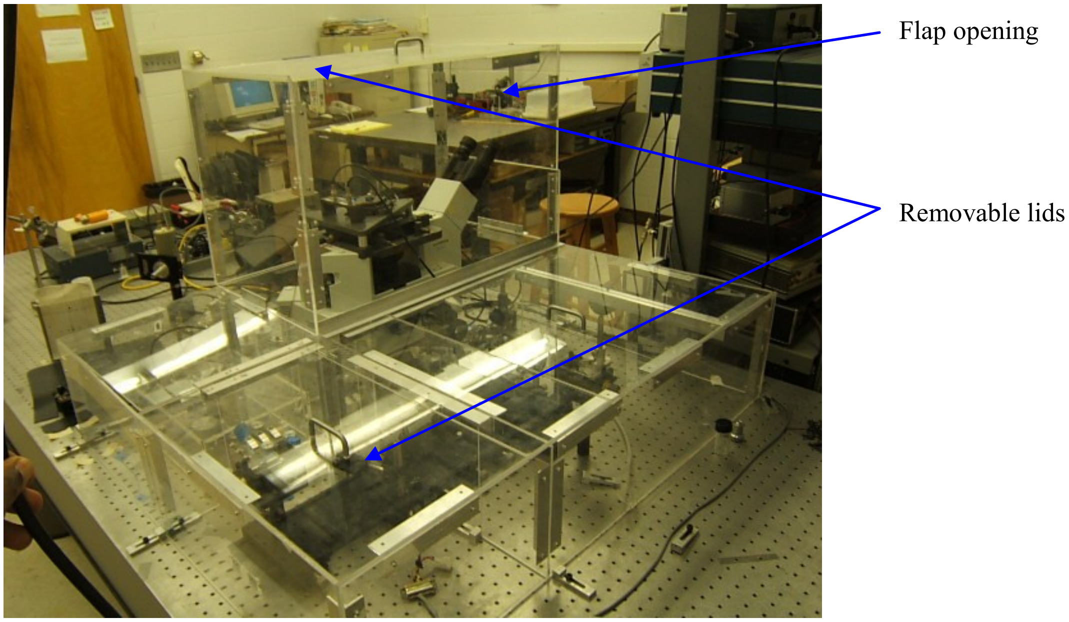

Figure 4.7: Environmental isolation enclosure for system. The top piece shown in the diagram can be removed completely. Access to the microscope is also available through the removable lid at the very top or through the flap opening shown in the diagram.

4.4 Electronics and Software

Image generation in the phase contrast NSOM requires the conversion of optical signals into electrical signals, the electrical signals into binary data and the subsequent processing of this data. These important aspects of the imaging process will be discussed in this section from the instrumentation point of view.

4.4.1 Signal Generator

A 2 MHz sweep/function signal generator was used throughout my investigation. The generator was operated at 1 kHz with the main-out signal sent out environmental stabilization feedback circuit and the auxiliary signal used as a reference for the lock-in amplifiers in the setup.

4.4.2 Lock-in Amplifiers

Four lock-in amplifiers were utilized in the experimental setup of the phase contrast NSOM. Each amplifier was referenced at 1 kHz. An amplifier is used as part of the feedback system for stabilization. It monitors the first harmonic term of the back-reflected signal and sends an output signal to the stabilization PI circuit. The circuit then outputs an error signal to the fiber wrapped PZT. Two lock-ins are used during the phase determination procedure. The first measures the first harmonic voltage of the output while the other measures the second harmonic voltage. The second lock-in also evaluates the ratio of the first and second harmonics voltages and sends a ratio signal to a separate PI circuit. The PI circuit then transmits an error signal to the galvanometer. The final lock-in serves a dual purpose. It functions as a signal generator for the PZT attached to the tuning fork and also monitors the signal generated by the tuning fork. An output signal is sent from this lock-in to a third PI circuit. This PI circuit sends an error signal to the z axis control of the precision stage which maintains constant tip/sample separation during the scanning process.

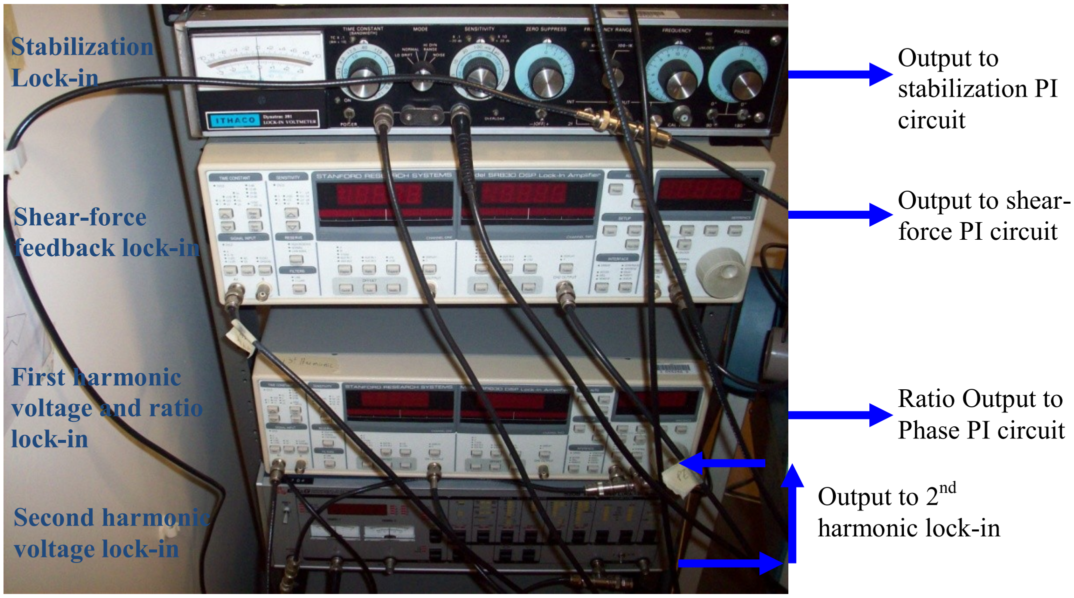

Figure 4.8: The four lock-in amplifiers utilized in the experimental setup are depicted in the image shown. Three of the lock-ins outputs voltages to PI circuits. The second harmonic lock-in outputs a voltage to the first harmonic lock-in which in turn outputs a voltage proportional to the ratio of the two signals.

4.4.3 Feedback Circuits

Three PI circuits are used in the setup as mentioned in the previous section. The circuits are used for environmental stabilization, phase determination and maintaining constant tip/sample separation during a scan. The details of operation were previously reviewed in chapter 2 and further details can be found elsewhere [17].

4.4.4 Oscilloscope

An oscilloscope was used to monitor the output and back-reflected signals generated by the system. Since these signals have well defined characteristics, the oscilloscope allowed for the immediate determination of any obvious problems with either signal. All signals were pre-screened with the oscilloscope before connecting them to the lock-ins

4.4.5 Spectrum Analyzer

The phase determination process requires that the first and second harmonic voltages be equalized. This is achieved by adjusting the amplitude of the modulation signal at the signal generator. The spectrum analyzer allows for visual monitoring of the amplitude of each signal and electronic verification of equalization of the two voltages.

4.4.6 Detectors

Throughout the course of this investigation solid state photo-diode detectors with 632.8 nm filters were utilized. A total of three detectors were used to monitor the back-reflectance, output and intensity signals. The intensity signal was generated by placing a thin glass cover slip in the sample arm of the interferometer as shown in figure 4.6, to act as a beam splitter. The signal from each detector after amplification was in the millivolt range.

4.4.7 Data Acquisition Board

Finally, all intensity, phase and topography signals were routed to a desktop Pentium II personal computer running windows 98. Data acquisition was realized using a National Instrument model BNC-2090 data acquisition (DAQ) board. The DAQ board was connected to the computer via a PCI interface card.

4.4.8 In-Vivo Imaging

In vivo imaging of biological cells requires that the cells be imaged in a liquid environment. The “natural” environment of biological cells is an aqueous solution. Just as important is the fact that cells quickly dry out in air. The main concerns with NSOM imaging in a solution are liquid loss due to evaporation and Q-factor loss due to increased damping. Without liquid replenishment, changes in the liquid height due to evaporation throughout a scan would result in image artifacts. To deal with this issue, a liquid replenishment system was designed. The main strategy employed in the system is to maintain a very thin film of liquid above the sample during scanning. This ensures that damping is kept at a minimum and a high Q-factor can be achieved. To meet this objective, a 3cm diameter o-ring is positioned in the liquid on top of the sample.

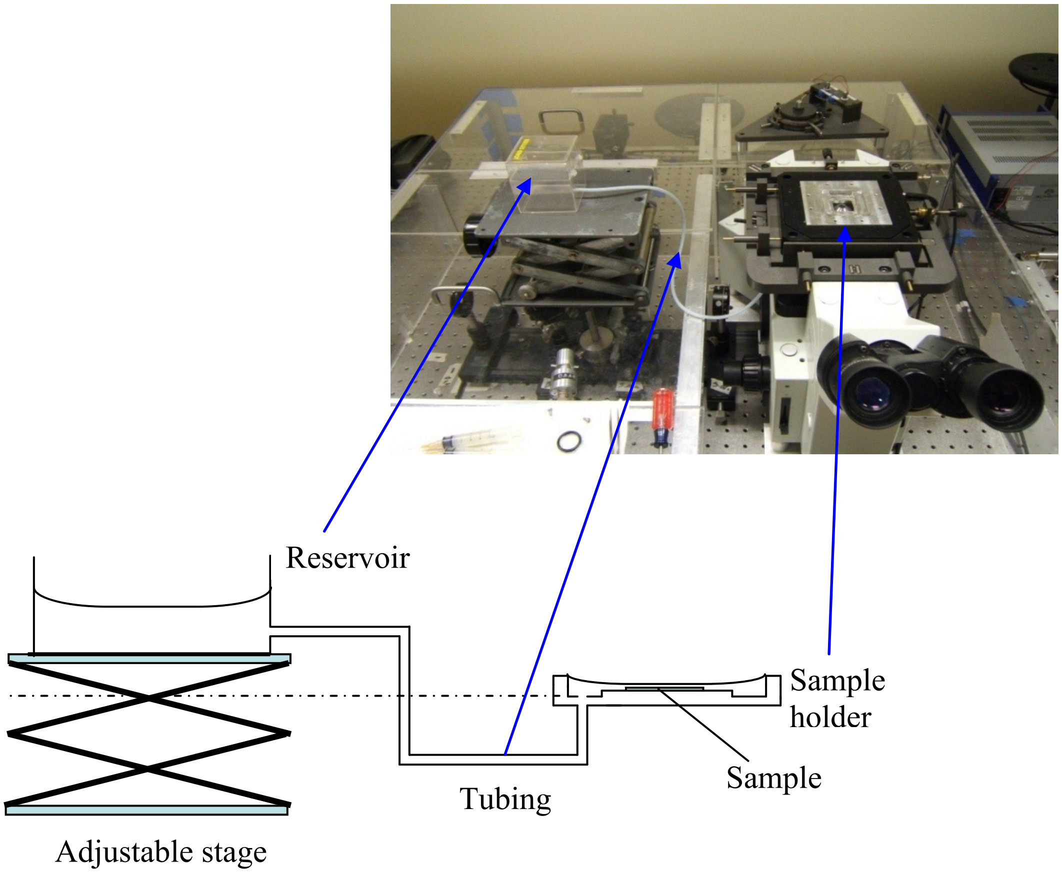

Figure 4.9: The top image is of the actual experimental setup for liquid imaging and the bottom image is a schematic of the liquid replenishment system. As liquid evaporates from the sample holder, it is replenished by the reservoir.

The meniscus formed at the face of the ring leads to a thin film over the surface of the sample as shown in figure 4.10. This approach proved quite effective in imaging both biological and non biological samples in a liquid environment.

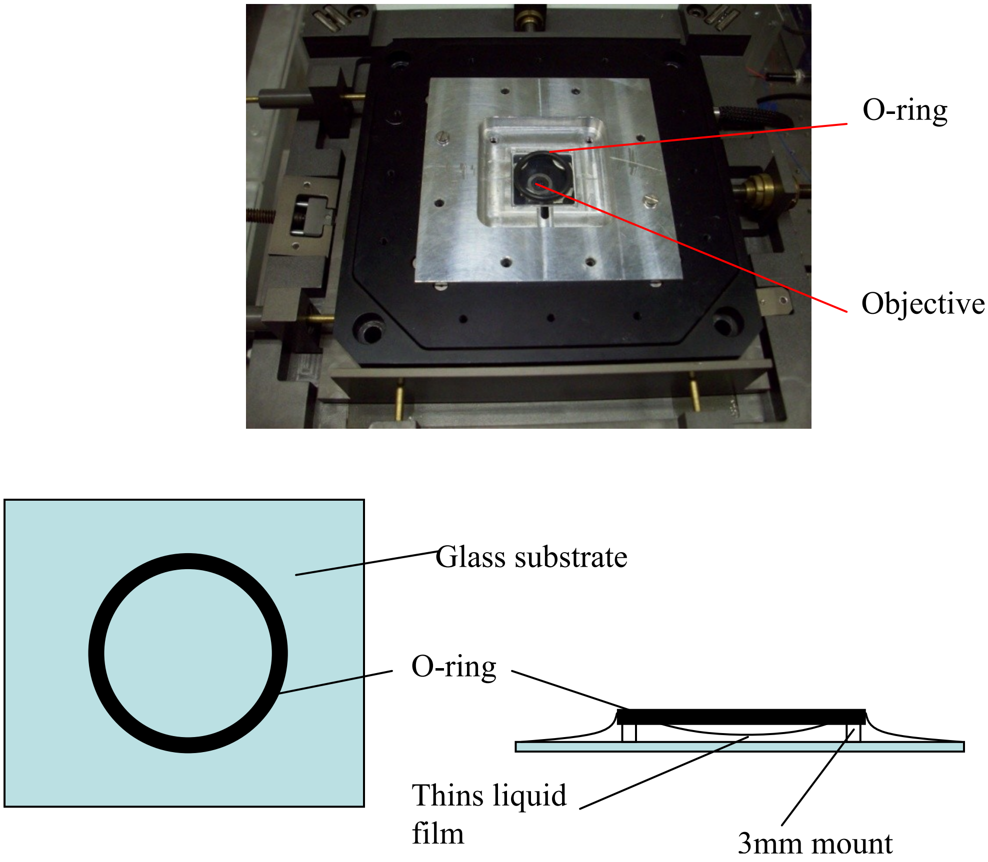

Figure 4.10: An image of the o-ring positioned on top a glass substrate sitting over the lens objective of the inverted microscope is shown (top). The bottom image is a schematic representation of the ring and substrate depicting the formation of a negative meniscus on the surface of the substrate/sample.

4.4.9 Software

The original code for data acquisition was written in LabView by Michael Riley, a past member of the research group. The code has since been modified to accommodate a ratio signal instead of individual first and second harmonic voltages. This change was implemented as the research transitioned from measuring phase using the tangent function to unambiguous phase determination. At the DAQ board, the analog signal from the detectors and circuits are converted into digital signals to be processed and interpreted.

4.4.9.1 Raster Scanning

During the scanning process, voltage signals generated by a LabVeiw program are used to position the precision stage in the x and y directions. LabView (version 5) software was used to perform both raster scanning and the acquisition of the voltage values required to generate all images. In each instance, the data was stored as a two dimensional data array in a proprietary format which was subsequently converted to a Microsoft Excel file for processing. Since in a raster scan odd numbered lines are scanned in the opposite direction, a post imaging line scan correction was required.

4.4.9.2 Image Processing

All the image processing was performed using MatLab. Ronnie Ferperman wrote the initial code for generating the three dimensional representation of the data and for some basis image processing such as slope removal. Since then I have substantially rewritten all the old code and included several new algorithms to allow for greater efficiency and functionality. Some of the details are reviewed in chapter 5. The improvement includes better slope removal, improved 3-D representation and noise filtering. New codes were written for image registration and image subtraction. Image subtraction is required during the extraction of subsurface information from the phase data. The subtraction process results in difference residue errors which led to a separate program being written to minimize this error. It was determined after careful observation that there was a lateral shift between successive line scans during the scanning process. This error due to hysteresis of the precision stage was also corrected using Matlab code. Much of the details are reviewed in chapter 5.

4.5 The Phase Contrast NSOM

The phase contrast NSOM allows for tri-modal high resolution in vivo imaging. Before this can be achieved, there are several important steps which need to be followed as part of the setup. The first step in imaging requires that the sample and probe be engaged in the near field.

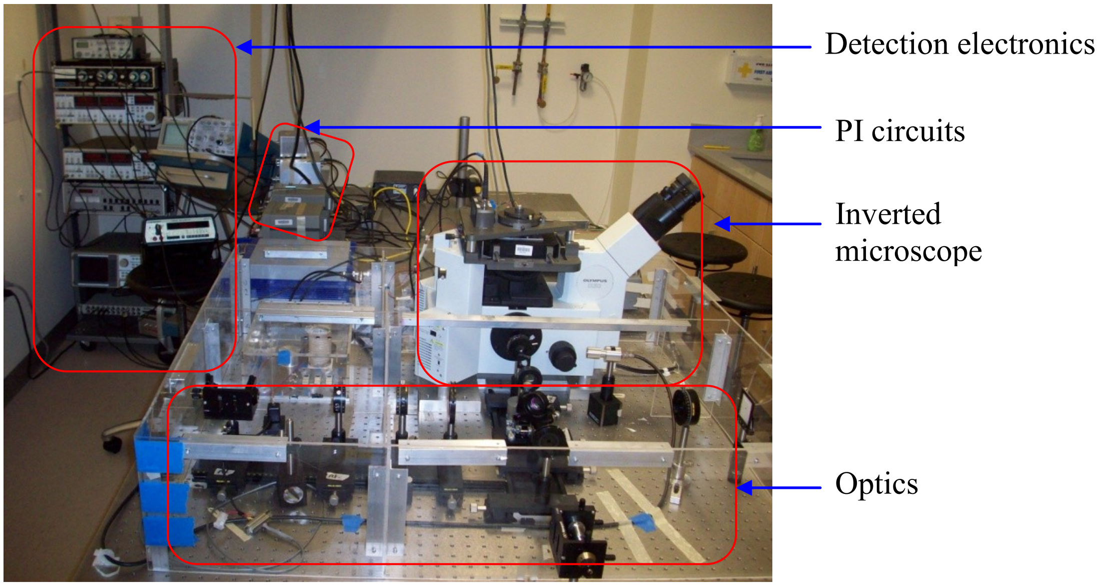

Figure 4.11: This is an image of the complete system. The detection electronics are on the left. Up front are the optical components and the inverted microscope is toward the right.

Once this is done, the stage is lowered several microns using the electronic z –axis fine adjustment and the optics aligned. This usually takes about 20 minutes. After this step, the probe is visually positioned near the region of the sample to be imaged and the sample re-engaged in the near field. With the sample engaged, the phase detection and stabilizations circuits are turned on. During a scan, the time interval between data acquisition points is 100 ms with a step size of about 100 nm. Thus a 15 microns by 15 microns scan size with 100 pixels in the x and y directions takes approximately 20 minutes. The post imaging processing has been streamlined to the point where the final images are available a few minutes after each scan. The details of this part of the process is explored in the next chapter

CHAPTER 5: IMAGE PROCESSING

5.1 Data Acquisition

During a sample scan, voltage values from the intensity amplification circuit, phase PI circuit and shear-force feedback PI circuit are channeled to three of the available sixteen inputs of the DAQ board. The BNC 2090 DAQ board used throughout the investigation has only two outputs which were used for X and Y positioning of the precision stage. The line scan voltage values for each signal are represented graphically in LabView, as the scan progresses. This provides real time information on the progress of each scan and an early indication of any potential problem, in which case the scan can be terminated. At the end of the scan, the three datasets corresponding to the three different imaging modalities are stored as two dimensional arrays of voltage values in a LabView proprietary file format. The files are subsequently converted into Microsoft Excel files and imported into Matlab for processing. Throughout this research, acquired tri-modal datasets are represented as pseudo-color rendered three dimensional images. In the case of the shear-force feedback and phase data, the corresponding voltage values are usually converted to topography height values in nanometers or microns using appropriate conversion factors. The intensity information is expressed in arbitrary units.

In this section, I will review the steps involved in converting each Excel file into a three dimensional image representation. All post processing procedures such as slope removal and filtering will be discussed in detail. Finally, I will discuss the steps involved in extracting the subsurface information from the phase data using the topography data and present both simulated and experimental results to demonstrate the process.

5.2 Pre-Plotting Image Processing

Prior to conversion of the original two dimensional data arrays into three dimensional images, the data needs to be pre-processed. This step involves the reversal of alternate lines, removal of slope from the data and a correction for scanning hysteresis. Each of these procedures is further expanded below.

5.2.1 Line Reversal

In a typical scan, the probe moves from the left to the right relative to the sample (i.e. the sample which sits on the stage moves from right to left) in the initial line scan. At the end of this line scan, the probe moves forward by a specified distance, and the scan continues from right to left. This process continues until the specified region of the sample is scanned. Therefore, alternate lines in the scan need to be reversed. The original LabView files are converted to Excel files and the line reversal procedure and all subsequent processing is perform in a Matlab environment.

5.2.2 Slope and Curve Removal

Square quartz glass substrates of 1mm thickness and 1″ dimensions were used for both the fabricated and biological samples. The lateral dimensions of the sample correspond to the size of a grooved sample-receptacle of the sample holder. Larger substrates need to be modified accordingly or placed on top the 1″ substrate. Imaging of the glass slides with a white light interferometer verified that surfaces were not “perfectly” flat. Another cause of image slope is the gradual heating or cooling of the laboratory environment. A third cause is due to the fact that the substrate is slightly tilted relative to the probe while positioned in the sample-receptacle. Figure 5.1 shows a phase image of an RIE etched trench in a glass substrate with and without slope removal. After slope removal, it is much easier to ensure that the phase and SFF images lie on the same plane prior to further processing. This is a critical step in the registration process prior to image subtraction.

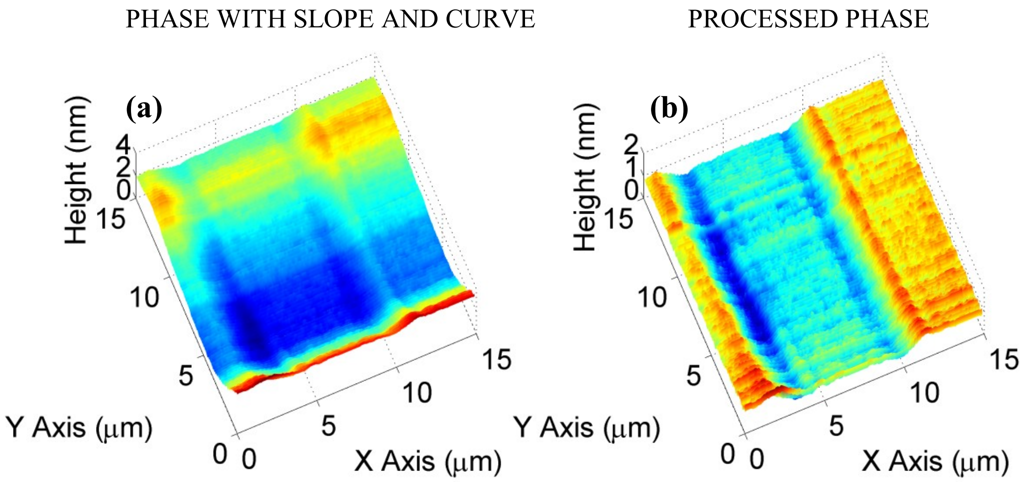
PHASE WITH SLOPE AND CURVE

PROCESSED PHASE

Figure 5.1: Figures (a) and (b) represents phase images of a RIE etched trench before and after slope removal respectively. A gradual slope is observed in image (a) together with significant curvature. After processing, the slope and curve are effectively removed as shown in (b).

Slope removal is performed via an interactive process. At least three points on the substrate are interactively selected from a two dimensional representation of the two data sets. The objective is to remove any slope present in the substrate. This is accomplished by fitting a plane to the substrate then subtracting the plane from the original data. We can write the equation of a plane as;

$$ax + by + d = cz \tag{19}$$

where a, b, c and d are constants. Thus if we consider a series of selected points z_1, z_2, z_3...z_n from the original dataset with coordinates (x_1, y1), (x_2, y2), (x_3, y3)… (x_n, y_n), we can write;

$$kX = Z \tag{20}$$

$$X = k^{-1}Z \tag{21}$$

where k is a n x 3 matrix with the nth row containing the elements x_n, y_n and 1; X is a 1 x 3 matrix with the coefficients a, b and c; and Z contains elements z_1 through z_n. Thus X coefficients are determined using the inverse of the matrix k. A plane is built up with dimensions determined from the size of the original dataset using these coefficients. This best fit plane is then subtracted from the original data. When imaging in a liquid, it was difficult to maintain environmental stability. The result was that there was a pronounced curve in the phase over a time interval of several minutes. This can be corrected by fitting a curve to a one of the edges of the substrate and subtracting this information from the original data along a direction orthogonal to the edge. During this process, extreme care must be taken to ensure that the features of interest are not affected by the process. It was nevertheless fairly easy to remove any gradual curvature in the topography and phase data. The intensity data did not demonstrate these effects.

5.2.3 Hysteresis Correction

As the sample is moved in a particular direction during a scan, an increasing voltage is applied to the appropriate axis controller of the stage. As the sample is scanned in the opposite direction, the voltage is gradually decreased. However, the path travelled in one direction is slightly offset with respect to the other direction of travel. This offset has a constant value for a given scan range and is corrected for post-scanning by shifting alternate lines by a few tens of nanometers relative to the other lines. This effect is minimal for small travel ranges.

5.3 3-D Plotting

After the initial processing, the data is typically represented in a 3-D topography format (i.e. the z axis is expressed as a height value. The lateral displacement voltages used for raster scanning is converted to displacement distances in the x and y directions using the conversion factor 1mV equals 10nm.

5.3.1 Topography

The shear-force feedback voltage is converted to a height value using the conversion factor 1mV equals 2nm. The data is represented as pseudo color rendered 3D images using code written in matlab. Any slope or noise is subsequently removed.

5.3.2 Phase

The phase compensation voltage to the galvanometer is converted to a height phase value using a calibration curve as previously explained. The phase value in degrees is then converted to a height value using.

$$h = \frac{0.6328(\Delta\theta)}{360(n_{ave} - 1)} \tag{22}$$

where $\Delta\theta$ is the phase in degrees and n_{ave} is the average refractive index of the sample. If necessary, slope removal and filtering is performed to produce a final image. For the image subtraction process, the phase is not converted to a height value since n_{ave} is not constant as is usually assumed. Instead, the topography height is converted to a phase value as seen later.

5.3.3 Intensity

There is little processing performed on the intensity data. The voltage values are not converted to any other form. The only processing performed is a vertical shift such that the lowest point in the data corresponds to zero. Another noteworthy point is that the intensity image is inverted so that it corresponds to the topography.

5.34 Noise filtering

It is sometimes necessary to filter out high frequency noise from the final data. Inherent noise is always present in the system but the effect is exacerbated when the optical light signals are low or the feature height is a few hundred nanometers. This condition is easily remedied by filtering out high frequency components in the frequency domain followed by an inverse transform. This step is typically unnecessary for microscopic specimens such as biological cells.

5.4 Subsurface Imaging

There are three processing stages involved in the extraction of subsurface information from the phase data. The first step involves registration of the two data sets. This is followed by the conversion of the topography data into phase information followed by an image subtraction. The final data is usually expressed in degrees unless the refractive index of the subsurface feature is known.

5.4.1 Image Registration

Registration was accomplishing using Matlab code which allowed a corresponding point in the SFF and phase data sets to be manually selected followed by the relative translation of one of the data sets such that the selected points coincided. This procedure was fairly simple but there are numerous techniques available which are far more sophisticated [76-77]. For example, if one image is of a small size (i.e. smaller dimensions) compared to the other, registration may be performed using a cross correlation. If the unregistered images are the same size, it is possible to crop one of the images before performing a cross correlation. I investigated both approaches and the manual method proved more reliable. It was very important that slope in the original data sets be removed to ensure reliable registration. Once this condition was met, excellent registration was routine.

5.4.2 Data Conversion

Before subtraction, the topography data was converted to phase information using equation 4 and solving for $\Delta\theta$. This was discussed in chapter 2. The sample in concerned is assumed to be homogenous with a constant refractive index n_{ave}. In the case of a cell, the refractive index of the cytoplasm was taken as the average refractive index value. The conversion of the height to phase step was followed by image subtraction.

5.4.3 Image subtraction

The shear-force data after conversion to phase data was subtracted from the quantitative phase data. This was performed via a simple subtraction algorithm and the absolute difference determined.

5.44 Residue error suppression

A residue difference error is always obtained when two images are subtracted unless there is perfect alignment. In this investigation, I approached this problem by attempting to suppress sharp spikes in the difference data. To illustrate, the procedure employed, simulated results are presented. Figure 5.2 explains the origin of the residue error.

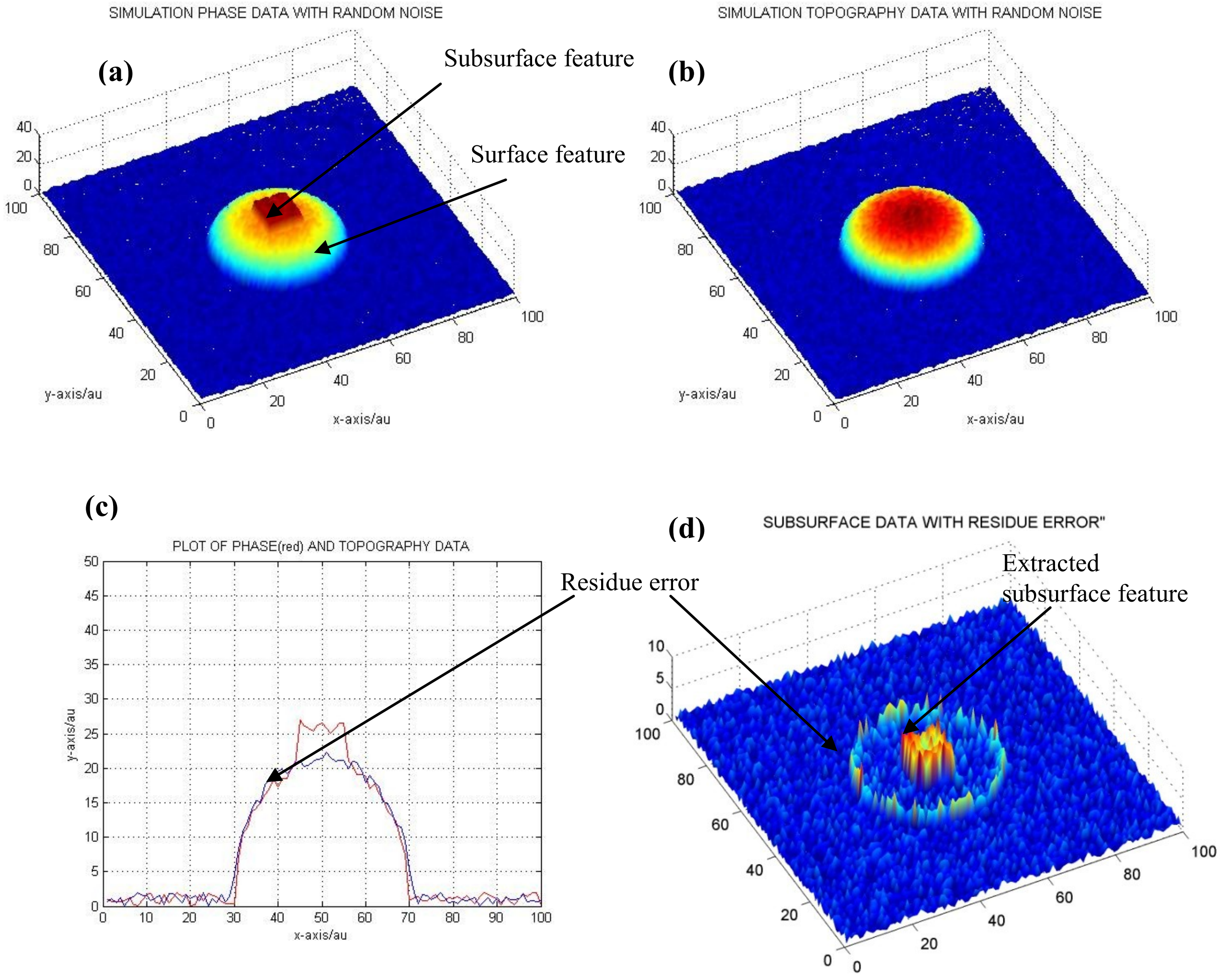

Figure 5.2: Image (a) is a simulated 3D phase representation of a sample with a central subsurface feature. Image (b) is a simulated topography image of the sample. Line scans from each simulated data set are shown in (c). The two images are not perfectly registered and thus a residue difference error is results after subtraction (d).

To minimize the residue error, I attempted to selectively suppress sharp spikes in the difference data (difference of phase and SFF data). Before performing this step, I attempted to predict the location of the spikes by examining the gradient of the topography data. One would expect a high gradient at surface feature boundaries of the topography image and this is precisely where sharp spikes will occur in the difference data. The gradient of the phase data would indicate spikes at the boundaries of the surface features, but also at the subsurface features. It would not be advisable to suppress any data near the subsurface feature since this could lead to loss of "real" data, hence my rationale for using the topography data.

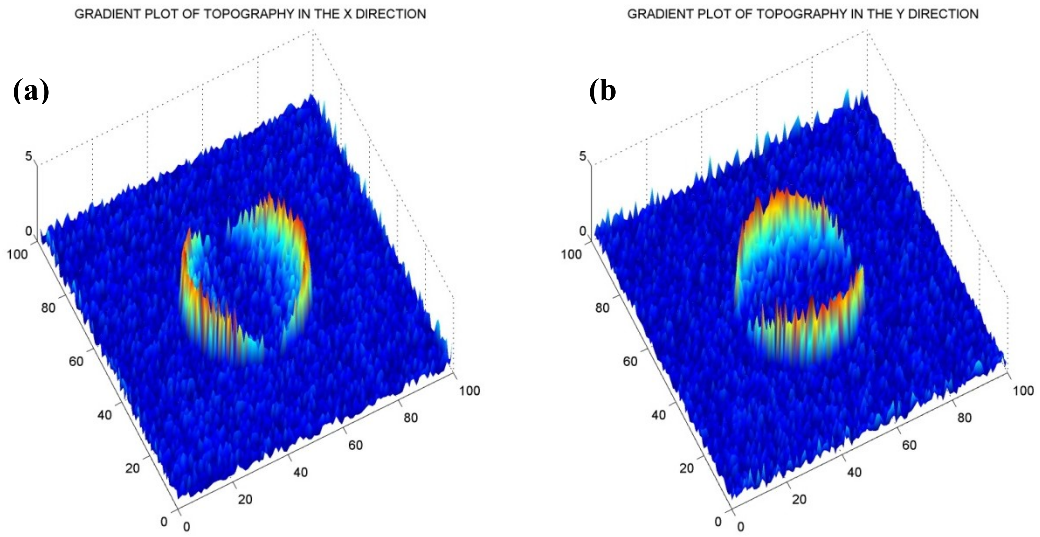

Figure 5.3: Image (a) is a plot of the gradient function in the x direction for the topography data. Image (b) is a plot of the gradient function in the y direction. The spikes in the two images occurs at the surface feature boundary and coincides with the location of the difference reside error in figure 5.2 (d).

Once the location of the spikes has been determined, a threshold is set which will determine which spikes will be suppressed. This is accomplished by sampling the background of the gradient image i.e. I chose points from the gradient image which are away from the spikes and find the average of these points. The threshold chosen depends on the nature of the sample but is usually 5 times the background "noise".

The residue noise suppression algorithm suppresses spikes when they are found at any point in the data, by searching for the nearby neighbor from a group of neighbors in a defined interval, which result in the smallest difference error. This interval is defined by the relative shift between the two unregistered data sets which is obtained from the registration algorithm. For example, in figure 5.4, during the subtraction process, points *A* and *A'* when subtracted from each other will leads to a spike. My algorithm searches for points around A which lie within the interval of the relative shift between the unregistered images, and selects the point which results in the smallest difference.

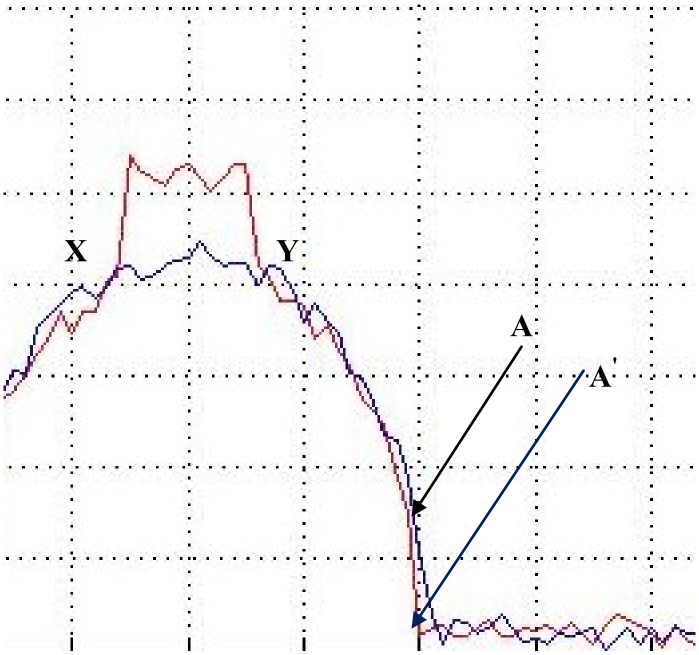

Figure 5.4 Indicates the line scans for the simulated phase date (red) and the topography data (blue). The phase values in the range X to Y are greater than any other values in the topography line scan, hence they must correspond to the subsurface feature. A residue error occurs when A' is subtracted from A which is corrected using the noise suppression algorithm.

Since this process is computationally intensive, spike suppression is not performed when not required. For example, the phase points between X and Y have a greater value than any other topography points in the line scan. Thus they are automatically chosen as “real” data points in the subsurface image without any processing.

The results of applying the algorithm are shown in figure 5.5. Image (a) represents the extracted subsurface feature without suppression while (b) represents the results with suppression. It is observed that the noise is significantly reduced but that the subsurface feature is unaffected. This procedure allows fine detail to be preserved in the subsurface result.

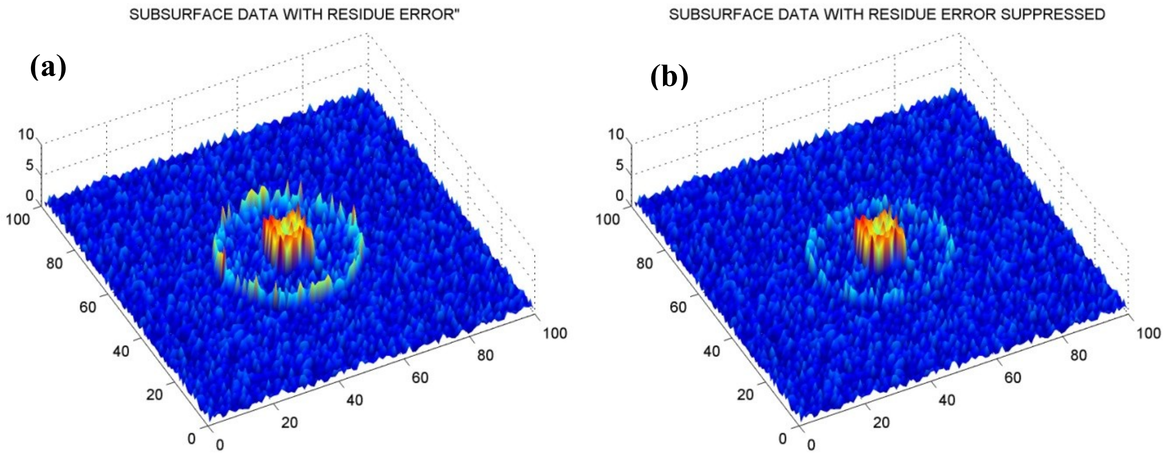

Figure 5.5: Image (a) is the extracted subsurface image obtained by subtracting the two data sets and taking the absolute value of the difference. Image (b) is the extracted subsurface result employing the spike suppression algorithm described in this section. It can be seen that the error is reduced but the subsurface feature is unaffected.

This algorithm is well suited for simple cells but does not always perform as well with not biological samples. The code work best when the subsurface feature and residue noise are well separated.

5.5 Summary

The phase, topography and intensity data sets are all represented as pseudo color rendered 3D images throughout this work. Before this can be accomplished, the data must be pre-processed to remove all slope and noise. Subsurface feature extraction involves subtracting the shear-force feedback data converted to phase, from the quantitative phase data. The two images must be well registered before the subtraction. Subsequent suppression of sharp peaks allows subsurface information to be extracted.

CHAPTER 6: IMAGING IN AIR

6.1 Introduction

The results of this research can be subdivided into imaging in air and imaging in a liquid environment. In this chapter, the results of the former are presented and the later results are presented in chapter 7. Throughout this research, both fabricated non biological samples, and biological specimens were investigated.

My master's thesis research was based on an investigation into the near-field phase imaging of selected samples. The goal was to extend the phase contrast capable NSOM to the imaging of biological specimens. Since these specimens are relatively thick (greater than 1 micron), it was necessary to design a novel phase detection scheme which allow for real time unwrapping [78]. Although a successful system was implemented, the detected phase was intensity dependent as explained in chapter 2. Nevertheless, human and rat red blood cells were imaged without the need for post scanning phase unwrapping which plagued my prior research [17]. It is worth making the clarifying point that most of my earlier images were not near-field images since the sample thickness often exceeded 500nm. However, high spatial phase resolution was demonstrated by resolving 100 nm separated lines in a PMMA sample [78]. In this case the sample thickness was only 220 nm and as such, high resolution near-field imaging was possible. The samples imaged were generally homogenous and lack any significant subsurface features. As such, it was possible to define each sample by an average refractive index value.

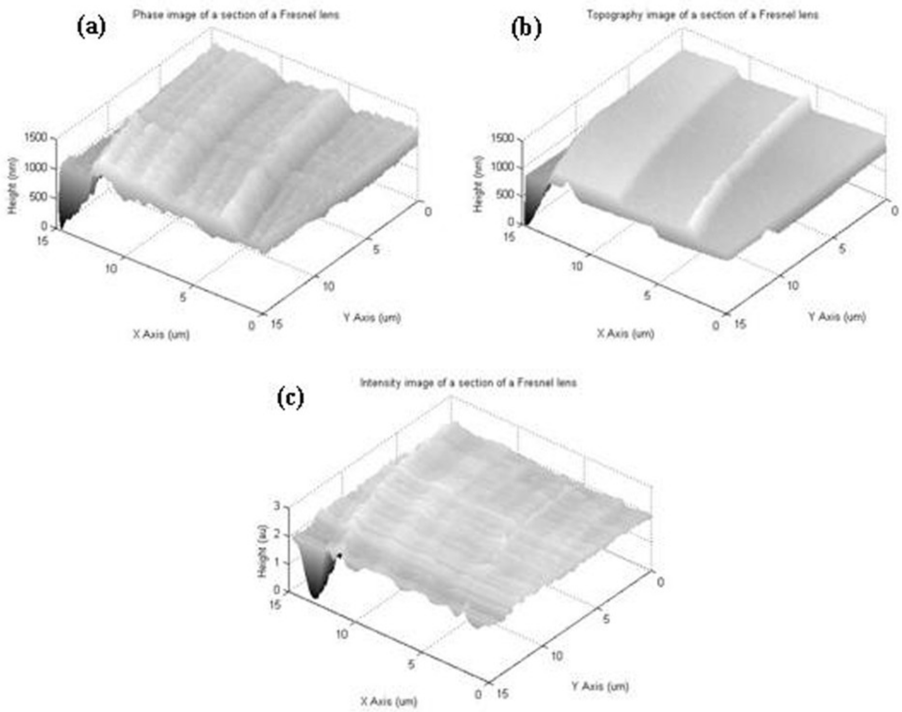
(a) Phase image of a section of a Fresnel lens

(b) Topography image of a section of a Fresnel lens

(c) Intensity image of a section of a Fresnel lens

Figure 6.1: Experimental results for the imaging of a small section of a Fresnel lens: a, Phase image of lens; b, Topography image of lens; c, Intensity image of the same lens. The features are only partially resolved in the intensity image but clearly identified in the phase image.

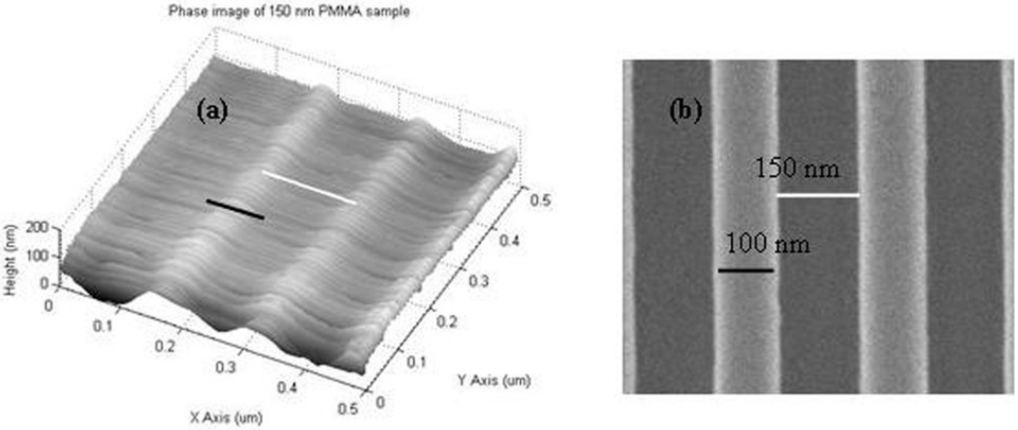
Phase image of 150 nm PMMA sample

Figure 6.2: Experimental results for the imaging of a 500 nm x 500 nm region of a PMMA sample with 100 nm thick lines separated by 150 nm. The image on the left (a), is a phase image and the region on the right (b), is an SEM image of the same region.

The main focus of my most recent research was to decouple the surface and subsurface contributions in the phase data and to extend the phase NSOM technique to liquid imaging. Biological cells for example are often nucleated and contain many other organelles unlike the red blood cells of mammals. Recently, several novel quantitative phase imaging techniques have been proposed and applied to the study of the surface morphology of biological specimens including red blood cells (RBCs) [22-25]. Erythrocytes are commonly used in quantitative phase investigations because depending on the species of origin, these simple cells are typically enucleated and can be considered to be homogenous. However, most biological cells are nucleated and contain several subsurface organelles. Thus the resulting phase data contains valuable subsurface information which up until now has been ignored.

In my investigation, intracellular information was extracted using simultaneously obtained sample phase and shear-force feedback topography data. After image registration, the topography data was used to suppress surface information in the phase data to revealed enhanced subsurface information. Unlike confocal and optical coherence microscopy, the generated subsurface data is integrated rather than consisting of individual slices. This new technique however is much better suited for imaging individual cells than the aforementioned techniques, which are more appropriate for imaging thicker samples. Much of this research was focused on imaging relatively simple cells with a single major intracellular component, such as nucleated red blood cells. The procedure was initially applied to the imaging of fabricated structures with surface and subsurface features. In each case, both the shape and height of the subsurface structures were extracted with excellent reproducibility.

6.2 Subsurface imaging: Fabricated Structures

Samples with surface features only, subsurface features only and both surface/subsurface features were fabricated as described in chapter 3. The samples with surface features consisted of 2 microns resist circles on 4 micron centers. In the case of the samples with subsurface features only, they were fabricated by planarizing trenches etched onto a quartz glass substrate. The subsurface/subsurface sample was fabricated by either deposited human red blood cells on top the planarized trench or depositing the 2 micron resist circle pattern onto the planarization layer. The results of imaging these samples are discussed in the next few sections.

6.2.1 Fabricated structure: Subsurface

The subsurface trenches ranged in size from 2 microns to 10 microns wide and from 200nm to about 1 micron in depth. In the case of the 200nm sample, approximately 1 micron of resist was required to achieve about 90% planarization. The 1 micron deep trench features required approximately 6-10 microns of resist to achieve 90% planarization. The width of the trenches did not significantly affect the planarization thickness layer. Figure 6.3 depicts the phase (a), topography (b) and intensity image (c) of a 5 micron wide, 180 nm deep trench prior to planarization. The overall shape and dimensions correspond quite well on both the phase and topography images. This is expected since there are no subsurface features present. It was often difficult to image the side walls of the etched samples due to significant loss in the optical signal at these regions. I attempted to minimize this problem by immersing the etched samples in diluted HF to reduce the gradient of the side walls with success. Several of these samples were planarized with resist for the subsurface imaging part of the investigation.

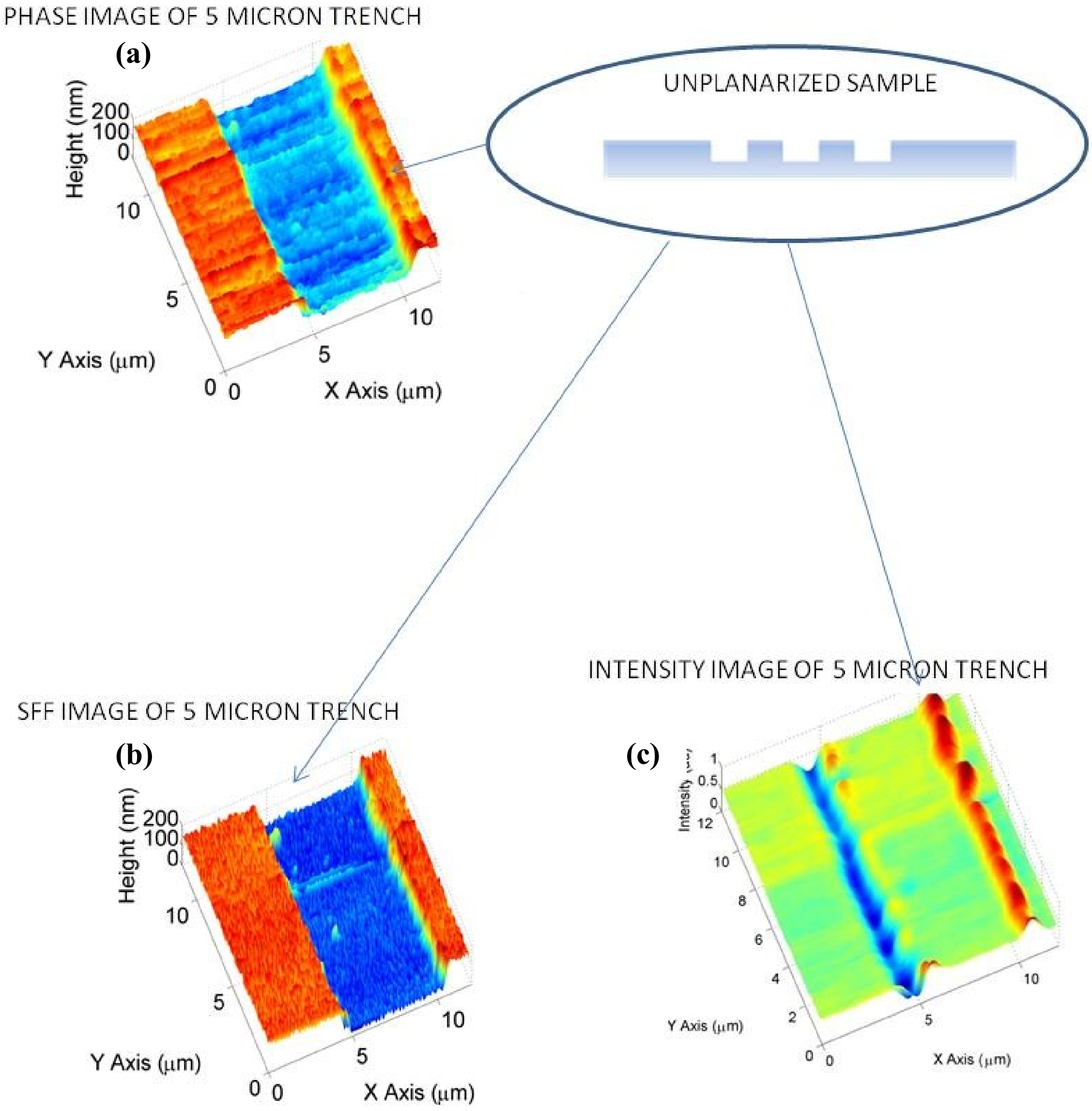

Figure 6.3: Experimental results for the imaging of a 15micron x 15 micron region of a 5 micron wide 180 nm deep RIE etched trench in a glass substrate. Images (a) and (b) are 3D representations of the phase and shear-force feedback topography data respectively of the same feature. Image (c) is an intensity image of the sample. A schematic of the sample is shown at the top right.

6.2.2 Subsurface features

The planarized samples were fabricated by overlaying a layer of resist over the etched RIE trench pattern. In figure 6.4, the phase and topography images of the planarized sample in figure 6.3 are shown. The subsurface feature is clearly resolved in the phase image but almost imperceptible in the shear-force feedback topography (SFF) result. Only the edges are discernible in the intensity image.

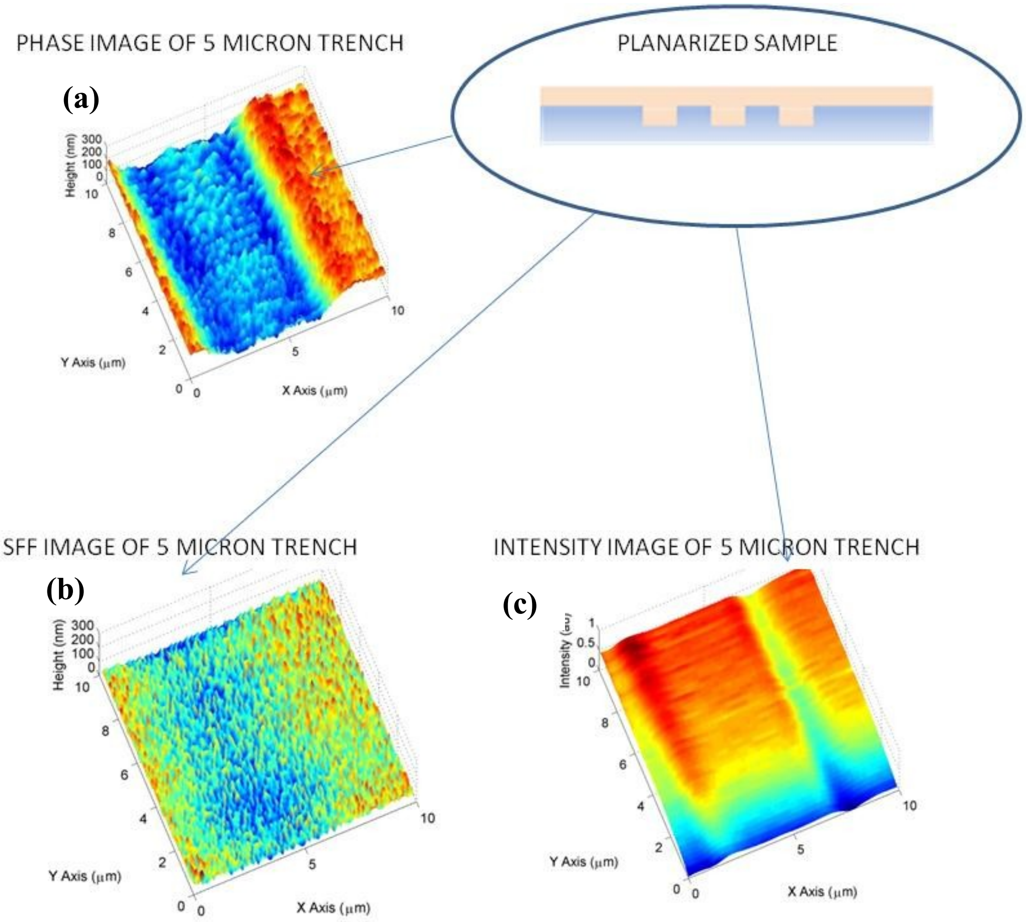

Figure 6.4: Experimental results for the imaging of a 15micron x 15 micron region of a 5 micron wide 180 nm deep planarized trench in a glass substrate. Images (a) and (b) are phase and shear-force feedback topography images of a region of the sample. Image (c) is an intensity image of the same region.

A comparison of line scans from the sample before planarization (red line trace in figure 6.5) and the extracted subsurface feature from the phase data (blue line trace in figure 6.5) indicate that the height and lateral dimensions of the extracted feature corresponds well with expected results.

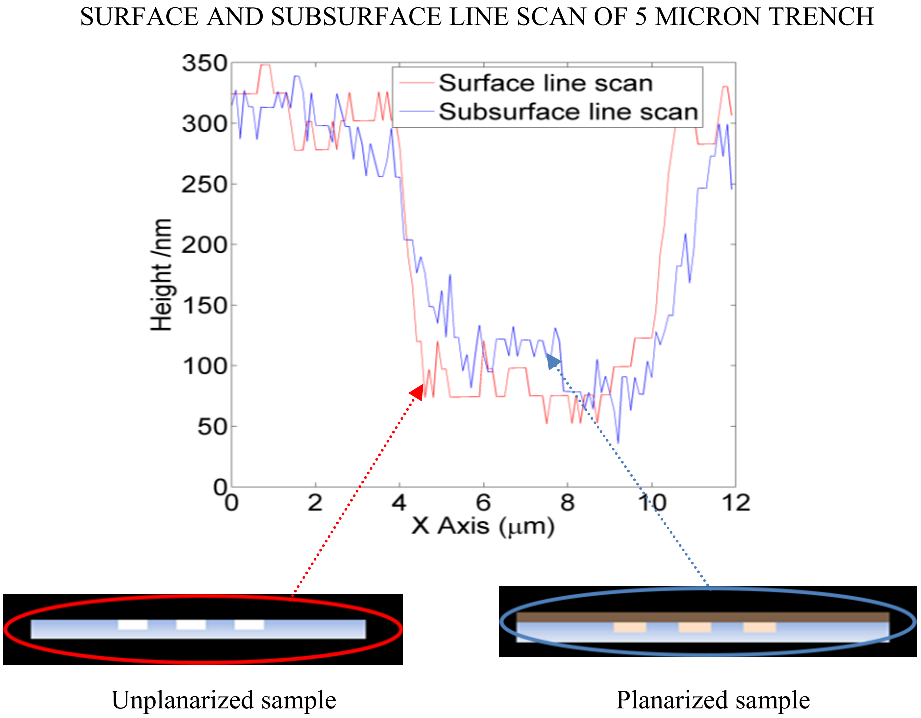
SURFACE AND SUBSURFACE LINE SCAN OF 5 MICRON TRENCH

Unplanarized sample

Planarized sample

Figure 6.5: The red trace is a line scan from the 180 nm deep 5 micron scan taken before planarization. The blue trace is a line scan from the phase data of the sample after planarized with a layer of resist. The profiles in air (before planarization) and after planarization were very consistent.

Figure 6.6 represents the results for a 800 nm deep, 5 micron wide planarized trench. The planarization thickness was about 6 microns in this instance because of the increased depth. The subsurface structure is well resolved in the phase data but is less than 100 nm in the SFF topography image. The height of the sample as determined from the subsurface phase results compared well with the measure height before planarization. However, for thick planarization layers, a “spreading effect” of the lateral feature dimensions is observed. In the line scans of 6.6 (c), the width of the planarized trench appears slightly larger than that of the unplanarized trench. This is due to the spreading of the beam emanating from the tip of the probe with sample separation. This effect is minimal for separation distances less than 6 microns and is characterized in further detail in the next section.

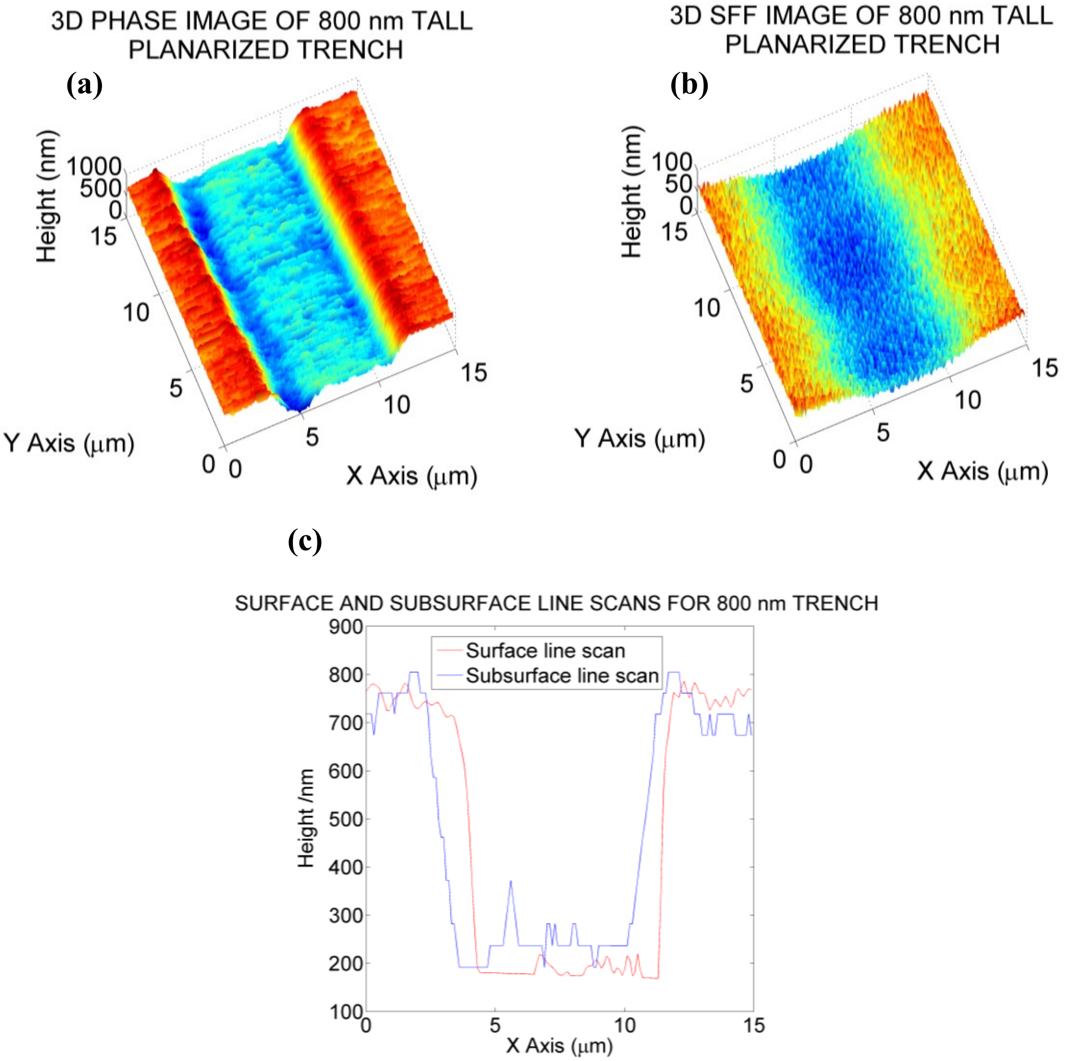

Figure 6.6: Experimental results for the imaging of a 5 micron wide 800 nm deep planarized trench. Images (a) and (b) are 3D representations of the phase and SFF topography data respectively. The planarized feature appears to be about 100nm but the subsurface feature is clearly resolved in the phase image. Image (c) indicates line scans from the phase data before planarization (red) and after planarization (blue).

6.23 Lateral feature spreading

As the probe to sample separation is increased, spreading of the emitted field results in a loss in resolution relative to imaging in the near-field. Figure 6.7 represents series of images obtained for a 5 micron wide, 800 nm unplanarized trench with a near-field probe sample separation (a), 2 microns separation (b), 4 microns separation (c) and 12 microns of separation (d). It is seen that the edges are progressively rounded and some of the details on the bottom surface of the trench is lost at larger separation distances. The overall shape and size is nevertheless conserved.

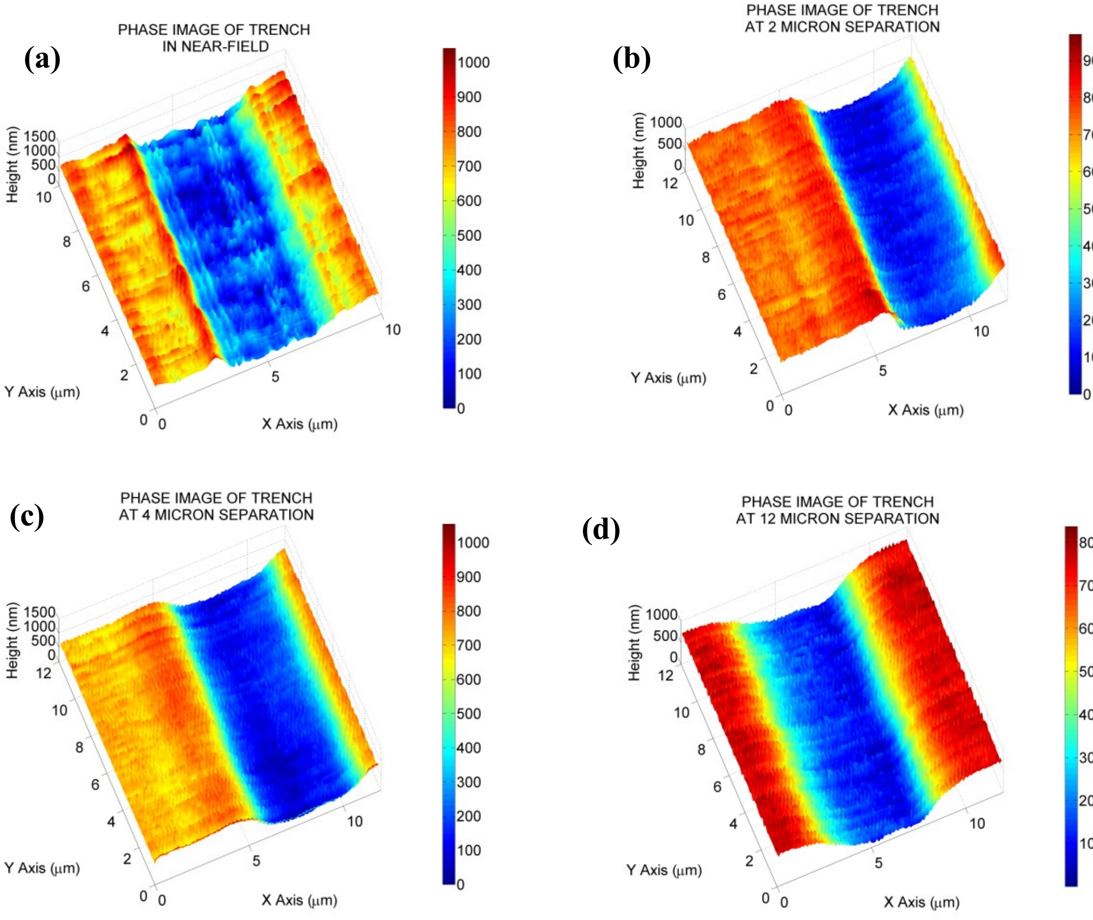

Figure 6.7: Series of phase images for different probe sample separation distances. Image (a) is an image of an 800nm deep, 5 microns wide unplanarized trench obtained with a near-field probe/sample separation. Images (b), (c) and (d) were obtained at 2, 4 and 12 microns separation respectively. It is observed that the edges are rounded of and some of the surface details are loss with increasing separation.

In biological cells, the subsurface organelle of interest often protrudes through the surface membrane but a substantial portion remains below the surface. In some instances, the feature of interest may be completely below the surface. The results of figure 6.7 suggest that it should possible to determine the shape and size of subsurface features several microns below the surface. The cells investigated in this research were typically less than two microns thick so it is expected that the "spreading effect" and the loss of resolution should be minimal. Figure 6.8 is a plot of FWHM (full width at half maximum) width of the trench feature versus separation distance for a 3.4 microns wide planarized trench. The blue plot illustrates how the FWHM value of the width of the trench increases with separation. This effect is minimal for separation distances less than about 4 microns but is notable for greater distances.

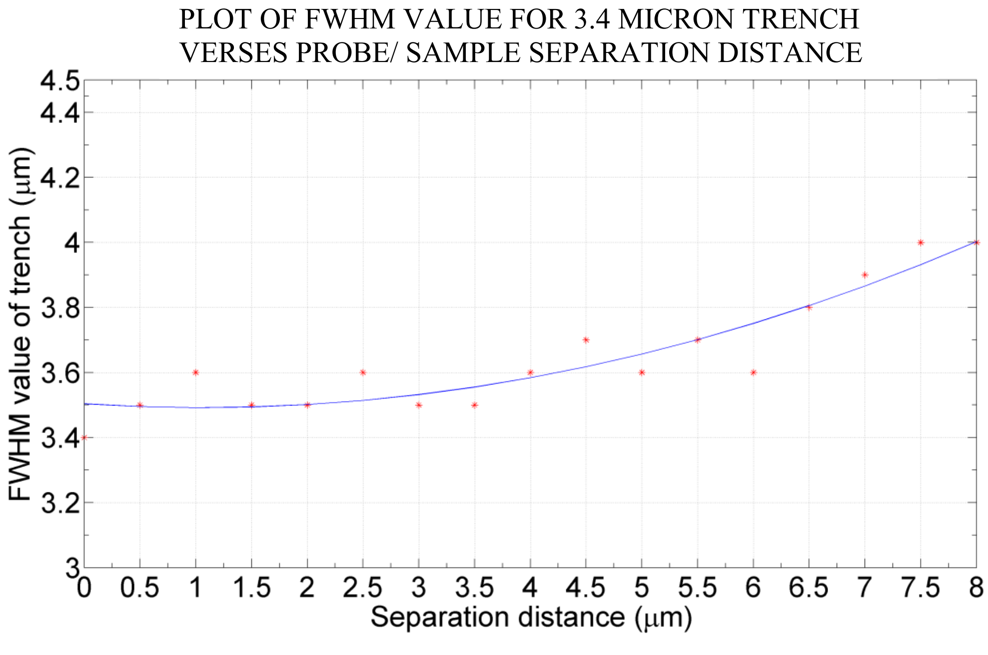

Figure 6.8: A plot of the FWHM value for a 3.5 micron trench verses probe/ sample separation distance is shown. The FWHW value for a separation of 0 microns corresponds to the near-field value. As the separation increases, the width of the lateral dimension of the subsurface feature also increases. This effect is minimal for separation distances of less than 4 microns. Most of the samples investigated as part of this research were less than 2 microns thick.

6.24 Fabricated structure: Surface/Subsurface

The surface/subsurface samples consisted of a planarized trench with either red blood cells or a 2 micron resist pattern deposited on top. Figure 6.9 depicts the SFF topography (a), phase (b) and intensity images (c) for a sample with a surface human red blood cell on top a subsurface 10 microns wide trench. The trench was about 500 nm deep with a 6 wide micron thick planarization layer. A schematic of the sample is shown in (d) with the subsurface result in (e). In the SFF images, only the surface RBC is observed whereas both the RBC and subsurface trench is observed in the phase data. This is confirmed from the line scans from the SFF and phase images. It is worth noting that the nature of the sample is unclear from an examination of the phase data only, without prior knowledge. That fact that a subsurface feature is present in the phase data is only apparent after an examination on the topography result. During the image processing stage, the topography data is converted to a phase equivalent data and both data sets are pre-processes before subtraction as explained in chapter5. The registration process is never perfect and a residue error results after subtraction. The result of the subtraction is shown in (e). The subsurface trench is clearly observed but the RBC has been effectively eliminated. After suppression of the residue error using the algorithm described in chapter 5, the error is substantially reduced but not completely eliminated.

Thus it seen that it is possible to effectively suppressed surface information in a sample with both surface and subsurface features to yield a final image with essentially only subsurface information. The sample investigated was quite simple in that there was a single dominant surface feature. Although this is often the case with biological cells, it was nevertheless decided that a more complex sample with multiple surface features would be investigated to test the robustness of the registration algorithm.

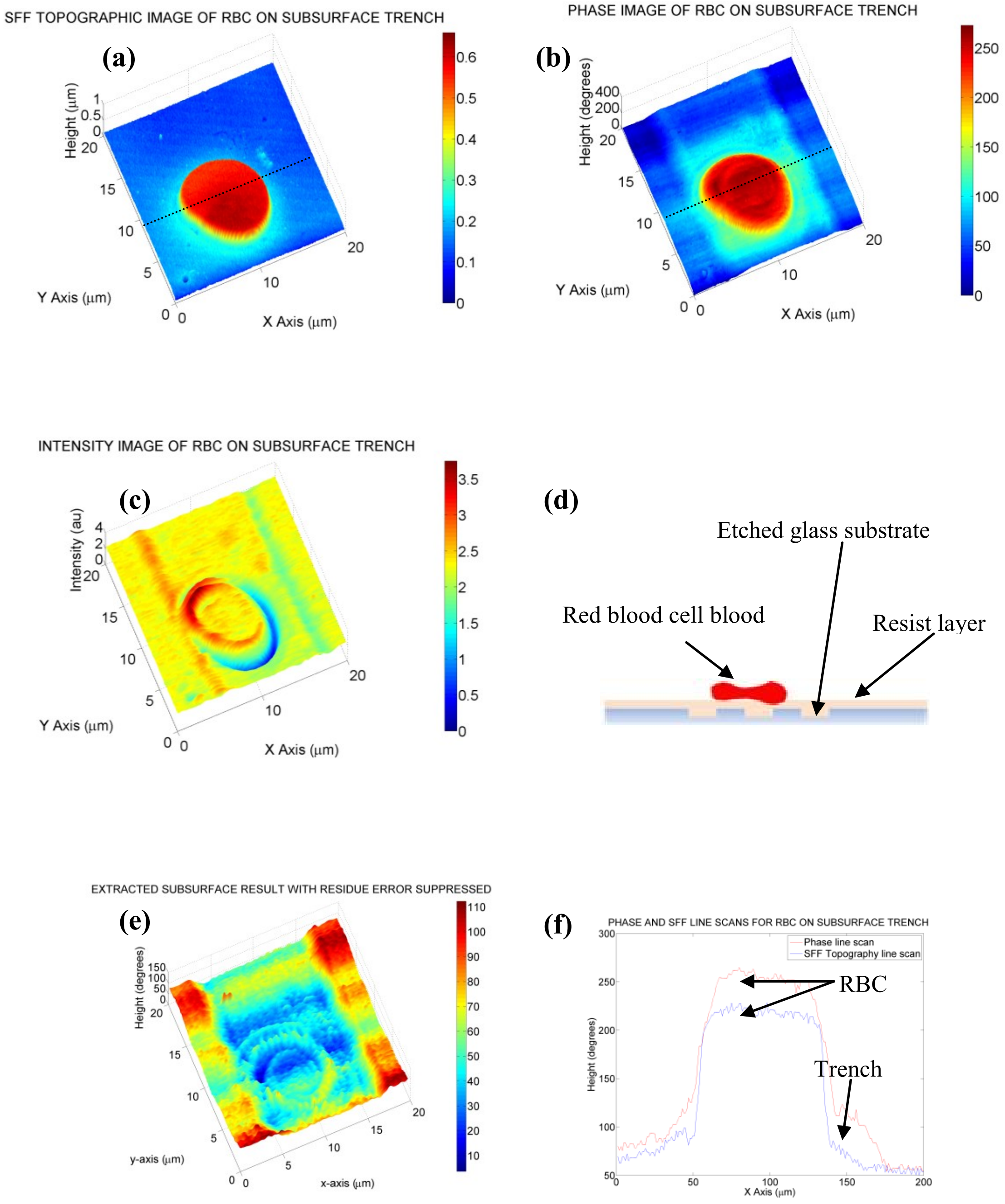

Figure 6.9: Figure (a) is a shear-force feedback (SFF) topography image of a human red blood cell deposited on a 10 microns wide subsurface trench. Images (b) and (c) are the corresponding phase and intensity images respectively. Image (d) is a schematic of the fabricated sample. Image (e) represents the extracted subsurface image and image (f) depicts line scans in the x direction of the SFF and the phase images in (a) and (c), indicated by black dotted lines.

Results for the circular resist pattern covered planarized trench are shown in figure 6.10. The SFF and phase images are indicated in (a) and (b) respectively and the subsurface results in (c).

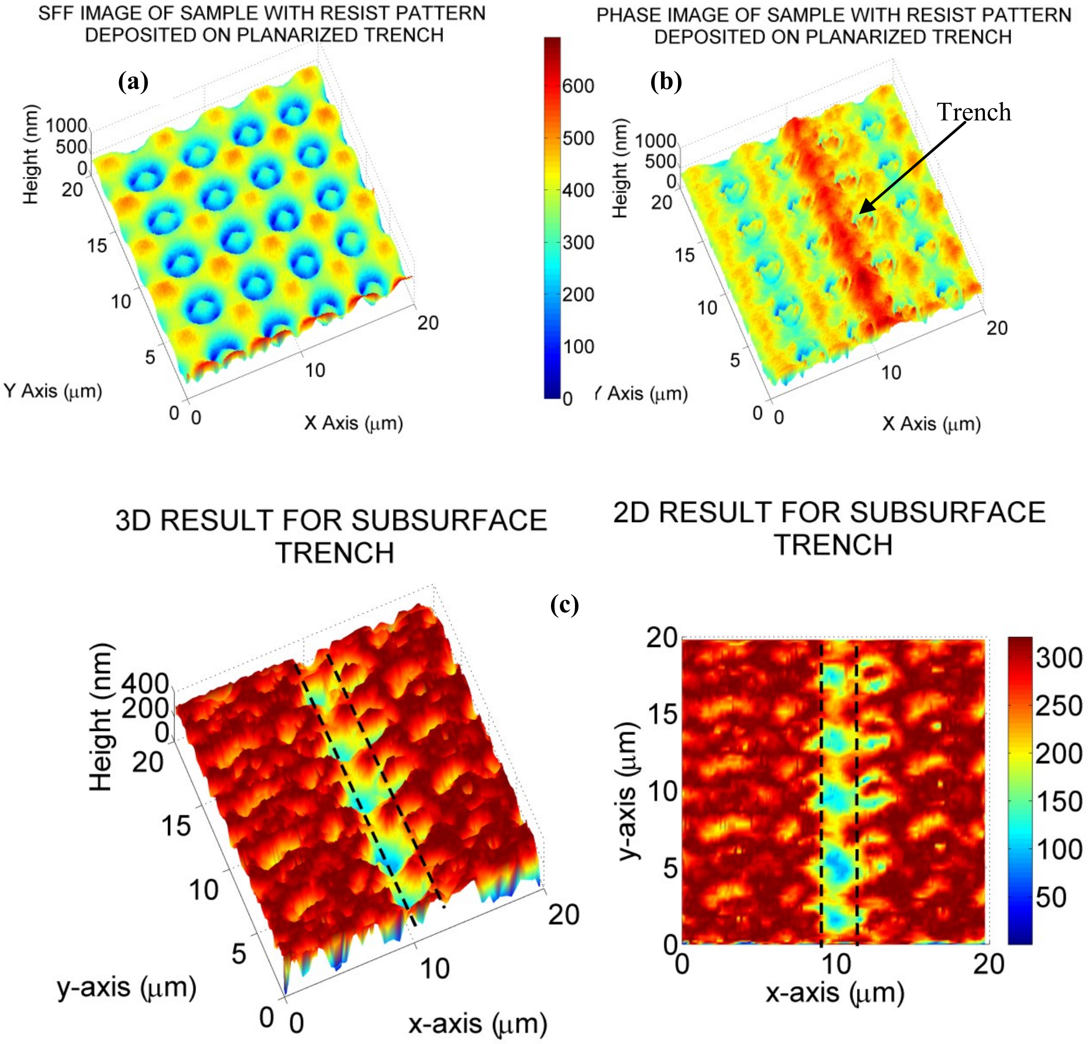

Figure 6.10: Experimental results for circular resist pattern covered planarized trench. Images (a) and (b) are the SFF and phase images respectively. 3D and 2D representation of the extracted subsurface trench are shown in image (c). The dotted black lines indicate the edges of the trench.

The width of the trench as measured before planarization was approximately 2 microns with a depth of about 200 nm. A negative resist was used for planarization because the optical opacity allowed for the visible detection of the subsurface trench prior to scanning.

Thus the 2 micron circular pattern is the negative of that usually obtained. This represents a difficult case as there are multiple periodic surface features in the phase result. The SFF result depicts only the resist pattern but the subsurface trench is also observed in the phase image. The dotted lines in (c) indicate the edges of the trench. It was very difficult to register the two images and as such the subtraction procedure resulted in less than ideal results. The subsurface feature is nevertheless readily identified.

6.3 Subsurface imaging: Biological samples

One of the primary objectives of this research was to image the subsurface intracellular components of biological cells. The most prominent and readily identifiable structure of a cell is the nucleus. This organelle is typically several microns in diameter depending on the cell in concern. As indicated previously, the shape and size of this organelle is often an indicator of the progression or onset of pathological conditions including cancer.

Malaria is characterized by the development of the plasmodium parasite inside red blood cells. Another stated objective of this research was to successfully image the plasmodium parasite while inside a red blood cell. There are very few non invasive techniques for the imaging of malaria infected RBCS and as such these results may prove very useful to researchers in the field of malaria research. The results of the biological specimen imaging is provided in the next few sections.

6.31 Human red blood cells

Most RBCS including those of mammals and birds are enucleated and are considered to homogenous [53]. Amphibians, fishes and reptiles in particular have nucleated RBCs. Human RBCs are enucleated homogenous with an average refractive index of 1.41. Thus a SFF scan of such a cell should appear identical to the corresponding phase result. The subsurface result should also not reveal any significant intracellular features as there are none. A sample was prepared by smearing a drop of blood onto a glass substrate as describe in chapter 3. Images (a), (b) and (c) indicates the SFF, intensity and phase results respectively. The line scans of the SFF and phase data shown in (d) indicate a very close match after registration. Images (e) and (f) represent the subsurface results before and after residue suppression. It is clear from (f) that there are no significant subsurface features.

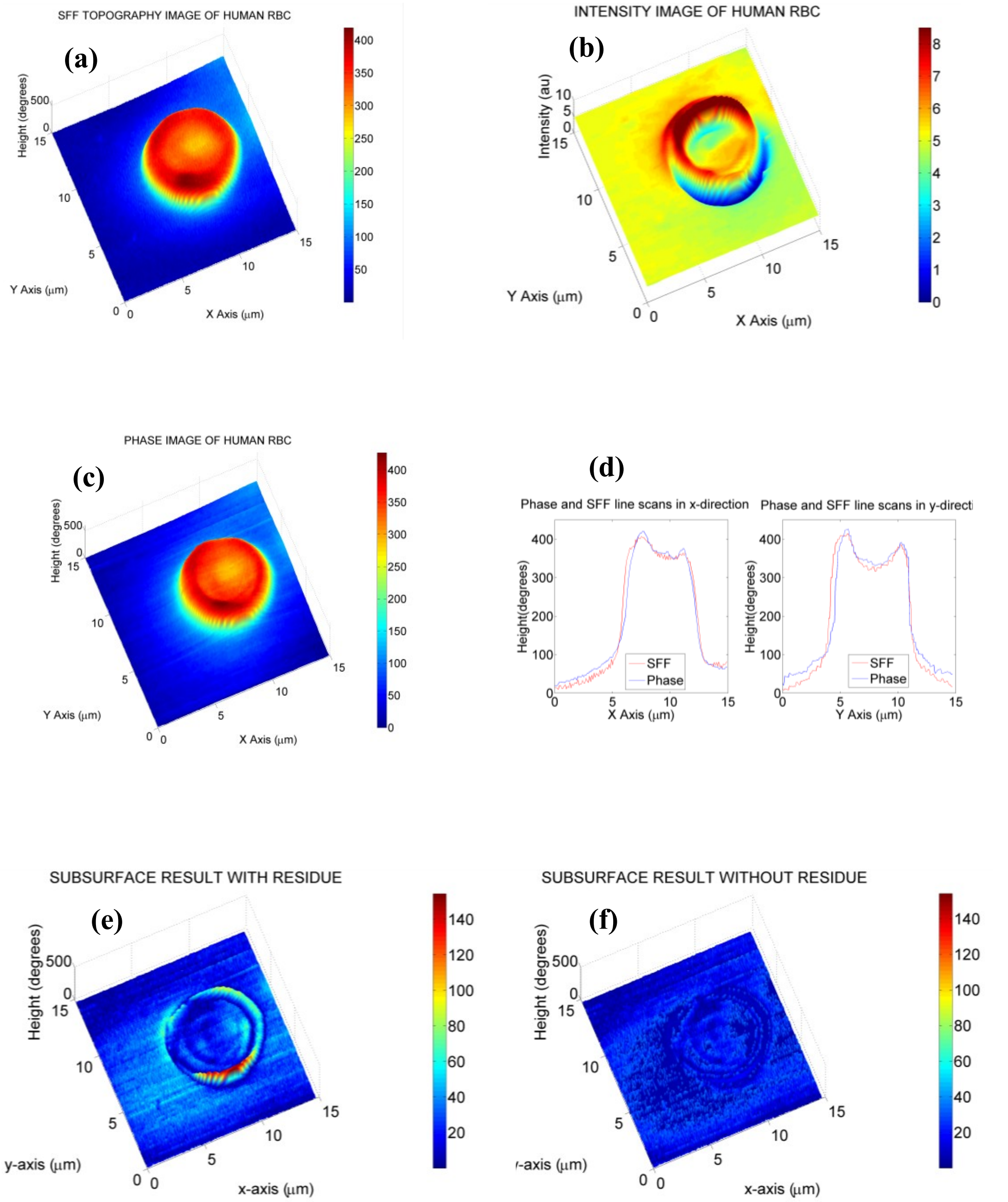

Figure 6.11: Experimental results for a human red blood cell. Images (a), (b) and (c) represents the SFF, intensity and phase of the red blood cell. Image (d) indicates line scans in the x and y directions for the SFF (red) and phase (blue) images. A very good match was obtained after registration. Images (e) and (f) are the subsurface results before and after residue noise suppression respectively.

6.32 Fish red blood cells

A fish's red blood cells present a very different situation to that of a human being. Erythrocytes from the silver dollar fish (Metynnis Argenteus) were examined as part of this investigation. The results are shown in figure 6.12.

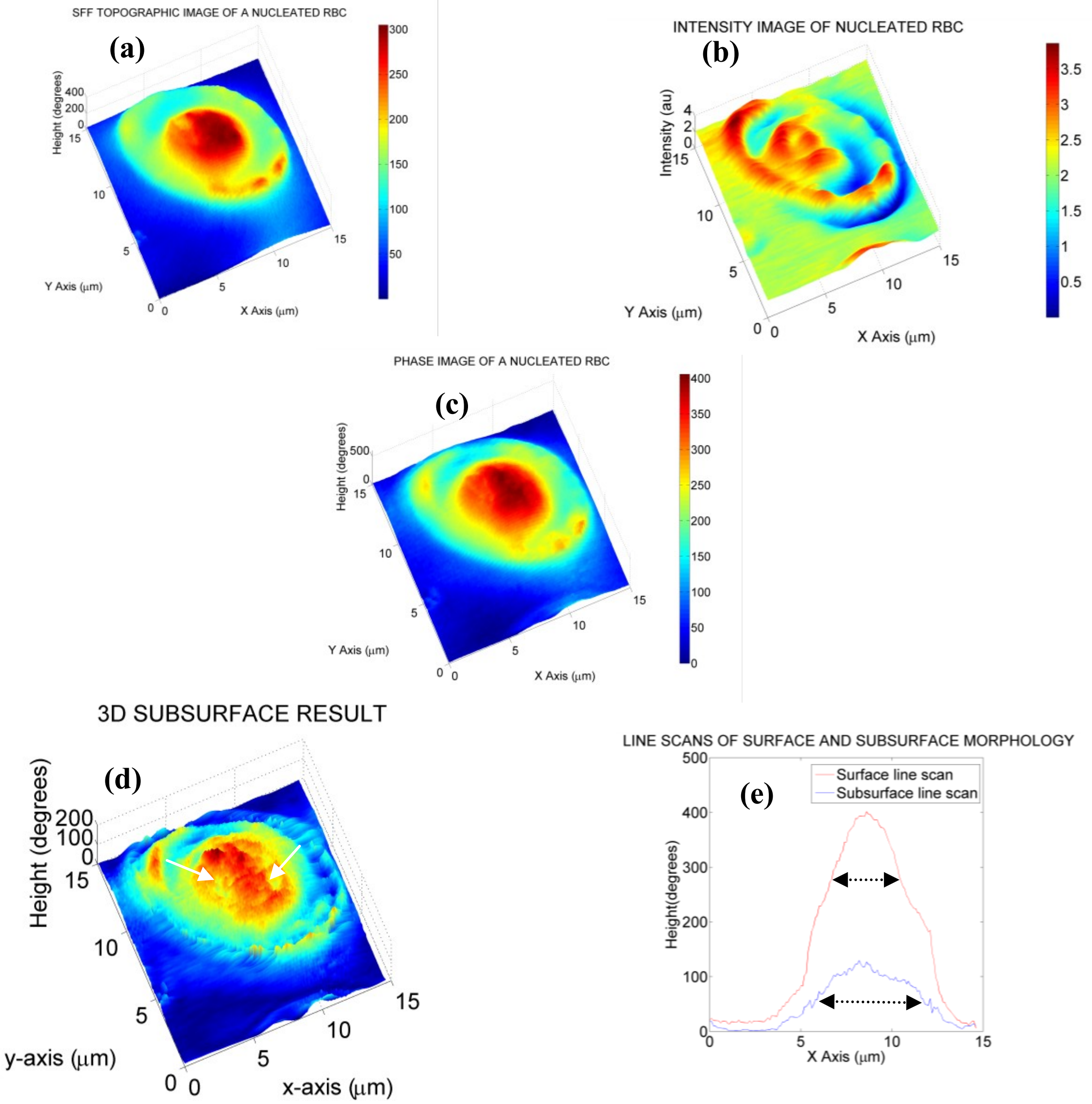

Figure 6.12: Images (a), (b) and (c) represent the SFF, intensity and phase images of a fish's red blood cell. Image (d) indicates the 3D representation of the extracted subsurface nucleus. The white arrows point to small pits on the surface of the nucleus. In image (e), the red line represents a line scan of the surface topography while the blue line represents a line scan of the extracted subsurface feature i.e. the nucleus.

Figures 6.12(a), (b) and (c) represent SFF, intensity and phase images of a fish's red blood cell. The nucleus protrudes through the surface and this is reflected as a bump at the center of the elliptical cell in both images. However, the highest point in the phase data corresponds to approximately 400 degrees whereas the highest point in the topography data (converted to degrees) corresponds to approximately 300 degrees. Thus it is apparent that there exists extra information in the phase which is not present in the topography data. The extracted subsurface nucleus is shown in 6.12 (d). The residue error has been substantially suppressed and the dominant features are clearly visible. The nucleus has an elliptical shape and a much rougher surface than that suggested by either the topography or phase data. The white arrows in image 6.12(d) identify tiny pits on the surface which is consistent with published descriptions [79].

Line scans of the surface and subsurface morphology are indicated by the red and blue plots respectively in 6.12 (e). It is clear from these plots that the spatial extent of the nucleus is greater than that indicated by the rounded bump in either the topography or phase image. This is easy to see from the dotted black lines in (e). If the refractive index of the nucleus is known, the volume can be easily calculated. Even if this information is unavailable, changes in the volume can be determined.

Figure 6.13 highlights some of the results for a collection of fish red blood cells. Image (a) represents the phase result while image (b) depicts 3D (left) and 2D (right) representations of the subsurface nuclei. This result indicates that the registration procedure is robust enough to provide excellent registration even if there are multiple features of interest in the phase and SFF topography images. It should be mentioned that the residue suppression algorithm works best when the feature in concern is away from any edges in the sample. If this is not the case, it is usually very difficult to differentiate between the residue noise and the subsurface feature. Fortunately, with most of the biological cells encountered, the dominant intracellular features were present near the center of the cell and away from the cell boundary.

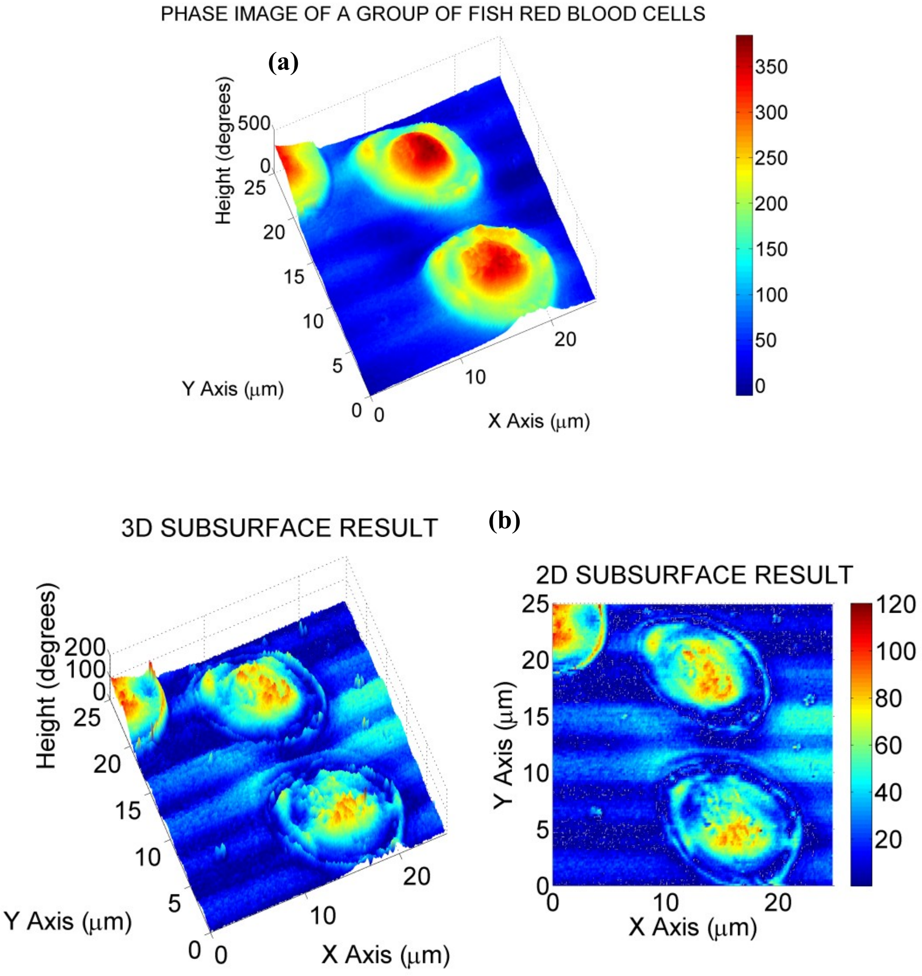

Figure 6.13: Experimental results for the imaging multiple fish red blood cells. Image (a) is a phase image of the cell collection. Image (b) indicates 3D (left) and 2D (right) representations of the subsurface results for the group of cells. The three nuclei are clearly observed.

6.33 Malaria infected cells

Malaria is caused by any one of several parasites which invade and eventually destroy red blood cells (RBCs). The Plasmodium Falciparum parasite in particular is one of the most insidious and virulent microscopic pathogen responsible for this disease. In spite of the global effort targeted at managing malaria, this disease results in millions of annual deaths worldwide [70]. Upon invasion of human erythrocytes, these pathogens cause significant changes to the cell's surface morphology [80, 81]. The parasite develops in distinct stages, consuming the red blood cells' hemoglobin and converting it to an insoluble form known as hemozoin [51]. In the later stages of development, large empty regions or vacuoles appear near the parasite where the hemoglobin has been totally consumed. Although a significant amount of research has been pursued towards understanding the mechanism by which these intracellular parasites evades detection of the body's immune system, much remains unknown.

Optical microscopy and florescent microscopy are the two most common techniques for investigating these cells [82, 83]. However, in the former, an exogenous contrast agent such as Giemsa stain is used and in the later, a fluorescence tag is required. With Geimsa staining, the quality of the diagnosis is strongly dependent on the skill and experience of the researcher [84] and neither approach can be considered to be non-invasive. X-ray imaging has been used for malaria studies but the technique can cause severe damage to the RBCs [85]. Atomic force microscopy studies of malaria infected red blood cells yields high spatial resolution but only surface morphology investigations are possible. Higher resolution surface morphology studies are possible with the SEM but this requires deleterious and invasive preparation techniques and does not allow for subsurface investigation. Confocal microscopy has proven to be a very powerful technique for malaria studies but the process is computationally intensive when attempting to reconstruct 3D images of the parasite.

There are three discrete stages in the development of the Plasmodium Falciparum parasite referred to as the ring, trophozoite and schizoint stages, each with well defined characteristics which will be highlighted in the respective results. In the ring stage, a ring-shaped vacuole is located near the parasite. By the time the cell progresses to the trophozoite stage of development, the size of the vacuole has increased significantly due to consumption of hemoglobin near the parasite. In the schizoint stage, the parasite has self replicated several times and occupies a large percentage of the volume of the cell.

Series A of figure 6.14 depict the results for the ring stage. Images (a) through (e) depict the optical, phase, topography, intensity and subsurface result in each series. In image (e) of the ring stage, it is seen that the parasite is relatively small compared to the cell and very little of the hemoglobin has been consumed. At this stage, the cell's surface morphology is not drastically altered although it is possible to determine the presence of the parasite in either the phase or topography image.

Series B is indicative of the trophozoite stage. A large circular region is observed where most of the hemoglobin has been consumed by the parasite in image (e). The cell is clearly deformed with a large bump on one side indicating the presence of the parasite. The shape of the parasite at this stage agrees quite well with that of previously published results using other imaging techniques [51, 86].

A: RING STAGE **B: TROPHOZOITE STAGE**

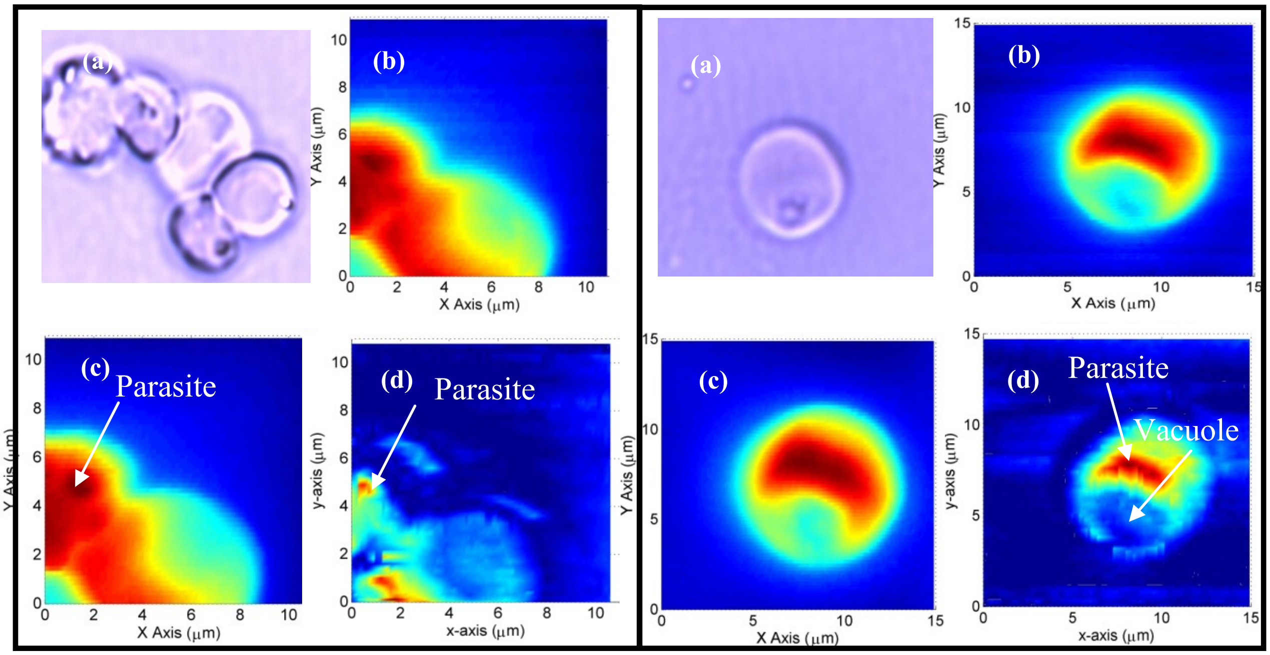

C: SCHIZOINT STAGE

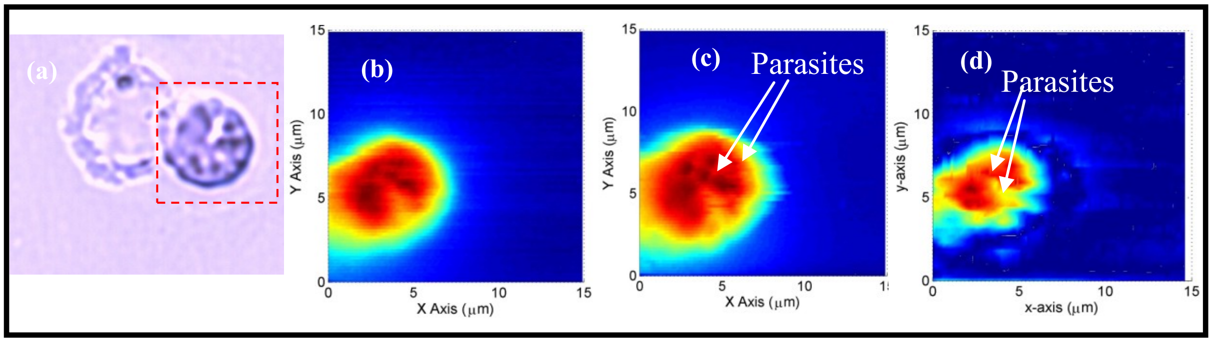

Figure 6.14: Results for imaging of the different developmental stages of the malaria parasite. Series A represents the first stage or ring stage of development. Series B represent the trophozoite stage of development and series C represent the final or schizoint stage. For each series, the images (a) through (d) represent the optical, phase, topography and subsurface images for the respective developmental stage of the parasite. In the ring stage, the parasite is tiny and the surface morphology of the cell is barely affected. In the next two stages, significant alterations to the surface morphology are observed.

The final series includes images of an infected cell in the schizoint stage. In this instance, the surface morphology departs significantly from that of a normal red blood cell. Several bumps are observed on the surface which corresponds to the individual parasite. The subsurface image indicates that the parasites occupies most of the volume of the cell and are clustered together. These results are in close agreement with the most recently published literature on the developmental stages of the Plasmodium Falciparum parasite [51, 82, 83]. In each stage, the parasite is readily identified and its spatial extent easily determined. Unlike most other techniques, this was achieved without any invasive preparation.

6.34 White blood cells

White blood cells or leukocytes play a vital role in helping the body fight infections. These cells appear translucent to the naked eye and are very difficult to observe without the use of a contrast agent or dye. The white blood cells investigated as part of this research were identified optically by painstakingly sifting through the red blood cells on a quartz substrate. They are easily differentiated from red blood cells due to their translucence appearance and their size. The imaging results for two different leukocytes are presented in figures 6.15 and 6.16. The first cell shown in figure 6.16 was identified as a neutrophil due to its size (approximately 10 microns in diameter) and overall granulated morphology. The SFF topography (a) and phase images (b) indicate a granulated morphology which is consistent with expected results. Nuetrophils are the most abundant white blood cells and are characterized by a “U” shaped nucleus as shown in image (c).

This cell depicted in figure 6.16 is smooth and agranular and as such can only be either a monocyte or a lymphocyte. However lymphocytes are only slightly larger than red blood cells and have a nucleus to cell ratio of almost 1:1. It is therefore clear that the white blood cell in question is a monocyte. The nucleus of the cell is clearly identifiable in both the topography and phase scans of 6.16 (a) and (b) respectively. Although the two images appear similar, the maximum height in degrees of the phase data is greater than that of the shear-force feedback topography information expressed as a phase value. Thus it is clear that at least part of the nucleus is subsurface. Also, more detailed structures are observed in the phase image when compared to the topography which suggests that there is additional information in this data.

Image 6.16 (c) indicates that the nucleus of the cell is smooth and large. A careful observation reveals that the nucleus has a bean-shaped appearance as is typical for these cells. This imaging procedure is useful in that it allows for the identification of white blood cells without the need for any exogenous dyes.

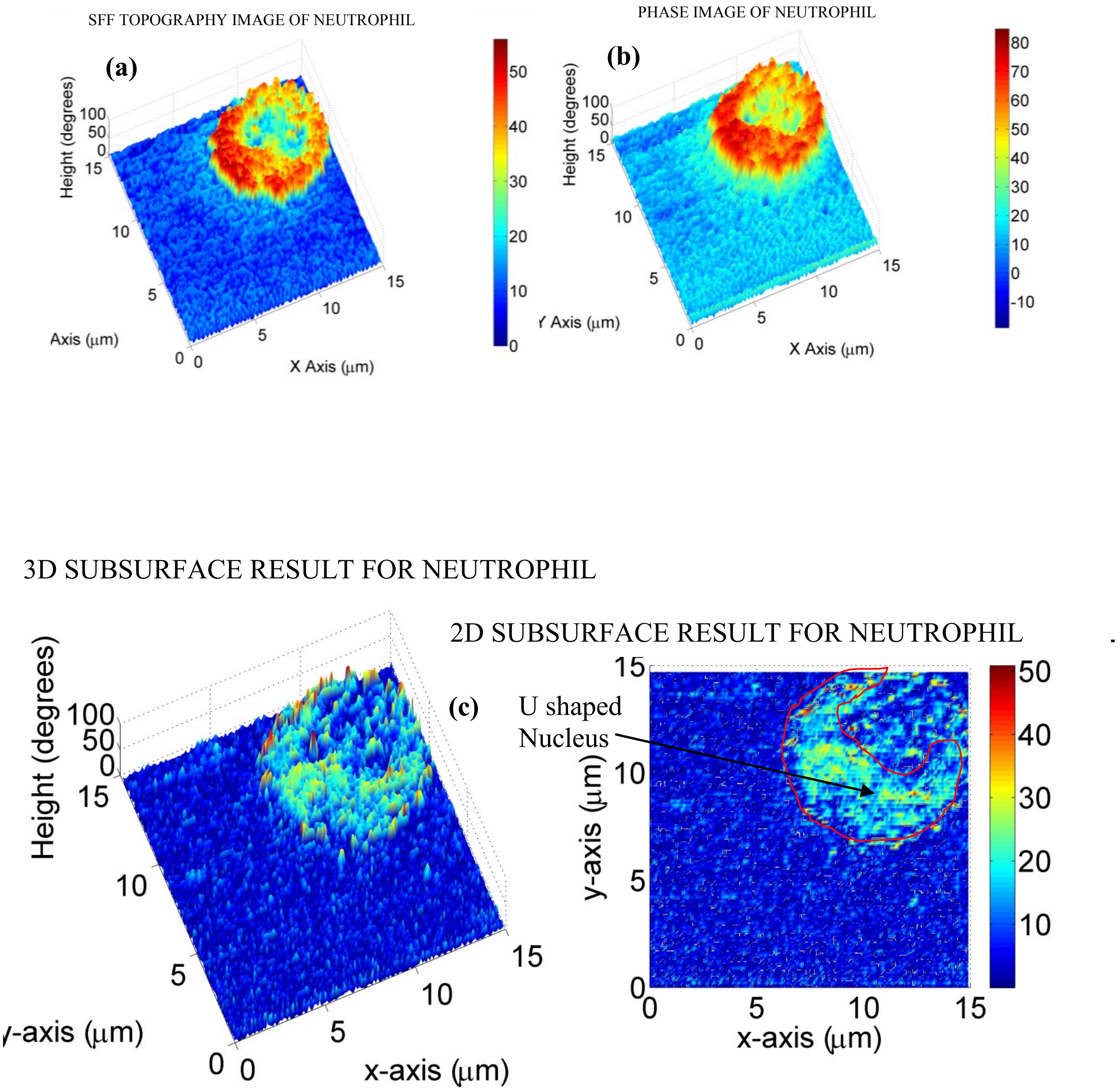

Figure 6.15: Experimental results for a human neutrophil. Images (a) and (b) represent the topography and phase images of the nuetrophil respectively. The images in (c) are 3D (left) and 2D (right) representation of the subsurface information. This image depicts the nucleus which has a typical “U” shape.

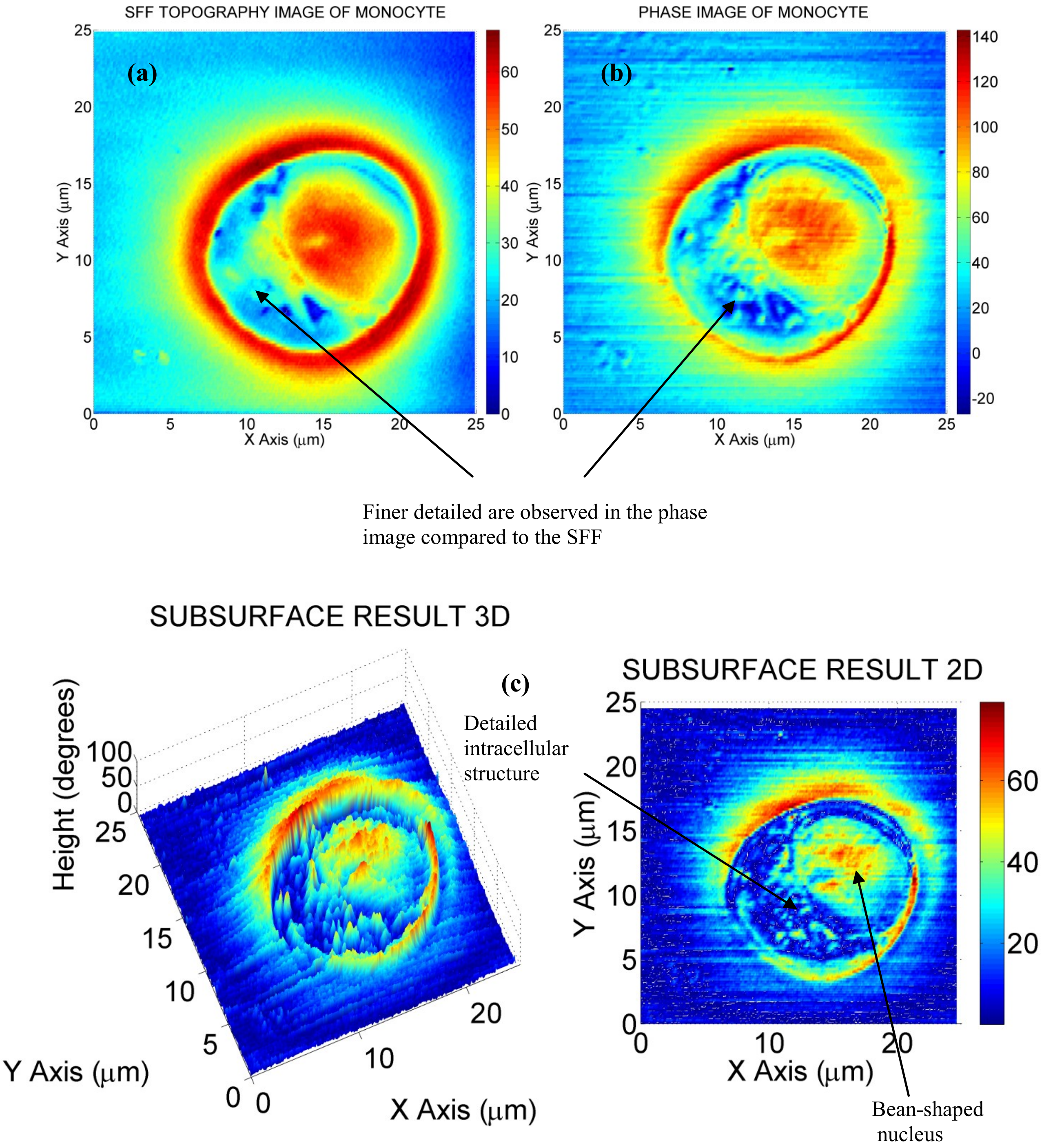

Finer detailed are observed in the phase image compared to the SFF

Detailed intracellular structure

Bean-shaped nucleus

Figure 6.16: Experimental results for a human monocyte. Images (a) and (b) represent the topography and phase images of the monocyte respectively. The images in (c) are 3D (left) and 2D (right) representation of the extracted subsurface information. These images present a more detailed view of the nucleus that either the phase or SFF image.

6.4 Conclusion

The hybrid SFF/ scanning phase system has been shown to be effective in imaging subsurface features in both fabricated structures and biological cells. In the former, the extracted surface results after planarization of RIE etched trenches showed strong agreement in shape and dimensions when compared with the results of the pre-planarizations scans. A spreading effect is observed for thicker samples but this effect is minimal for samples less than 4 microns thick. It was also shown that surface and subsurface information in the phase data could be reliably decoupled. The decoupling procedure proved to be quite useful with regards to biological specimen, allowing for the study of intracellular structures. In the case of a nucleated red blood cell, it was possible to determine the shape and "true" spatial extent of the nucleus. Given the refractive index of the nucleus, it is possible to determine the volume. Even if the refractive index is unknown, it is still possible to determine the change in volume with time. This has direct application to oncology studies.

This technique also allowed for the in-vivo investigation of the malaria parasite while inside the host red blood cell. This was achieved without staining or slicing of the specimen and using information obtained in a single scan. The subsurface information is always integrated data along the optical path of the transmitted beam through the sample but for simple, relatively thin (less the 4 microns) cells, it is clear that the results show very strong potential for intracellular studies. This approach is ideal for samples with isolated subsurface features which are away from the cell boundary.

All the results were obtained for dry samples using standard but non invasive preparation techniques such as fixing. Such was the case with the white blood cells. While red blood cells are able to maintain their shape very well due to their exoskeleton, the same is not necessarily true for other cells. However, the shape of the nucleus is typically not affected as significantly due to drying. Nevertheless, investigation to the surface morphology biological cells is best pursued in an environment similar to the native environment of the cell. For most living cells, this is an aqueous environment. In the next chapter, I will present the details and results of modification made to my system to allow for imaging in a liquid.

CHAPTER 7: IMAGING IN A LIQUID

7.1 Introduction

Biological cells in living organisms are typically surrounded by an aqueous medium which plays a critical role in nutrient uptake and waste material exchange. This medium also helps to maintain a viable pH environment for the cell. Thus the investigation of live specimens is only possible in an aqueous solution which is similar to their native interstitial medium. This is considered the “Holy Grail” in biological imaging since dynamic physiological processes can only occur in a live cell. An understanding of these fundamental processes is critical to our understanding of the onset and progress of pathological diseases such as cancer. An aqueous environment also allows chemical agents to be administered to a cell and the effects observed in real-time.

As described previously, the damping effect of a liquid on the NSOM tip and changes in the liquid level can adversely affect shear-force feedback system. A liquid cell with a replenishment system to compensate for evaporation was designed to circumvent this problem. As part of this investigation, both fabricated resist structures and rat fibroblast cells were imaged. The resist sample was imaged in distilled water and the fibroblast cells in phosphate buffer solution. In each instance, the results of the scans in a liquid environment compared very well to the scans in air. In the final part of my investigation, cell refractometry studies were performed on the rat cells. The refractive index information obtained for these cells in air and water correspond quite well with previously published results. In a recent publication, a direct relationship was established between the refractive index of certain biological cells and the onset of certain cancer [16]. As with this technique, there are several other quantitative phase procedures which allow for cell refractometry analysis [13-14], but they either lack the spatial specificity affording by a scanning probe system or are technically challenging to implement. The results of my investigation into imaging in a liquid environment are included in this chapter.

7.2 Shear-force feedback in a liquid

There are three major potential problems when imaging in a liquid; the first involves overcoming the surface tension of the liquid, the second involves the reduced Q-factor due to damping and the third is related to liquid evaporation. I have proposed some novel solutions to these problems which will be highlighted in this chapter.

7.21 Surface tension of aqueous solution

During the imaging process, one of my primary objectives was to maintain a thin film of liquid over the sample. This was facilitated in part by the use of an o-ring to form a negative meniscus over the sample. However if distilled water is used, the surface tension causes “beading” instead of a thin film. It was therefore useful to add a surfactant such as an alcohol (isopropanol was used in this investigation) to help reduce the surface tension. However, due diligence is required as the evaporation rate is higher for the mixture. When imaging the resist sample in a liquid one part of isopropanol was used for every four parts of distilled water. This allowed a thin film to be formed over the sample with a manageable evaporation rate.

7.22 Reduction in Q-factor

When the dithered probe attached to the quartz tuning fork is slowly dipped into a liquid, the system experiences a significant damping effect which is proportional to the insertion length [87]. In air, the tuning fork has a resonant frequency of 32.76 kHz with a Q-factor as high as 7,000. Once the probe is attached, the resonant frequency typically increases to between 33 and 34 kHz although it is possible to have a slight decrease. The combined effect of changes in the mass and stiffness of the system influences the outcome since an increased mass lowers the resonant frequency while an increase in stiffness has the opposite effect. A corresponding decrease is observed in the Q-factor with the probe attached. Typically values are in the range of 200 to 1000. In my experiments, a Q-factor of about 400 with the probe attached was usual for a free oscillator. Q-factors of 1000 or more often resulted in an unstable system probably due to the time constant setting used on the lock-in amplifier and PI circuit. In practice, an ideal Q-factor was in the range of 200 to 400. Upon immersion in a liquid, it was observed that there was always a decrease in the resonance frequency and Q factor. If the behavior of the system is described using a harmonic oscillator model, it is seen that the Q-factor is inversely proportional to the viscosity of the medium as observed. Modeling the behavior of the system in a liquid as a forced oscillator, we have

$$\omega_{\max} = \omega_o \sqrt{1 - \frac{1}{2Q^2}} \tag{23}$$

where the resonant frequency in a liquid is given by ω_{max} and the resonant frequency of the free oscillator is given by ω_o. It is seen that as Q decreases, so does the resonant frequency. Also, for a slight decrease in Q, there should be a correspondingly small change in the resonant frequency in a liquid. Figure 7.1 shows frequency response plots for a mechanically driven tuning fork when the probe is dithered in air (blue plot), and for slight (black plot) and deep immersion (red plot) in a liquid. The colored arrows indicate the maximum amplitude for the corresponding curve e.g. the blue arrow indicates the maximum amplitude for the blue plot. In this investigation and subsequent liquid imaging, the prongs of the fork were not allowed to come into contact with the liquid since this results in electrical "shorting". The behavior of the tuning fork is consistent with that of a forced harmonic oscillator. The amplitude of the response signal decreased by about 6.6 % with "slight immersion" and by approximately 14.2 % with "deeper immersion". Immersion was achieved by applying an electronic signal to the z-axis of the precision stage to move the liquid cell towards the fixed dithered probe. It was therefore possible to determine that the immersion depth for "slight immersion" was about 10 microns and about 50 microns for "deeper immersion".

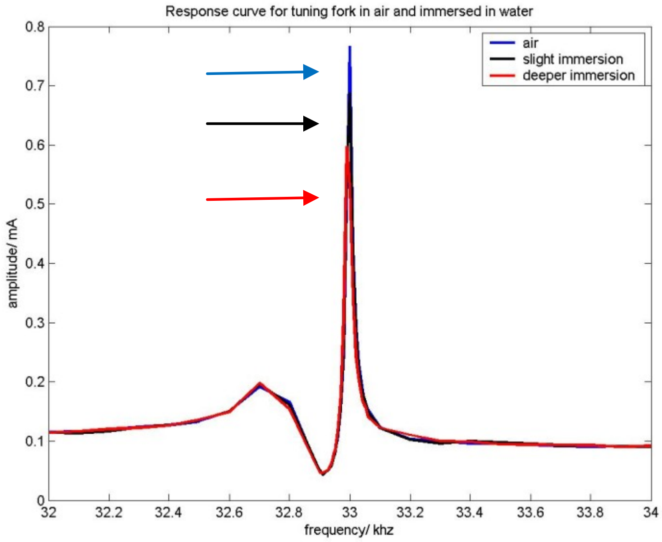

Figure 7.1: The plots shown depicts the frequency response of a tuning in air (blue), after slight immersion in water (black) and after approximately 50 microns of immersion (red). Alcohol was added to the distilled water to reduce the surface tension. The arrows indicate the maximum amplitude for the response curve of the corresponding color i.e. the blue arrow corresponds to the maximum of the blue curve etc.

A Q-factor of approximately 800 was obtained for the tuning fork in air. There was only a slight reduction in this value with an immersion depth of up to 50 microns and a slight downshift in the resonant frequency. Taking all these facts into consideration, it was determined that fiber probe should be only slightly immersed in the imaging liquid. This requires a thin liquid film and evaporation compensation.

7.23 Effects due to evaporation

Using a thin film of liquid over the sample requires evaporation compensation. The details of the theory and the experimental setup are described in chapters 2 and 4 respectively. Figure 7.2 represents line scans of 2 micron circles on 4 micron centers, imaged in distilled water without evaporation compensation. A selected region of the sample was scanned repeated back and forth in the x direction over a period of about 24 minutes. As the liquid evaporated throughout the progression of the scan, it is seen that noise artifacts start to appear in the line scans. In addition, the height of the feature starts to gradually decrease after about 6 minutes. This effect occurs primarily due to a loss of sensitivity of the feedback system as the scan progresses.

Prior to each scan, the phase difference between the driving signal of the dithering PZT and the signal generated by the tuning fork is set at some fixed value (usually minus 20 degrees). As the probe starts to engage the sample while approaching the near-field, this phase value rapidly increased as a result of the increased damping which results from the sample interaction. It was determined experimentally that an increase in phase from minus 20 to 0 degrees results in a stable point for near-field scanning. For liquid imaging, this phase difference is set while the probe is in the liquid. As the liquid evaporates, this phase difference increases. Thus the engagement point of the sample with the probe is further away as more liquid evaporates. This leads to a lower resolution and the introduction of noise artifacts as the scan progresses. This effect was effectively eliminated by compensating for evaporation.

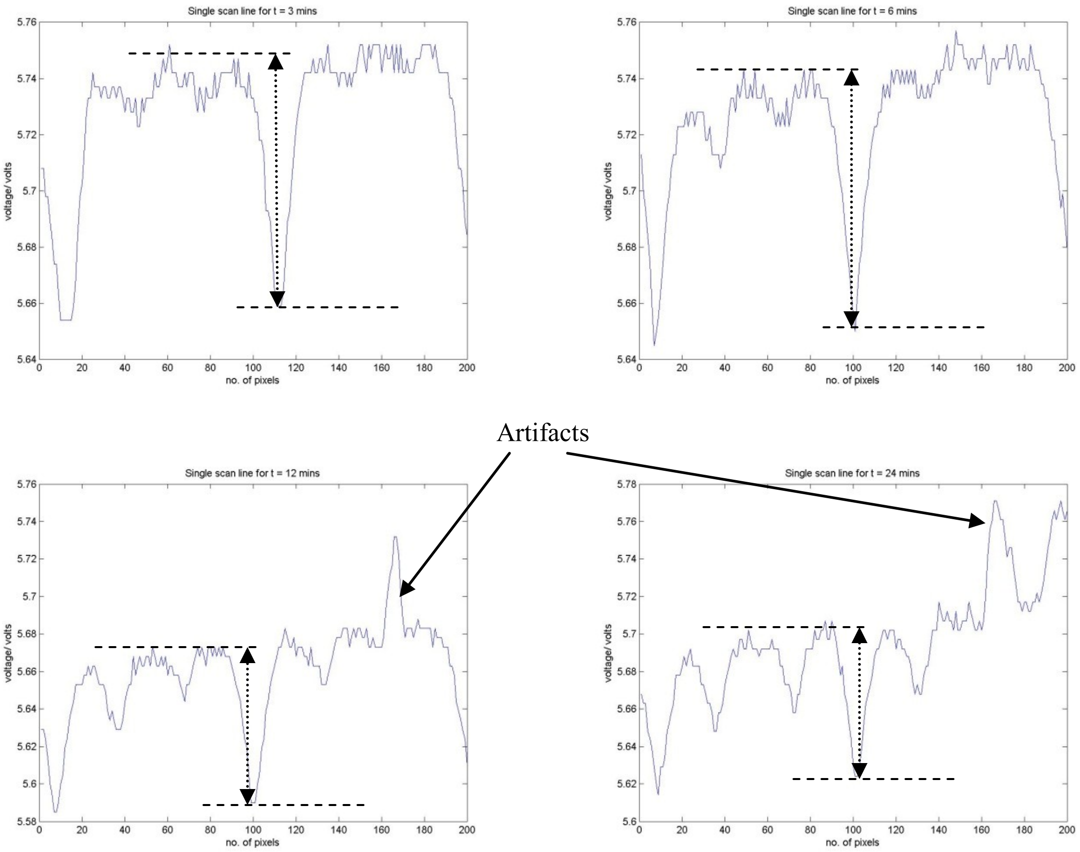

Figure 7.2: Reproducibility line traces in the x-direction for a 2 micron photoresist sample in a liquid without evaporation compensation after (a) 3 minutes, (b) 6 minutes, (c) 12 minutes and (d) 24 minutes of scanning. It is observed that the measured height decreases throughout the scan duration. Between 6 and 12 minutes, the first artifacts start to appear. This effect is due to a loss in sensitivity of the feedback system.

7.3 Imaging in a liquid: Resist and Fibroblast Samples

In this part of the investigation, rat fibroblast cells were imaged in phosphate buffered saline. This aqueous solution is ideal for imaging biological specimens because it helps to maintain a constant pH. The solution is isotonic in that the osmolarity and ion concentration usually matches that of the cell. If the ion concentration of the medium is too high, water tends to leak out of the cell and shrinkage occurs. If the ion concentration is too low, water enters the cell and can cause it to burst. PBS has the added advantage of being non toxic to biological cells. Prior to biological imaging, the liquid imaging system was testing by imaging a resist sample in both air and water. The results for the resist and fibroblast samples are included in the next two sections.

7.31 Resist sample

The resist sample was fabricated as described in chapter 3. Several scans of the sample were performed first in air, then in a solution of distilled water with isopropanol added. The scans in both air and in the liquid were highly reproducible. The test resist sample had a slightly irregular shape as seen in figure 7.3. The top of the sample did not have the characteristic dip in the center which characterized previous samples. It should also be noted that the regions scanned in the air and water are not exactly the same. The reason for this is subsequent to scanning the sample in air, the NSOM head needs to be removed and water added to the liquid cell. This is typically followed by a realignment of the optics. Thus the probe is not returned to its previous position over the sample. A solution to this problem is to use a CCD camera to monitor the water level and tuning fork/probe unit with the NSOM head in place. This would allow water to be added to the cell and the liquid level head adjusted without the need to remove the head unit. It is important that the prongs of the fork be kept dry and water not allowed to spill from the cell into into the precision stage since this would ruin this expensive equipment. The camera would also allow for monitoring of the specimen sample without having to open the box enclosure and peer through the microscope.

Image 7.4 indicates the result results for imaging 2 microns resist circles in air. These scans and those of the rat’s fibroblast cells were performed with evaporation compensation. The top two images are 3D and 2D representations of the phase information while the bottom images are 3D and 2D representations of the SFF data It is seen that the features are slightly bigger than 2 microns and that the height is approximately 0.6-0.7 microns if one accounts for slope in the sample.

IMAGING IN AIR

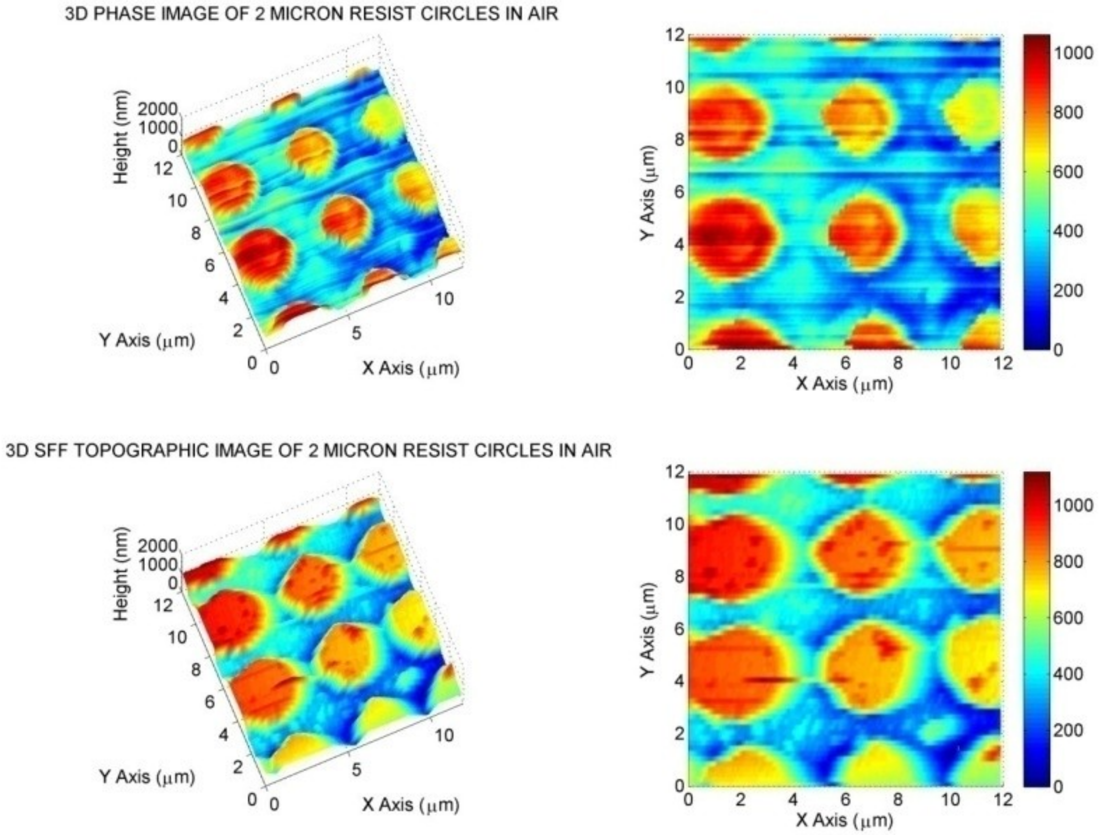
3D PHASE IMAGE OF 2 MICRON RESIST CIRCLES IN AIR

3D SFF TOPOGRAPHIC IMAGE OF 2 MICRON RESIST CIRCLES IN AIR

Figure 7.3: Results for imaging of the resist sample in air. The two images at the top are 3 D (left) and 2D (right) representations of the phase data and the bottom results are 3 D (left) and 2D (right) representations of the SFF information.

Figure 7.4 indicates the results for imaging the same sample in distilled water. As in figure 7.3, the top two images represent the phase results and the bottom two represents the SFF data. The height and shape of the features are consistent with the results obtained in air. These results were reproducible after multiple scans over the period of several hours which verified the efficacy of the evaporation control system.

IMAGING IN DISTILLED WATER

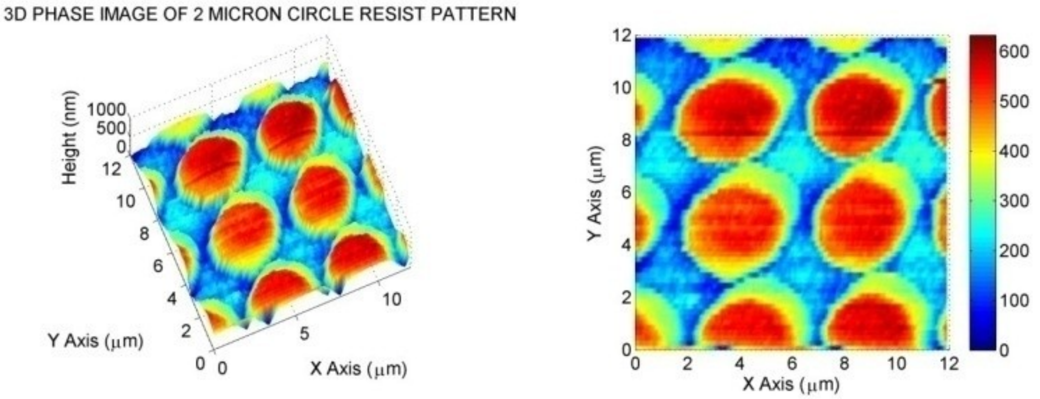
3D PHASE IMAGE OF 2 MICRON CIRCLE RESIST PATTERN

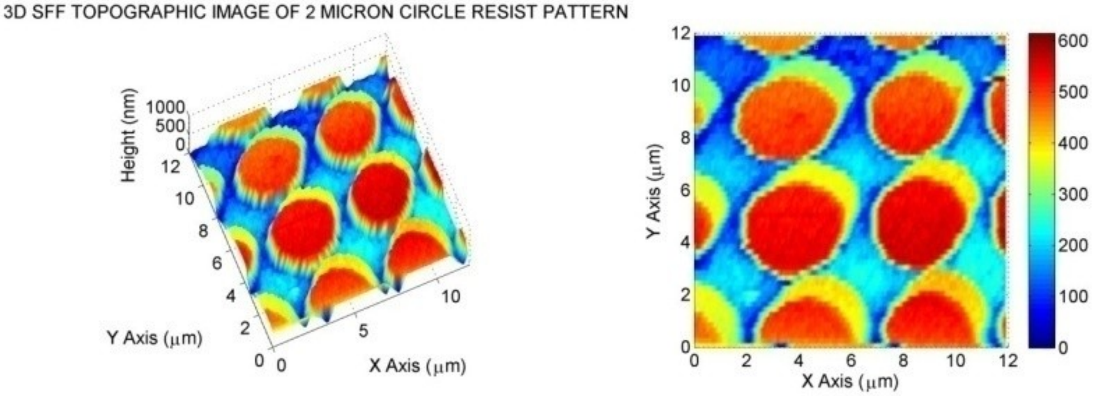
3D SFF TOPOGRAPHIC IMAGE OF 2 MICRON CIRCLE RESIST PATTERN

Figure 7.4: Results for imaging of the resist sample in distilled water with evaporation compensation. The two images at the top are 3 D (left) and 2D (right) representations of the phase data and the bottom results are 3 D (left) and 2D (right) representations of the SFF information. These results compare quite well with those obtained in air.

7.32 Rat fibroblast cells

The rat fibroblast cells were obtained from ATCC (American Type Culture Collection), an independent, private, non-profit biological resource center and research organization. These cells were extracted from a normal rat embryo and derived from the 3T3 line. This line was established in 1962 by two researchers at NYU. The 3T3 has become the standard fibroblast cell line with the "3T3" designation referring to the abbreviation of "3 day transfer, inoculum $3x10^5$ cells". Thus the original embryonic cells were transferred from the original culture every 3 days and inoculated at the rigid density of $3x10^5$ cells per 20 cm^2 dish. Cells with stable growth rates were obtained after 20-30 generations in culture before being labeled 3T3.

Fibroblasts are important cells involved in the synthesis of extracellular matrix and collagen for animal tissue. They play an important role in wound healing and are the most common cells of connective tissue in animals. The term *blast* indicates that these cells are stem cells. Fibroblasts have branched cytoplasm surrounding an elliptical speckled nucleus. I attempted to image the nuclei but the thickness (more than 6 microns) and size (more than 100 microns) precluded such an investigation. The cells were fixed on a glass substrate and the branched cytoplasm regions imaged in air. The cells were then completely immersed in phosphate buffer solution (PBS) and the same regions reimaged. The results of these investigations are presented herein.

The fibroblast cells were fixed onto a quartz glass substrate and imaged in air then in PBS. Two different regions labeled region A and region B in figure 7.5 were imaged. Each region was imaged a total of three times in air and in the buffered solution. The selected regions were chosen to be away from the center of the cell where it was unlikely to find a nucleus or other organelles. It was therefore expected that the content of the cell would be homogenous in these two regions.

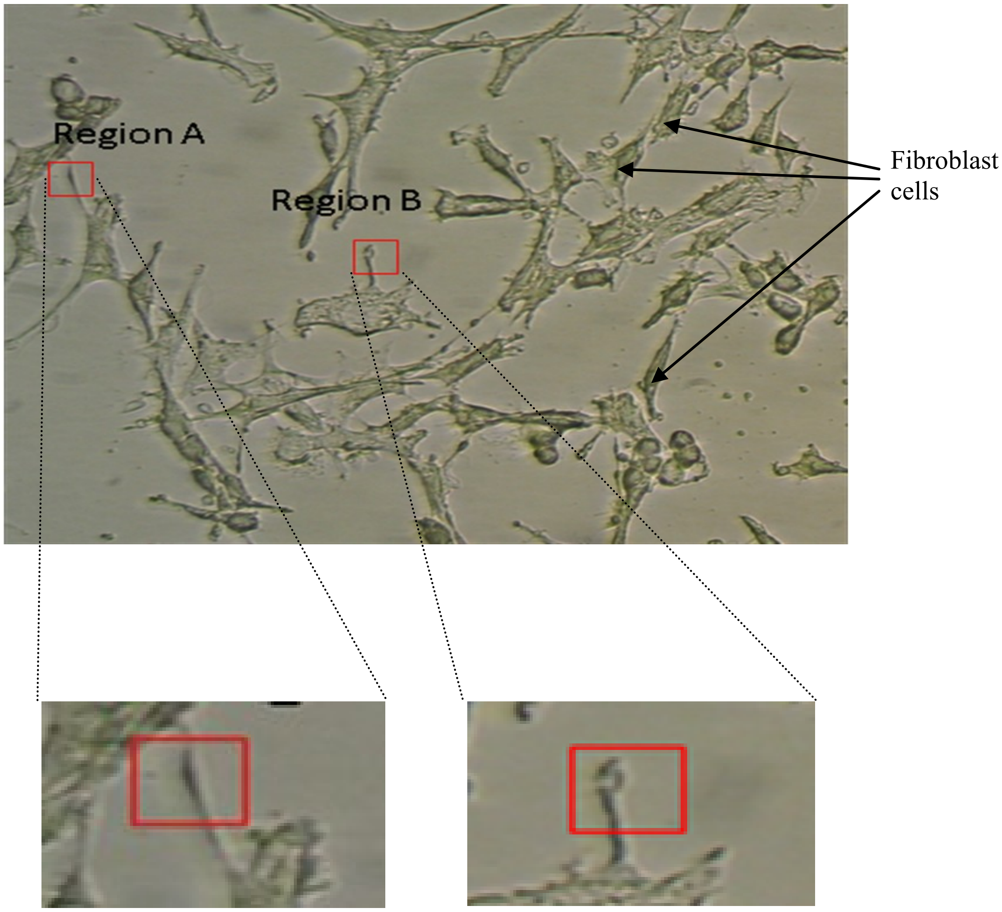

Figure 7.5: Optical image of rat fibroblast cells as seen under an optical microscope at low magnification. The two regions imaged are highlighted as region A and region B. These regions are away from the center of the cell. Magnified images of the region are shown below.

Image 7.6 represents the result obtained for imaging region A in air. The two top images are 3D and 2D representations of the phase data while the bottom images are similar representations of the SFF data. The results in both images compared quite well with each other as expected because the cell is homogenous in this region. Three scans were performed over several hours with excellent reproducibility.

REGION A: AIR

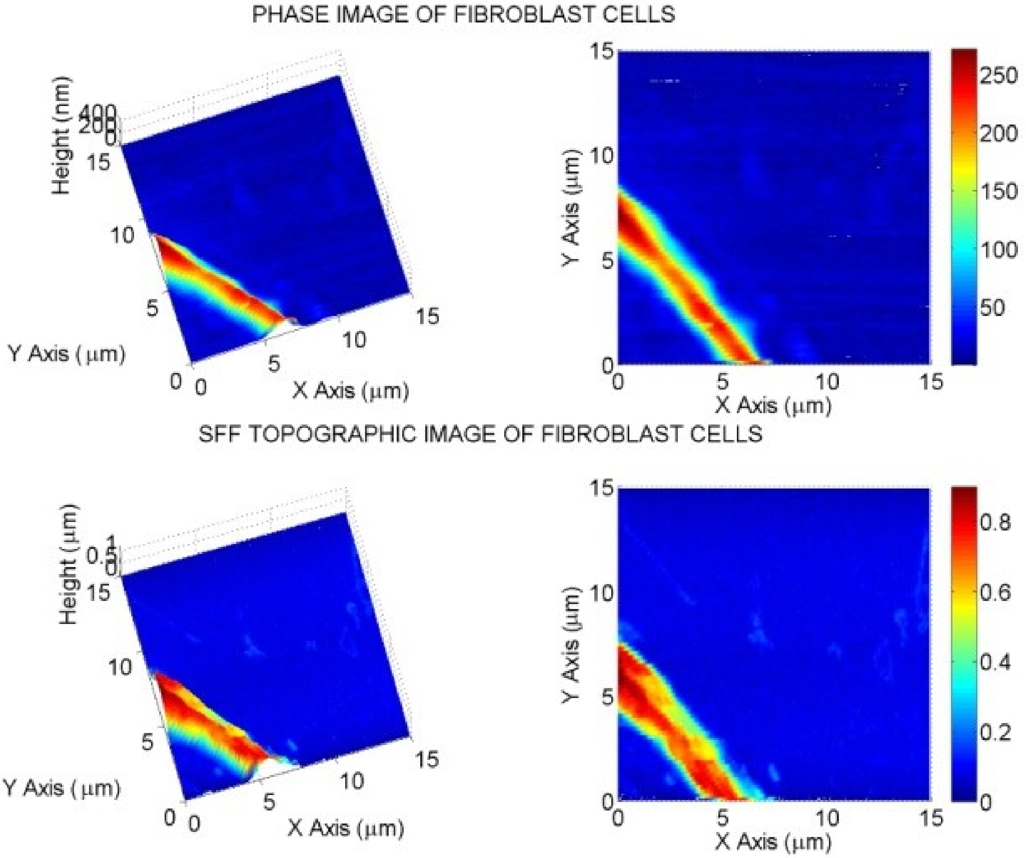

Figure 7.6: Results for region A of fibroblast cells imaged in air. The two images at the top are 3 D (left) and 2D (right) representations of the phase data and the bottom results are 3 D (left) and 2D (right) representations of the SFF information. The phase and SFF compare quite well since region A is homogenous.

Region A was subsequently rescanned with the cells completely immersed in phosphate buffer solution. Evaporation compensation was employed for these scans. A comparison of the images in air and in PBS indicates that the cell exhibits similar shape and height characteristics. This result was highly repeatable and confirmed that there were no artifacts induced by changes in the level of the liquid. It also verified that the feedback system was sufficiently sensitive in a liquid to allow for the imaging of soft samples.

REGION A: PBS SOLUTION

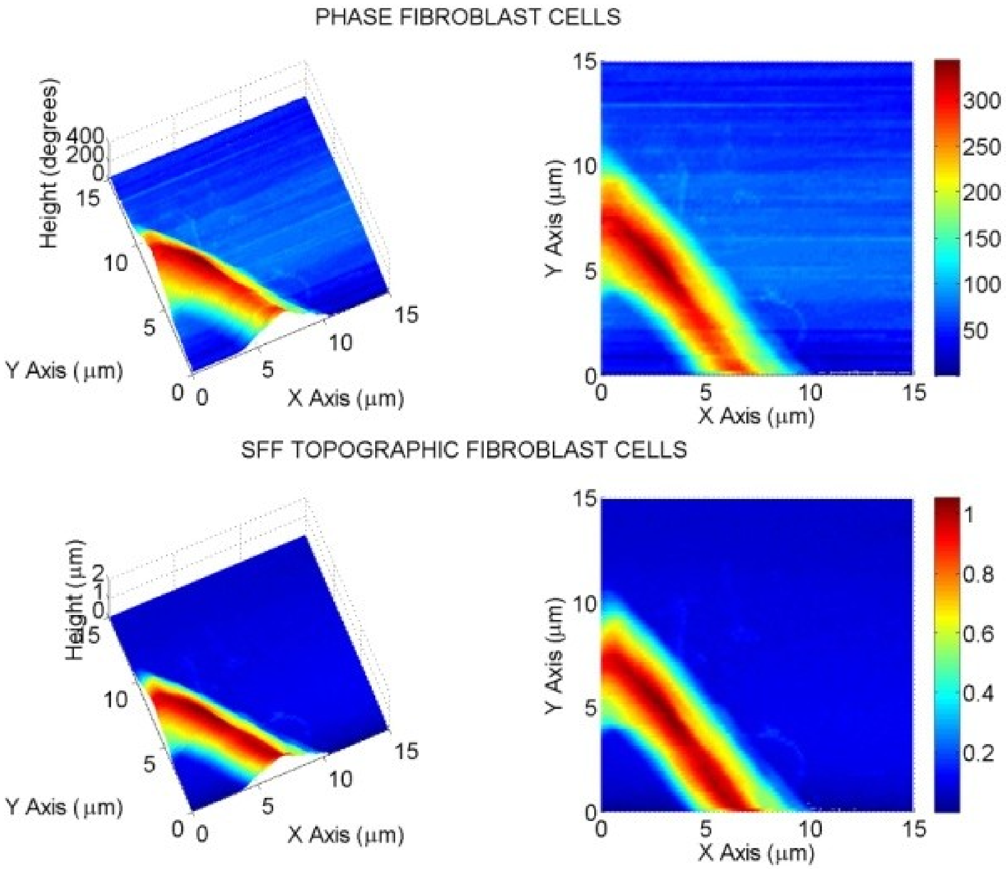

Figure 7.7: Results for region A of the fibroblast cells imaged in PBS. The two images at the top are 3 D (left) and 2D (right) representations of the phase data and the bottom results are 3 D (left) and 2D (right) representations of the SFF information.

To verify these results, a second region of the sample was scanned both in air and in PBS. The results for region B are represented in figures 7.8 and 7.9. The phase and SFF results of figure 7.8 (imaging in air) are quite similar although some of the features in the topography image appear larger than the corresponding features in the phase. The overall shape and morphology of the features in both data sets are nevertheless consistent.

REGION B: AIR

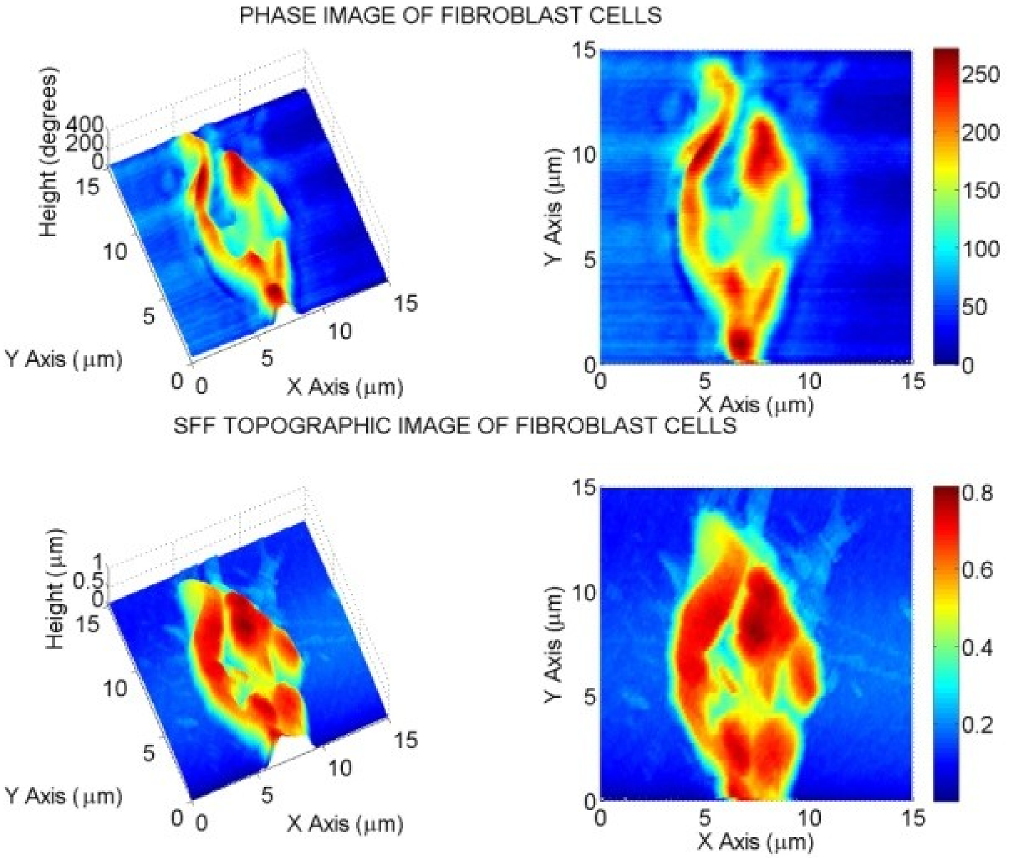

Figure 7.8: Results for region B of the fibroblast cells imaged in air. The two images at the top are 3 D (left) and 2D (right) representations of the phase data and the bottom results are 3 D (left) and 2D (right) representations of the SFF information.

Figure 7.9 presents the results for imaging region B in PBS. It is seen that the phase and topography (SFF) results are in excellent agreement with regard to the surface morphology and size of the feature. As with region A, the reproducibility of the results was excellent.

REGION B: PBS SOLUTION

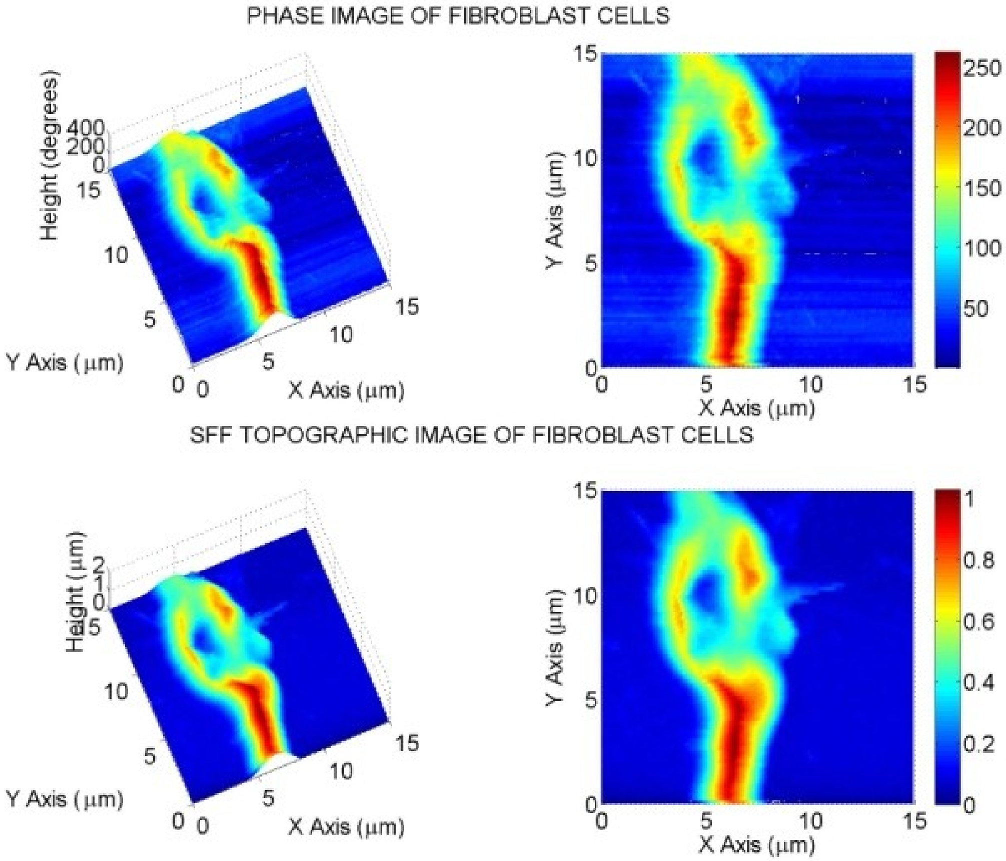

Figure 7.9: Results for region B of the fibroblast cells imaged in PBS. The two images at the top are 3 D (left) and 2D (right) representations of the phase data and the bottom results are 3 D (left) and 2D (right) representations of the SFF information. These results are consistent with those obtained in air.

These results confirm that it is possible to obtain simultaneous SFF and phase information in vivo. Using this information, it is then possible to examine the spatial variations in the refractive index of a cell. This analysis was performed and the results are presented in the next section.

7.4 Cell Refractometry Study

The integrated refractive index at any point (x,y) on a 3D object is given as;

$$n_c(x, y) = \left(\frac{\lambda}{2\pi H(x,y)}\Delta\theta\ (x,y)\right)+1 \qquad (24)$$

where λ is the illumination wavelength, *H (x, y)* is the height of the sample and *Δθ (x, y)* is the measured phase of the sample at the point (x, y). Since *H (x, y)* and *Δθ (x, y)* are determined directly from the SFF and phase data, it is relatively straightforward to determine the refractive index at the point *(x, y).* As is the case with image subtraction, it is critical that the two images are precisely registered.

For this investigation, the refractive index was determined at five different points for regions A and B as indicated in figure 7.9.1. For each region, the refractive index was determined both in air and in phosphate buffer solution.

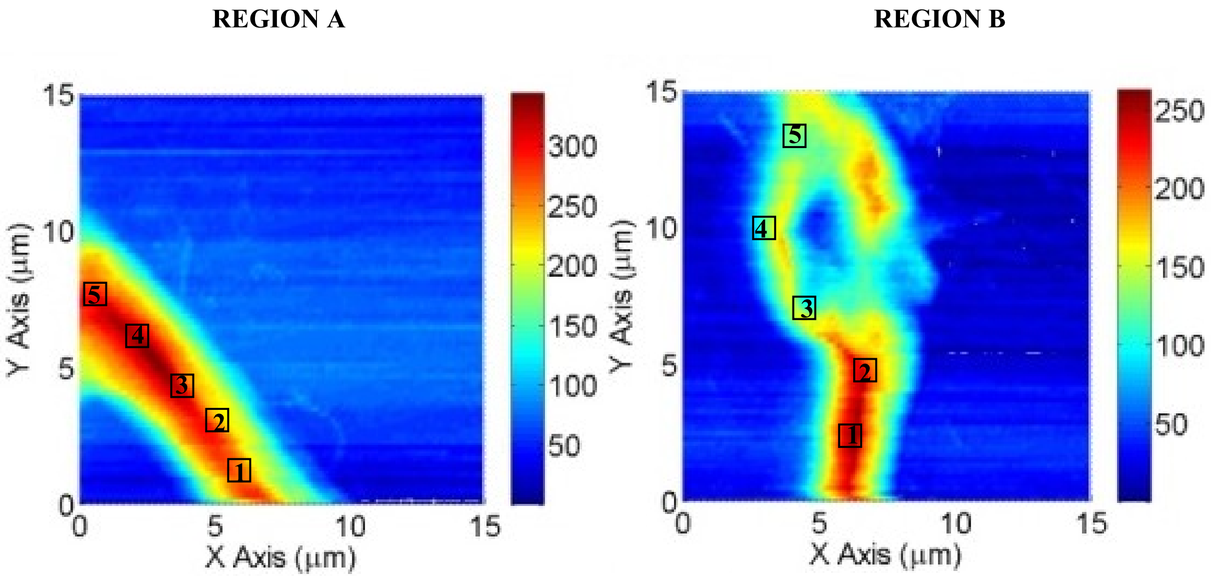

Figure 7.10: The two images shown indicate the five points on regions A and B for which the refractive index was determined. Each region was scanned a total of three times both in air and in water, from which an average refractive index value was determined for each of the five point and finally, for the region.

Each region was scanned a total of three times in air and in water. The results of this investigation are shown in table 1. Each of the five values for regions A and B represent the average refractive index at that point for three successive scans.

Table 1: The table on the left represents the average refractive index information at five different points from regions A for 3 successive scans. The refractive index information for scans in both air and PBS are indicated. The table on the right represents the same information for region B.

Region A	**n (AIR)**	**n (WATER)**
1	1.48	1.46
2	1.59	1.40
3	1.56	1.43
4	1.50	1.44
5	1.57	1.45
AVERAGE	**1.54**	**1.44**

Region B	**n (AIR)**	**n (WATER)**
1	1.46	1.42
2	1.49	1.40
3	1.52	1.43
4	1.55	1.44
5	1.57	1.45
AVERAGE	**1.52**	**1.43**

A standard deviation of ± 0.02 was determined for the refractive index value of the system in air and water. This was determined by repeatedly scanning a given region of a fibroblast cell a total of 10 times in the x direction without y translation. This was repeated at 5 different locations for the selected cell. In total, three cells were scanned in this manner both in air and in PBS. The selected regions were chosen to be away from the cell's center for reasons previously mentioned.

For both regions, we can conclude that the average refractive index (RI) value in air is higher than the average value in water, since the difference in the two values (~ 0.9) is well outside the margin of error in the measurement. This is predicted from the equation $n = n_o + \alpha C$ where n_o is the refractive index of the cell's cytoplasm (~1.33), α is the specific refraction increment which depends on the nature of the solute of the cytoplasm (e.g. whether proteins or lipids are present and in what proportion) and C is the concentration of the fluid which makes up the cytoplasm [88]. Thus when the cell is place in PBS, this reduces C and the refractive index *n* decreases.

In both air and water, Region A yielded a slight higher refractive index value than region B but the difference is with the margin of error and not significant. The refractive index of a cell is strongly influenced by the composition of bimolecular ingredients such as lipids, sugars, proteins, etc [90]. Of all the ingredients, proteins are the main contributors due to their abundance and high refractive index (1.50-1.58) [91]. In air, the average refractive index of regions A and B are 1.54 and 1.52 respectively which is probably due to a high concentration of proteins in these regions. The refractive index values obtained for the fibroblast cells in a buffer solution falls within the expected range of 1.4 to 1.5 [94].

There is a growing interest in the use of refractive index information for the identification of pre-invasive and pre-cancerous cells. Before cells become invasive, the nuclear architecture changes, becoming enlarged and crowded [92]. The resulting change in the refractive index can range from 0.04 to 0.06 [93]. This expected change in the refractive index is larger than the measurement error of my system, and is probably detectable using the current setup. Thus the potential exist for oncology studies with single cells.

7.5 Conclusion

It has been clearly demonstrated that the shear-force feedback/scanning quantitative phase system can be stabilized in a liquid environment. The liquid scans were highly reproducible over a period of several hours. This opens up a new avenue for in vivo biological studies. It was also demonstrated that cell refractometry analysis was possible in both air and in a liquid without any ad hoc modifications. These results are applicable to oncology studies since a clear relationship between intracellular refractive index and the onset of certain types of cancer has been established. A possible area of future research is in high speed imaging. This is discussed further in chapter 8.

CHAPTER 8: FUTURE WORK

8.1 Limitations of the current system:

Incorporating a stabilized part fiber/ part air interferometer into a conventional near-field scanning optical microscope allows for ultra high optical resolution. The resolution of the system is a function of the aperture size of the probe. As the aperture size is reduced, there is a corresponding improved resolution capacity which results from the restricted spatial extent of the evanescent field from the probe. This improvement in resolution is achieved at the expense of a reduction in throughput, which places a severe restriction on the thickness of the samples which can be successfully imaged. In spite of this, the phase contrast NSOM yields the highest resolution quantitative phase results of any contemporary quantitative phase technique. This is the case because without exception, these techniques yield diffraction limited results. However, many of these techniques are full field. Thus the entire region of interest is imaged in a single frame and image acquisition is typical limited by the acquisition rate of the system's image capture device. The Fourier phase contrast microscope for example, has an image acquisition rate in the millisecond range [23]. My system by comparison has an acquisition time of almost 40 minutes for a scan of a 15 micron x 15 microns with a step size of 100nm. Dynamic biological processes occur over the time scale of milliseconds to a few seconds

[98] and as such are precluded from investigation with the current setup. Towards the goal of improving the temporal resolution of the system, there are two distinct approaches which may be adopted. The first approach involves the incorporation of a full field imaging modality into the current system. In this approach, the system would have two modes of operation. In the so called “fast mode”, a large region of interest would be quickly scanned to assist in the identification of specific regions of interest. However, only quantitative phase data would be acquired. These regions would be subsequently scanned in the slow, high resolution mode in which both phase and topography data would be acquired.

The second approach entails improving the overall temporal resolution of the current system (i.e. speeding up the scanning process). Since the rate of phase acquisition can be significantly improved relatively easily, the main challenge in this approach would be to improve the temporal resolution of the SFF data acquisition. This is an ongoing area of research and several approaches have been proposed for achieving this objective [95 - 97]. Invariably, the maximum scan rate is determined by the resonant frequency of the scanner but newer and faster scanners are constantly being developed. In spite of this fact, it is probably unrealistic to expect to achieve an acquisition time of much less than 1 second for a “regular” size scan (15 microns x 15 microns) especially if the sample specimen is more than 1 micron in thickness. Nevertheless, I will further discuss the details of both ideas in the next two sections.

8.2 Full Field Quantitative Imaging

Many of the contemporary techniques for quantitative phase imaging use a full field setup in which the entire region of the sample to be imaged is illuminated. Although there exit a few approaches which are based on image acquisition using a single interferogram [7,12], my inclination would be to adopt phase shifting approach since the setup is straightforward and can be easily incorporated into my current setup. Using a phase shifting approach, several interferograms (3 to 4 in most cases) are acquired from which the sample phase is determined. This was discussed in chapter 1. Subsequent phase unwrapping if often required but since the rate of acquisition of the interferograms is determined primarily by the speed of the image capture device, these techniques offer very high temporal resolution. In published results [23], it has been demonstrated that full-field phase images can be acquired in milliseconds. It may be possible to adapt the current system for full field imaging using a cleaved probe instead of a tapered NSOM probe. This would also allow for the imaging of samples much greater thicker than 6 microns and for scans sizes far greater than the usual 15 microns x 15 microns. I would suggest using phase shifting interferometry to acquire at least four interferograms which would then be used for phase determination as described in chapter 1. Once a specific region of interest is identified, an NSOM probe can then be spliced onto the cleaved fiber and the sample imaged in a high resolution mode.

8.2.1 High speed NSOM

It has been established that high speed NSOM imaging requires a quartz tuning fork with a resonant frequency of at least 100 kHz. The tuning forks used in my setup have a resonant frequency of approximately 32.76 kHz. At 100 kHz, the system has a much faster response time since sample information is accessed much more rapidly. This would require a faster lock-in than that currently used (current lock-in operate in the kHz range) and a reduction of the time constant on the feedback PI circuit. However, it is important to keep in mind that an inherent limit to data acquisition using this approach is the resonant frequency of the precision stage. Fortunately, a high frequency tuning fork is not necessarily required for high speed SFF imaging. In a paper by Humphris et al, the author was successful in achieving an acquisition rate of 100 frames per second by vibrating a probe with amplitude of several microns instead of a few nanometers which is typical. Using a 32.76 kHz tuning fork, the author was able to obtain a fast line scan for each oscillation cycle of the probe, and a slow scan as the probe was advanced. Thus the amplitude of the probe oscillation dictated the scan size in one direction and the displacement during advancement in the slow line scan determined the scan size in the orthogonal direction. My preference would be to use a high frequency fork and to operate the system well below the resonant frequency of the stage, but it is nevertheless possible to significantly reduce the data acquisition time for the SFF system.

8.2.2 High speed scanning quantitative phase

The temporal resolution of the quantitative phase imaging component of the current system can be significantly improved by increasing the modulation frequency to the fiber wrapped PZT shown in figure 2.1. Commercially available ceramic cylindrical PZTs can be modulated at frequencies upwards of 100 kHz, which is 100 times faster than the current modulation. However, heating of the actuator at these high frequencies can potentially result in thermal instability problems. Nevertheless, simply increasing the modulation frequency of the fiber wrapped PZT and appropriately adjusting the time constants on the lock-in amplifiers and PI circuits is sufficient to meet the stated objective. The lock-in in current use is the SR830 which operates at frequencies ranging from 1 millihertz to 100 kilohertz with an adjustable time constant from 10 microseconds to 30 kiloseconds. The time constant of the PI circuit which controls the galvanometer in the current setup, was reduced to the point where the motion of the plate was severely under-damped. Thus there exists significant unutilized capability within the current system even without increasing the modulation frequency.

Further capacity and far greater speeds can be achieved via acousto-optic frequency shifting or heterodyne interferometry. The basic idea of heterodyne interferometry is to introduce a small frequency shift Δf between two interfering beams. This is typically accomplished using an acousto-optic modulator (AOM) which is a device which makes use of the acousto-optic effect to diffract and shift the frequency of light using sound waves. Commercially available AOMs can produce frequency shifts ranging from a few hundred kilohertz to several hundred megahertz. Acousto-optic modulators operating at 40 MHz and below are cheap and widely available. The SR 844 lock-in can operate at frequencies as high as 200 MHz and is compatible with most commercially available AOMs. Acousto-optic modulators produce a relative frequency shift between interfering signals which results in an intensity modulated interference signal at a beat frequency equal to the shift.

A proposed setup is shown in figure 8.1. The AOM is placed in one of the output arms of the bi-directional coupler to exploit the stabilization system of the current setup. For data acquisition rates in the millisecond time scale, environmentally induced noise is unlikely to exert much of an influence on the system. If this is the case, the AOM can be placed immediately after the laser source with the shifted and un-shifted components launched into separate, uncoupled input arms. In either setup, the detected output signal will be modulated at a beat frequency equal to the frequency shift between the light traversing the reference and sample arms. Induced phase in the sample arm can be extracted by demodulating the interference signal using a lock-in amplifier referenced at this beat frequency.

It can be shown that the electric fields for the sample and reference arms of the interferometer shown in figure 8.1 are given *by* $E_1cos(\omega_1t+\theta_s)$ and $E_2cos(\omega_2t)$ respectively where θ_s is the sample phase, $\omega_1=2\pi(f+\Delta f)$ and $\omega_2=2\pi f$. After filtering out high frequency and dc terms, the output signal is given by $E_1E_2cos(\Delta f+\theta_s)$. Synchronized detection of the heterodyne signal with a high speed lock-in allows for the extraction of the phase θ_s. This information can then be used to actively adjust the angular position of the precision galvanometer as explained in chapter 2, which would obviate the need for phase unwrapping.

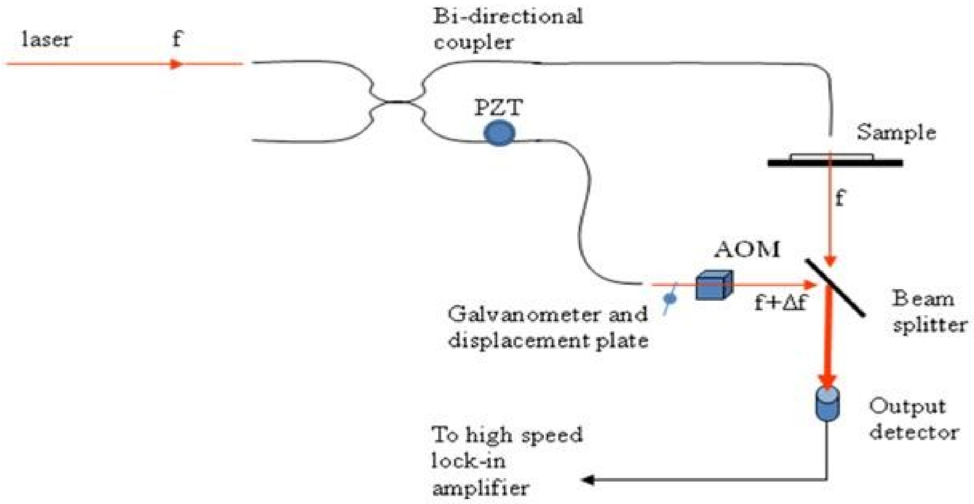

Figure 8.1: Experimental setup of a heterodyne scanning system for rapid phase data acquisition. An acousto-optic phase modulator in the reference arm outputs a signal given by f+Δf where Δf is the frequency shift introduced by the modulator. The light in the sample arm has a frequency of f. Thus the resultant interference signal is intensity modulated at Δf. A high speed lock-in is used to demodulate this signal and extract the sample phase.

It should therefore be possible to complete full scans with acquisition rates of a few seconds and potentially in the millisecond time scale, without the need for post imaging unwrapping. A procedure similar to the one proposed here has been successfully implemented in an NSOM but without environmental stabilization and real-time unwrapping [99].

8.3 Conclusion

A novel procedure has been presented for the investigation of subsurface intracellular features. This technique is noninvasive and requires only a single scan for the acquisition of the data required for subsurface information extraction. With only minor modifications, it was possible to perform cellular refractometry studies on biological samples in an aqueous environment. The system has the drawback of a long acquisition time. This is balanced by the ultra-high resolution capability for thin samples but the low temporal resolution essentially excludes dynamic studies. Although this system can be sped up, it is in my opinion inherently unsuited for dynamic studies. Exceptions would include dynamic processes which occur over a very long period of several seconds to a few minutes. I believe that the future of this instrument lies in a dual mode operation. In the high resolution mode, the instrument would operate in a scanning regime acquiring simultaneous SFF topography data and phase information. In the fast mode, the instrument would operate in a full-field high temporal resolution regime acquiring only phase information. Nevertheless, the heterodyne technique previously described should allow for a much shorter acquisition time which is always desirable.

REFERENCES

1. C. H. Yang, A. Wax, I. Georgakoudi, E. B. Hanlon, K. Badizadegan, R. R. Dasari and M. S. Feld, "*Interferometric phase dispersion microscopy* ," Opt. Lett. **vol. 25**, 1526-1528 (2000).

2. Julian. N. Walford, Keith, A. Nugent, Ann. Roberts and Robert. E. Scholten, "*Three-dimensional phase imaging with a scanning optical-fiber interferometer*," Appl. Opt. **vol.38**, 3508-3515(1999).

3. M. R. Arnison, K.G. Larkin, C. J. R. Sheppard, N. I. Smith and C. J. Cogswell, "*Linear phase imaging using differential interference contrast microscopy*," Journ. of Micros, **vol. 214**, 7-12 (2004).

4. Andrew Ahn, Changhuei Yang, Adam Wax, Gabriel Popescu, Christopher Fang-Yen, Kamran Badizadegan, Ramachandra R. Dasari and Michael S. Feld , "*Harmonic phase-dispersion microscope with a Mach-Zehnder interferometer*," Appl. Opt. **vol. 44**, 1188-1190 (2005).

5. Hidenao Iwai, Christopher Fang-Yen, Gabriel Popescu, Adam Wax, Kamran Badizadegan, Ramachandra R. Dasari and Michael S. Feld, "*Quantitative phase imaging using actively stabilized phase-shifting low coherence interferometry*," Opt. Lett. **vol. 29**, 2399-2401(2004).

6. Xinghong Li, Toyohiko Yamauchi, Hidenao Iwai, Yutaka Yamashita, Haijun Zhang and Teruo Hiruma, "*Full-field quantitative phase imaging by white-light interferometry with active phase stabilization and its application to biological samples*," Opt Lett. **vol. 31**, 1830-1832 (2006).

7. Takahiro Ikeda,Gabriel Popescu, Ramachandra R. Dasari and Michael S. Feld, "*Hilbert phase contrast microscopy for investigating fast dynamics in transparent system*," Opt Lett. **vol. 30**, 1165-1167(2005).

8. Gabriel Popescu, Lauren P. Deflores, Joshua C Vaughan, Kamran Badizadegan, Hidenao Iwai, Ramachandra R. Dasari and Michael S. Feld, "*Fourier phase microscopy for investigation of biological structures and dynamics*," Opt. Lett. **vol. 29**, 2503-2505 (2004).

9. M. Servin, J. L. Marroquin, D. Malacara and F.J. Cuevas, "*Phase unwrapping with a regularized phase-tracking system*," Appl. Opt**. vol. 37**, 1917(1998).

10. Liangliang Zhang, Yan Zhang, Cunlin Zhang, Yuejin Zhao and Xiaohua Liu, "*Terahertz multi-wavelength phase imaging without 2π ambiguity*," Opt. Lett. **vol. 31**,3668-3670 (2006).

11. C. Polhemus, "*Two-wavelength interferometry*," App. Opt. **vol. 12** , 2071-2074 (1973).

12. Daniel Parshall and Myung K. Kim, "*Digital holographic microscopy with dual wavelength phase unwrapping*," Appl. Opt. **vol. 45**, 451-459 (2006).

13. N. Lue, G. Popescu, T. Ikeda, R. R. Dasari, K. Badizadegan, and M. S. Feld, "*Live cell refractometry using microfluidic devices*," Opt. Lett. **vol. 31**, 2759-2761 (2006).

14. B. Rappaz, P. Marquet, E. Cuche, Y. Emery, C. Depeursinge, and P. Magistretti, "*Measurement of the integral refractive index and dynamic cell morphometry of living cells with digital holographic microscopy*," Opt. Exp. **vol. 13**, 9361-9373 (2005).

15. R. Barer, K. F. A. Ross and S. Tkaczk,"*Refractometry of Living Cells*," Nature **vol. 171**, 720-724(1953).

16. V. Backman, M. B. Wallace, L. T. Perelman, J. T. Arendt, R. Gurjar, M. G. Müller, Q. Zhang, G. Zonios, E. Kline, T. McGillican, S. Shapshay, T. Valdez, K. Badizadegan, J. M. Crawford, M. Fitzmaurice, S. Kabani, H. S. Levin, M. Seiler, R. R. Dasari, I. Itzkan, J. Van Dam and M. S. Feld, "*Detection of Pre-invasive Cancer cells*," Nature **vol. 406**, 35-36 (2000).

17. K. Edward, "*A novel technique for phase imaging in the near-field and its application to the imaging of biological specimens*," Thesis (M.S.) University of North Carolina Charlotte, (2005).

18. W. H. Wolberg, W. Nick Street and O. L. Mangasarian, "*Importance of Nuclear Morphology in Breast Cancer Prognosis*," Clin. Cancer Res. **vol. 5**, 3542-3548 (1999).

19. F. Zernike, "*How I discovered phase contrast*," Science **vol. 121**, 345-349 (1955).

20. Maksymilian Pluta, "*Nomarski's DIC microscopy: a review*," **vol. 1846**,Proc. SPIE (1994).

21. Robert Hoffman and Leo Gross, "*Modulation Contrast Microscope*," Appl. Opt. **vol. 14**, 1169-1176 (1975).

22. Gabriel Popescu, Takahiro Ikeda, Catherine A. Best, Kamran Badizadegan, Ramachandra R. Dasari, and Michael S. Feld, "*Erythrocyte structure and dynamics quantified by Hilbert phase microscopy*," J. Biomed. Opt. **vol. 10**, 060503(1-3) (2005).

23. G. Popescu, L. P. Deflores, J. C. Vaughan, K. Badizadegan, H. Iwai, R. R. Dasari and M. S. Feld, "*Fourier phase microscopy for investigation of biological structures and dynamics*," Opt. Lett. **vol. 29**, 2503-2505 (2004).

24. Gabriel Popescu, Takahiro Ikeda, Ramachandra R. Dasari, and Michael S. Feld, "*Diffraction phase microscopy for quantifying cell structure and dynamics*," Opt. Lett. **vol. 31**, 775-777 (2006).

25. Hidenao Iwai, Christopher Fang-Yen, Gabriel Popescu, Adam Wax, Kamran Badizadegan, Ramachandra R. Dasari, and Michael S. Feld, "*Quantitative phase imaging using actively stabilized phase-shifting low-coherence interferometry*," Opt. Lett. **vol. 29**, 2399-2401 (2004).

26. Desmond C. Adler, Robert Huber, and James G. Fujimoto,"*Phase-sensitive optical coherence tomography using buffered Fourier domain mode-locked lasers at up to 370,000 scans per second*," Proc. SPIE 6429, (2007).

27. Pierre Marquet, Benjamin Rappaz, Pierre J. Magistretti, Etienne Cuche, Yves Emery, Tristan Colomb, and Christian Depeursinge, "*Digital holographic microscopy: a noninvasive contrast imaging technique allowing quantitative visualization of living cells with subwavelength axial accuracy*," Opt. Lett**. vol. 30**, 468-470 (2005).

28. Toyohiko Yamauchi, Hidenao Iwai, Mitsuharu Miwa, and Yutaka Yamashita, "*Low-coherent quantitative phase microscope for nanometer-scale measurement of living cells morphology*," Opt. Exp. **vol. 16**, 12227-12238 (2008).

29. Christopher J. Mann, Philip R. Bingham, Vincent C. Paquit, and Kenneth W. Tobin, "*Quantitative phase imaging by three-wavelength digital holography*," Opt. Express vol. **16**, 9753-9764 (2008).

30. Kaveh Azartash, Enrico Gratton, "*Obtaining Quantitative Information on the Cell-induced Deformation of Collagen with Digital Holographic Microscopy*," Biophys. Journ. **vol. 96** (2008).

31. Christopher J. Mann, Philip R. Bingham, Vincent C. Paquit, and Kenneth W. Tobin, "*Quantitative phase imaging by three-wavelength digital holography*," Opt. Express **vol. 16**, 9753-9764 (2008).

32. Hariharan Subramanian, Prabhakar Pradhan, Yang Liu, Ilker R. Capoglu, Jeremy D. Rogers, Hemant K. Roy, Randall E. Brand, and Vadim Backman, "*Partial-wave microscopic spectroscopy detects subwavelength refractive index fluctuations: an application to cancer diagnosis*," Opt. Lett. **vol. 34**, 518-520 (2009).

33. Guy Indebetouw, Yoshitaka Tada, and John Leacock, "*Quantitative phase imaging with scanning holographic microscopy: an experimental assessment*," Biomed Eng Online **vol. 5** (2006).

34. Andrew W. Kulawiec and Duncan T. Moore, "*Quantitative phase imaging in confocal microscopy by optical differentiation*," Appl. Opt.**vol. 33**, 6582-6590 (1994).

35. Christopher G. Rylander, Digant P. Dave, Taner Akkin, Thomas E. Milner, Kenneth R. Diller, and Ashley J. Welch, "*Quantitative phase-contrast imaging of cells with phase-sensitive optical coherence microscopy*," Opt. Lett. **vol. 29**, 1509-1511 (2004).

36. Niyom Lue, Wonshik Choi, Kamran Badizadegan, Ramachandra R. Dasari, Michael S. Feld, and Gabriel Popescu, "*Confocal diffraction phase microscopy of live cells*," Opt. Lett. **vol. 33**, 2074-2076 (2008).

37. Y.a.n. Zhang, Giancarlo Pedrini, Wolfgang Osten, Hans J. Tiziani, "*Phase retrieval microscopy for quantitative phase-contrast imaging*," Optik - International Journal for Light and Electron Optics, **vol. 15**, 94-96 (2004).

38. Peter L. Wizinowich, "*Phase shifting interferometry in the presence of vibration: a new algorithm and system*," Appl. Opt. **vol. 29**, 3271-3279 (1990).

39. Gabriel Popescu, YoungKeun Park, Wonshik Choi, Ramachandra R. Dasari, Michael S. Feld, Kamran Badizadegan, "*Imaging red blood cell dynamics by quantitative phase microscopy*," Blood Cells, Molecules, and Diseases, **vol 41**, 10-16 (2008).

40. Niyom Lue, Wonshik Choi, Gabriel Popescu, Takahiro Ikeda, Ramachandra R. Dasari, Kamran Badizadegan, and Michael S. Feld, "*Quantitative phase imaging of live cells using fast Fourier phase microscopy*," Appl. Opt**. vol. 46**, 1836-1842 (2007).

41. B. Braunecker, A. W. Lohmann, "*Character recognition by digital holography*," Opt. Comm. **vol. 11**,141-143 (1974).

42. Joseph Rosen and Gary Brooker, "*Digital spatially incoherent Fresnel holography*," Opt. Lett. **vol. 32**, 912-914 (2007).

43. Christopher Mann, Lingfeng Yu, Chun-Min Lo, and Myung Kim, "*High-resolution quantitative phase-contrast microscopy by digital holography*," Opt. Express **vol. 13**, 8693-8698 (2005).

44. Etienne Cuche, Frédéric Bevilacqua, and Christian Depeursinge, "*Digital holography for quantitative phase-contrast imaging*," Opt. Lett. **vol. 24**, 291-293 (1999).

45. A. Barty, K. A. Nugent, D. Paganin, and A. Roberts, "*Quantitative optical phase microscopy*," Opt. Lett. **vol. 23**, 817-819 (1998).

46. Paganin, D., and Nugent, K.A,"*Non-interferometric phase imaging using partially coherent light*," Phys. Rev. Lett., **vol. 80**, 2586–2589 (1998).

47. M. Vaez-Iravani and R. Toledo-Crow, "*Phase contrast amplitude pseudoheterodyne interference near-field scanning optical microscope*," Appl. Phys. Lett. **vol. 62**, 1044-1046 (1993).

48. Saeed Pilevar, Walid. A. Atia, Christopher. C. Davis, "*Reflection near-field scanning optical microscope: An interferometric approach*," Ultramicroscopy **vol. 61**, 233-236 (1995).

49. Antonello Nesci, René Dändliker, and Hans Peter Herzig, "*Quantitative amplitude and phase measurement by use of a heterodyne scanning near-field optical microscope*," Opt. Lett. **vol. 26**, 208-210 (2001).

50. Gajendra S. Shekhawat and Vinayak P. Dravid Nanoscale, "*Imaging of Buried Structures via Scanning Near-Field Ultrasound Holography*," Science **vol. 310**, 89-92 (2005).

51. YongKeun Park, Monica Diez-Silva, Gabriel Popescu, George Lykotrafitis, Wonshik Choi, Michael S. Feld, and Subra Suresh, "*Refractive index maps and membrane dynamics of human red blood cells parasitized by Plasmodium falciparum*," PNAS **vol.37**, 13730-13730 (2008).

52. Thomas Taubner, F. Keilmann, and R. Hillenbrand, "*Nanoscale-resolved subsurface imaging by scattering-type near-field optical microscopy*," Opt. Express **vol.13**, 8893-8899 (2005).

53. Gabriel Popescu, Kamran Badizadegan, Ramachandra R. Dasari, and Michael S. Feld, "*Observation of dynamic subdomains in red blood cells*," J. Biomed. Opt. **vol. 11**, 040503(1-3), (2006).

54. Minoru Takeuchi, Hiroshi Miyamoto, Yasushi Sako, Hideo Komizu, and Akihiro Kusumi, "*Structure of the Erythrocyte Membrane Skeleton as Observed by Atomic Force Microscopy*," Biophysical Journal **vol.74**, 2172-2183(1998).

55. Levi A. Gheber, Jeeseong Hwang and Michael Edidn, "*Design and optimization of a near-field scanning optical microscope for imaging biological samples in a liquid*," Applied Optics **vol. 37**, 3574-3581 (1998).

56. P. Lambelet, M. Pfeffer, A. Sayah, F. Marquis-Weible, "*Reduction of tip-sample interaction forces for scanning near-field optical microscopy in a liquid environment, Ultramicroscopy*," **vol. 71**, 117-121 (1998).

57. M. Koopman, B.I. de Bakker, M.F. Garcia-Parajo and N.F. van Hulst, "*Shear force imaging of soft samples in liquid using a diving bell concept*," Applied Physics Lett. **vol. 83**, 5083-5085 (2003).

58. W. H. J. Rensen, N. F. van Hulst, and S. B. Kammer, "*Imaging soft samples in liquid with tuning fork based shear force microscopy*," Appl. Phys. Lett. **vol. 77**, 1557 (2000).

59. Robert J Hocken, "*Refractive index of Xenon near critical point*" (PhD thesis 1972).

60. Andrew Ahn, Changhuei Yang, Adam Wax, Gabriel Popescu, Christopher Fang-Yen, Kamran Badizadegan, Ramachandra R. Dasari and Michael S. Feld , "*Harmonic phase-dispersion microscope with a Mach-Zehnder interferometer*," Appl. Opt. **vol. 44**, 1188-1190 (2005).

61. Erik H. W. Meijering, Karel J, Zuiderveld and Max A. Viergever, "*Image registration for digital subtraction angiography*," Int. Journ. of Comp. Vision **vol. 31**, 227-246 (1999).

62. J.-M. Friedt and E. Carry, "*Introduction to the quartz tuning fork*," Am. J. Phys. **vol. 75**, 415-422 (2007).

63. Robert D. Grober, Jason Acimovic, Jim Schuck, Dan Hessman, Peter J. Kindlemann, Joao Hespanha, A. Stephen Morse, Khaled Karrai, Ingo Tiemann, and Stephan Manus, "*Fundamental limits to force detection using quartz tuning forks*," Rev. Sci. Instrum. **vol. 71**, 2776-2780 (2000).

64. Khaled Karrai and Ingo Tiemann, "*Interfacial shear force microscopy*," Phys. Rev. B, **vol. 62**, 174-181 (2000).

65. Tianhao Zhang & Zheyu Fang & Jianya Zheng & Limo Gao & Haidong Yang & Meirong Yin & Jia Yang & Yanzhen Lu & Huizhen Kang & Dapeng Yang & Huizhan Yang, "*The Influence Of Humidity On The Shear Force Between Tip And Sample In NSOM Using Piezoelectric Fork*," Surface Review and Letters**, vol. 12**, 355-358 (2005).

66. J. Zhang and S. O'Shea, "*Tuning forks as micromechanical mass sensitive sensors for bio- or liquid detection*," Sensors and Actuators B: Chemical, **vol. 94**, 65-72 (2003).

67. Manhee Lee, Junghoon Jahng, Kyungho Kim, and Wonho Jhe, "*Quantitative atomic force measurement with a quartz tuning fork*," Appl. Phys. Lett. **vol. 91**, 023117(1-3) (2007).

68. A Castellanos-Gomez, N Agraït and G Rubio-Bollinger, "*Dynamics of quartz tuning fork force sensors used in scanning probe microscopy*," Nanotechnology **vol. 20**, 1-8 (2009).

69. Henri Jansen, Han Gardeniers, Meint de Boer, Miko Elwenspoek and JanFluitman, "*A survey of reactive ion etching of silicon in microtechnology*," Journal of Micromech. and Microeng. **vol. 6**, 14-28 (1996).

70. M. Zaim, A. Aitio, N. Nakashima, "*Safety of pyrethroid-treated mosquito nets*," Medical and Veterinary Entomology**, vol. 14**, 1-5(2000).

71. W. Trager and J.B. Jensen, "*Human malaria parasites in continuous culture*," Science **vol. 193**, 673-675 (1976).

72. M.A. Paesler and P.J. Moyer, "*Near-field Optics: Theory, Instrumentation and Applications*," (John Wiley & Sons, Inc., New York, 1996).

73. Kate Hsu and Levi. A. Gheber, "*Tip-sample interaction in a shear-force near-field scanning optical microscope*," Review of Scientific Instruments, **vol. 70**, 3609-3613 (1999).

74. Elizabeth S. Erickson and Robert C. Dunn, "*Sample heating in near-field scanning optical microscopy*," Appl. Phys. Lett. **vol. 87**, 201102 (2005).

75. Raoul Stockle, Christian Fokas, Volker Deckert, Renato Zenobia, Beate Sick, Bert Hecht, and Urs P. Wild, "*High-quality near-field optical probes by tube etching*," App. Phys. Let., **vol. 75** (1999).

76. Barbara Zitova and Jan Flusser, "*Image registration method: a survey*," Image and Vision Comp., **vol. 21**, 977-1000 (2003).

77. Lisa Gottesfeld Brown, "*A survey of image registration techniques*," ACM computing surveys, **vol. 24**, 325-376 (1992).

78. K. Edward, T. W. Mayes, B. Hocken, and F. Farahi, "*Trimodal imaging system capable of quantitative phase imaging without 2π ambiguities*," Opt. Lett. **vol.33**, 216-218 (2008).

79. M Najiah, M Dahirah, H. Marina, S W. Lee and W. H. Nazaha, "*Quantitative comparisons of erythrocyte morphology in healthy freshwater fish species from Malaysia*," Research Journ. of Fisheries and Hydrobio.**vol. 3**, 32-35 (2008).

80. M Aikawa , "*Morphological changes in erythrocytes induced by malarial parasites*," Biol. Cell, **vol. 64** 173-181 (1988).

81. Brian M. Cooke, Narla Mohandas, Ross L. Coppel, "*The malaria-infected red blood cell: Structural and functional changes*," Advances in Parasitology, **vol. 50**, 1-86, (2001).

82. Leann Tilley, Geoff McFadden, Alan Cowman and Nectarios Klonis, "*Illuminating Plasmodium falciparum-infected red blood cells*," Trends in Parasitology, **vol. 23**, 268-277, (2007).

83. B. S. Lowe, N. K. Jeffa, L. New, C. Pedersen, K. Engbaek, K. Marsh, "*Acridine orange fluorescence techniques as alternatives to traditional Giemsa staining for the diagnosis of malaria in developing countries*," Transactions of the Royal Society of Tropical Medicine and Hygiene, **vol. 90**, 34-36 (1996).

84. Lema, O.E., J.Y. Carter, N. Nagelkerke, M.W. Wangai, P.Kitenge, S.M. Gikunda, P. A. Arube, C. G. Manafu, S. F. Materu, C. A. Adhiambo and H. K. Mukunza, " *Comparison of five methods of malaria detection in the outpatient setting*," Am. J. Trop. Med. Hyg. **vol. 60**, 177-182 (1999).

85. Cathleen Magowan, John T. Brown, Joy Liang, John Heck, Ross L. Coppel, Narla Mohandas, and Werner Meyer-Ilse, "*Intracellular structures of normal and aberrant Plasmodium falciparum malaria parasites imaged by soft x-ray microscopy*," PNAS, **vol. 94**, 6222-6227 (1997).

86. HG Elmendorf and K Haldar, "*Plasmodium falciparum exports the Golgi marker sphingomyelin synthase into a tubovesicular network in the cytoplasm of mature erythrocytes,*" J. Cell Biol., **vol. 124**, 449 – 462 (1994).

87. Lynn F. Lee, Richard D. Schaller, Louis H. Haber, and, Richard J. Saykally, "*High Spatial Resolution Imaging with Near-Field Scanning Optical Microscopy in Liquids*," Anal. Chem. **vol. 73**, 5015-5019 (2001).

88. R. Barer, "*Refractometry and Interferometry of Living Cells*," J. Opt. Soc. Am. **vol. 47**, 545-556 (1957).

89. J Beuthan, O Minet, J Helfmann, M Herrig and G Muller, "*The spatial variation of the refractive index in biological cells*," Phys. in Med. and Biol**. vol. 41** (1996).

90. W. Z. Song, X. M. Zhang, A. Q. Liu, C. S. Lim, P. H. Yap, and Habib Mir M. Hosseini, "*Refractive index measurement of single living cells using on-chip Fabry-Perot cavity*," Appl. Phys. Lett**. vol. 89**, 203901 (2006).

91. W. Z. Song, X. M. Zhang, A. Q. Liu, C. S. Lim, P. H. Yap, and Habib Mir M. Hosseini, "*Refractive index measurement of single living cells using on-chip Fabry-Perot cavity*," Appl. Phys. Lett. **vol. 89**, (2006).

92. V. Backman, M. B. Wallace, L. T. Perelman, J. T. Arendt, R. Gurjar, M. G. Müller, Q. Zhang, G. Zonios, E. Kline, T. McGillican, S. Shapshay, T. Valdez, K. Badizadegan, J. M.Crawford, M. Fitzmaurice, S. Kabani, H. S. Levin, M. Seiler, R. R. Dasari, I. Itzka, J. Van Dam and M. S. Feld, "*Detection of preinvasive cancer cells*," Nature **vol. 406**, 35-36 (2000).

93. X.J. Liang, A.Q. Liu, C.S. Lim, T.C. Ayi and P.H. Yap, "*Determining refractive index of single living cell using an integrated microchip*," Sensors and Actuators A: Physical, **vol. 133**, 9th International Conference on Materials for Advanced Technologies, 349-354 (2007).

94. Jason Reed, Joshua J. Troke, Joanna Schmit, Sen Han, Michael A. Teitell and James K. Gimzewski, "*Live Cell Interferometry Reveals Cellular Dynamism During Force Propagation*," ACS Nano **vol. 2**, 841-846 (2008).

95. Andrew D. L. Humphris, Jamie K. Hobbs, and Mervyn J. Miles, "*Ultrahigh-speed scanning near-field optical microscopy capable of over 100 frames per second*," Appl. Phys. Lett. **vol. 83**, 6-8 (2003).

96. A. D. L. Humphris, M. J. Miles, and J. K. Hobbs, "*A mechanical microscope: High-speed atomic force microscopy*," Appl. Phys. Lett. **vol. 86**, 034106(1-3) (2005).

97. Yongho Seo and Wonho Jhe, "*High-speed near-field scanning optical microscopy with a quartz crystal resonator*," Rev. Sci. Instrum. **vol. 73**, 2057-2059 (2002).

98. Gabriel Popescu, YongKeun Park, Ramachandra R. Dasari, Kamran Badizadegan, and Michael S. Feld, "*Coherence properties of red blood cell membrane motions*," Phys. Rev. E **vol. 76**, 031902(1-5) (2007).

99. Antonello Nesci, René Dändliker, and Hans Peter Herzig, "*Quantitative amplitude and phase measurement by use of a heterodyne scanning near-field optical microscope*," Opt. Lett. **26**, 208-210 (2001).

APPENDIX A: SAMPLE FABRICATION

Prior to RIE etching, a mask was created by first spin coating the substrate with HMDS adhesion promoter at 4000 rpm for 70 seconds. The promoter was allowed to sit on the substrate for 60 seconds before spin coating. This step improved the likelihood that the smallest photo-resist features would adhere to the substrate in the next stage of the fabrication process. S1813 resist was then spun onto the substrate at 2500 rpm for 30seconds followed by 5000 rpm for 30 seconds. The resist was soft baked at 115 °C for 60 seconds. This was followed by UV exposed for 22.4 seconds at 7.64 mW /cm^2. After exposure, the sample was baked a second time for 60 second at 115 °C. The desired irradiation for optimum photo-activation is 120mJ/ cm^2 so the exposure time will depend on power rating of the UV lamp which should be determined when the equipment is first turned on. Development was performed using (1:5) 354 developer (1 part developer 4 parts distilled water) for 40 seconds. Finally, the sample was hard baked at 115 °C for 5 minutes.

The resulting photoresist sample was used to as a mask for RIE etching as described in chapter 3. Using the STS Advance Oxide Etcher system available in the clean room, a recipe was used which included a mixture of C_4F_8, H_2 and He gases at flow rates of 10 sccm (standard cubic centimeter per minute), 174 sccm and 8 sccm respectively. A pressure of 20 mT and a power or 250 W was chosen. An etch rate of 62 Angstroms per second was determined for quartz glass using the aforementioned receipe. Therefore, to etch 1 micron deep structures, the total time required is just over 2.5 minutes. The etcher system was designed to accommodate 6″ diameter wafers but the glass substrates were only 1″ square in size. An aluminum paste has used to adhere the substrate to a “dummy” wafer prior to etching. The paste was cleaned afterwards using isopropanol. It is important that the substrate be place in the middle of the wafer to avoid the wafer tipping over inside the chamber during the sample loading and unloading process. After etching, Removal of the resist mask was achieved by etching the sample in piranha solution.

The most important step of the fabrication process is planarization. This was performed using SU8 photoresist because it was easier to optically locate the underlying structure compared to using S1316 or PGMI resist which are more opaque. Planarization was achieved by overlaying several layers onto the etched substrate. Each layer was heated to ensure reflow and cross-polymerization of the resist. Cross polymerization is desired to ensure that the planarization layer is unaffected by the subsequent lithography procedure for the deposition of surface structures on top of the planarized subsurface features. After each layer, the degree of planarization was determined using a profilometer. Three layers were sequentially placed onto the etched substrate and spun at 2000 rpm for 30 seconds. The estimated thickness of each layer was approximately 2.4 microns. The glass transition temperature of SU8 is 210 °C so the substrate was heated to 215°C for 15 minutes. This resulting in planarization to within 100 nm for 1 micron features. Fewer layers were required for features much less than 1 micron.

The final step in the sample fabrication process involved the deposition of resist 2 micron circles onto the planarized layer of the subsurface sample. A negative resist was used to create the pattern since the underlying trenches were difficult to observe optically when a positive resist such as S1813 was utilized. Subsequent imaging of the subsurface features involves carefully placing the NSOM probe near the edge of the feature prior to scaning, hence it is critical that the subsurface features were optical visible through the resist layer. SU8 resist was spin coated onto the planarized layer at 4000 rpm for 30 seconds. The layer was the soft baked for 100 seconds at 95°C prior to exposure. The sample was exposed for 7 seconds followed by a post exposure bake for 60 seconds at 95°C. Development was performed for 10 seconds followed by a hard bake at 180°C for 10 minutes. The features developed were the negative of the mask used.